# Patterns Selected by Spatial Inhomogeneity

**A DISSERTATION**
**SUBMITTED TO THE FACULTY OF THE GRADUATE SCHOOL**
**OF THE UNIVERSITY OF MINNESOTA**
**BY**

**Jasper Weinburd**

**IN PARTIAL FULFILLMENT OF THE REQUIREMENTS**
**FOR THE DEGREE OF**
**DOCTOR OF PHILOSOPHY**

**Arnd Scheel**

**May, 2019**

# Acknowledgements

First and foremost, I am grateful for the vision, support, and patience of my advisor, Arnd Scheel. You guided me on a course I didn't even see, setting me up for my career better than I had imagined.

To my committee: Thank you Prof. Polacik, for teaching so many of my graduate classes; thank you Prof. Rademacher, for your cheeriness and making the trip all the way from Germany; thank you Prof. McGehee, for shaping a program where I could thrive. Also, thank you Prof. Brubaker for the classes and early guidance.

My cohort and fellow graduate students, thank you for the collaboration and commiseration – especially the boys in office 524. Ben, gym-buddy, co-captain, and one-time neighbor, thank you for sharing this road with me. Sam and Alex, you deserve some special words. I knew long before the trip to Madison that you were both unbearable, yet something's kept us together. That something's truly special – let's not forget it.

For my family:

Eli, thank you for moving all the way to Minnesota so we could grow closer – oh, that's not why you came? Never mind, it was good having you here anyways.

Mom, I'm so glad you kept MN in our lives, so I knew it was a great place. Thank you for keeping us connected to your family here and ensuring I'd continue connecting. I'm especially grateful that my PhD also lead me closer to Grandma in the end.

Dad, you are a primary grounding force in my life. Throughout this ethereal and abstract journey you're somehow able to float with me to understand, then ground me again with a reminder of who I am and what I truly value.

Claire, in some ways this might have been easier without you. But in all the ways that really matter, it would have been impossible.

# Dedication

For my dearest friend, my love, my wife.

## Abstract

This thesis studies patterns that form in environments with sharp spatial variation. In a uniform environment, spots or stripes typically form with a self-consistent width. This width is taken from an interval around a characteristic value determined by the system. With a dramatic spatial variation, our environments only allow patterns in half the spatial region. This sets up a region of patterns directly adjacent to an area where patterns are suppressed. We show that this environmental inhomogeneity significantly restricts the widths of patterns that may occur in a given system. That is, the length of the interval around the characteristic value is significantly reduced.

We examine this phenomenon using a universal partial differential equation model. Reduction techniques from dynamical systems simplify our study to the behavior in a normal form equation (amplitude equation). A difficulty arrises at the location of the discontinuous inhomogeneity; results in the normal form equations on the left and right cannot be directly compared. We construct a transformation of variables that bridges this jump and allows a heteroclinic gluing argument. The explicit form of this transformation determines the widths of patterns that can occur in the inhomogeneous environment.

# Contents

# List of Tables

# List of Figures

# Chapter 1

# Introduction

Some material in this chapter originally appeared in [70].

## 1.1 Patterns in Nature and Experiments

Think of the innumerable patterns that nature creates. Stripes and spots appear in cumulus cloud formations, in bands and circles of vegetation, in animal coats, and many more. These spatial patterns are striking in their visual beauty and their apparent self-organization, see Figure 1.1. The diversity of physical situations exhibiting similar patterns inspires questions into the ubiquity of underlying mechanisms. Carefully controlled experiments attempt to create idealized situations where these mechanisms can be isolated. Prime examples can be found in thermal fluid convection [2, 1], chemical reactions [10, 53, 75], and gas-discharge [6]. In these idealized situations patterns form (nearly) free of defects, which are often present in naturally occurring environments that are not spatially uniform.

In nature, patterns are often shaped by changes in the pattern's environment. For example, vast expanses of cloud streets end abruptly where the atmospheric conditions change, in Figure 1.1a (top left) due to the change from open water to sea ice on the earth's surface below. Similarly, in Figure 1.1a (bottom right), the spots of bare ground end in the distance where a denser species of vegetation dominates, perhaps because of more water availability in that region. Experiments attempt to capture this behavior by introducing an abrupt change in the environment. For instance, in a CDIMA chemical

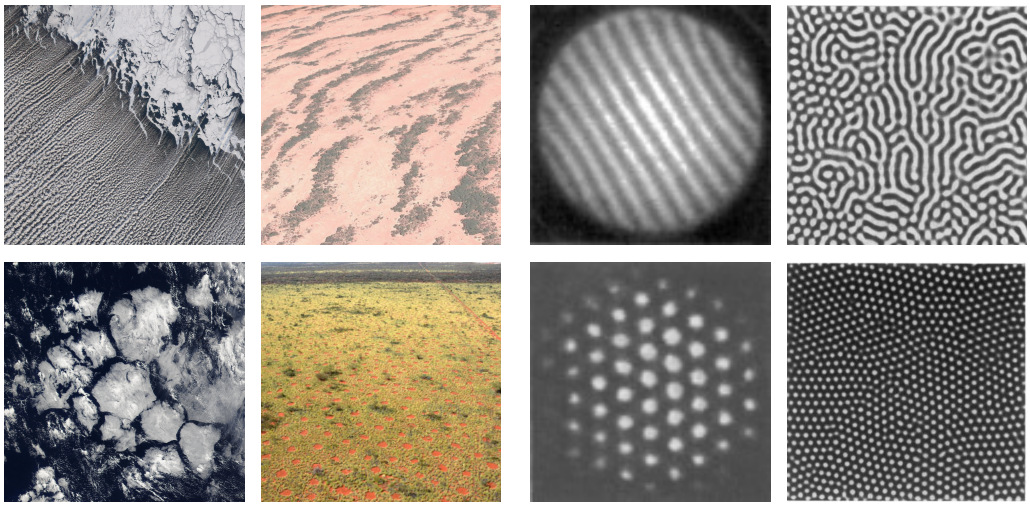

(a) (b)

Figure 1.1: Stripes and hexagons in nature and experiments. (a) Satellite images (left) of cloud streets over the Bering Sea [59] and of hexagonal convection cells in clouds over the Atlantic ocean [60] and aerial photographs (right) of vegetation bands near the border of Somalia and Ethiopia [29] and fairy circles in Australia [24]. (b) Images of experiments with gas discharge (left), reproduced from [6, 68], and with the CIMA chemical reaction (right) showing imperfect stripes and hexagons, reproduced from [75].

reaction, patterns are suppressed in half the domain by a bright light [54]. Locally applying an electric field produces a similar effect in nematic liquid crystals, leading to zigzag patterns in [3] . The abrupt spatial change in the underlying environment induces patterns with particular characteristics.

This is the subject of the present thesis; we study how a spatial inhomogeneity changes the width and stability of stripes and spots. We examine the formation of these patterns through a universal model equation for the pattern-forming *finite-wavelength instability*. This partial differential equation is then equipped with a parameter that varies in space, so that the instability creates patterns in one half of the domain and suppresses them in the other. We uncover a wave-length selection mechanism by proving existence of stationary half-patterned solutions.

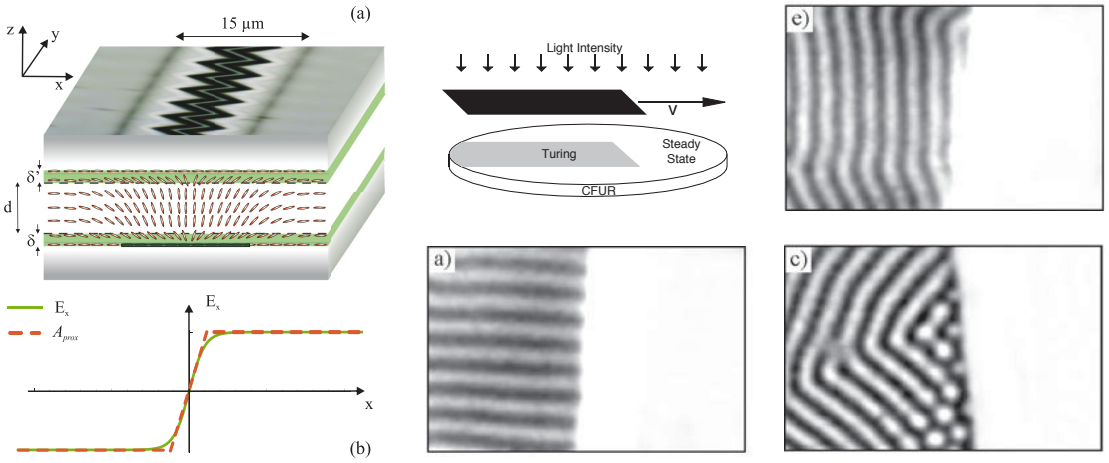


(a) (b)

Figure 1.2: Experiments in environments with spatial inhomogeneity. (a) Experiments in nematic liquid crystal with experimental set up (top) and spatially inhomogeneous voltage (bottom), reproduced from [3]. (b) Experiments in chemical CDIMA reactions with experimental set up (left, top) showing pattern suppressing light on half the experimental domain and experimental results, reproduced from [54].

## 1.2 Modeling Pattern Formation

Specific models of many of the physical systems mentioned above are difficult to build or too complicated to be analyzed mathematically. From a scientific perspective, the many variables and environmental parameters needed to model naturally occurring pattern formation cannot be determined from readily available or observable empirical data. In some laboratory settings, experiments are controlled carefully enough to provide such data but often lead to a model so complex it is mathematically intractable. In particular, it can be difficult to determine which mechanisms and system parameters are responsible for the formation of patterns, even if experimental results suggest a correlation. An alternative approach is to model the pattern-forming phenomena, rather than the systems.

### 1.2.1 Phenomenological Modeling – the Swift-Hohenberg Equation

This approach focuses on the patterns themselves and provides qualitative information grounded in mathematical rigor. An example in the case of one-dimensional, spatially extended systems is carried out by Cross and Hohenberg in [15]. Their approach classifies pattern-forming systems into three categories: type $\mathrm{I}_0$, with spatial patterns that are stationary in time; type $\mathrm{III}_0$, where spatially uniform states oscillate in time; and type $\mathrm{I}_s$, with patterns that oscillate in both space and time. Nonlinear PDE models fall into these classifications based on the spectrum of their linearization about a patterned solution near the uniform, un-patterned state. For the one-dimensional Swift-Hohenberg equation,

$$u_t = -\left(1 + \frac{\partial^2}{\partial x^2}\right)^2 u + \mu u - u^3, \qquad u, x \in \mathbb{R} \tag{1.1}$$

this information can be examined via the linear dispersion relation which determines that small solutions $u \sim e^{\lambda t + i k_x x}$ grow in time for $k_x$ in a small interval around 1. For sufficiently small $\mu > 0$, this leads to a family of stationary periodic solutions with wavenumber $k_x$ satisfying $|k_x^2 - 1|^2 < \mu$. Thus, the Swift-Hohenberg equation is of type $\mathrm{I}_0$. In fact, it has become a protypical model for systems exhibiting this type of instability across a variety of disciplines.

The Swift-Hohenberg equation was originally introduced in 1977 as a model for phenomena observed in Rayleigh-Bénard convection experiments [73]. It has been used to study similar pattern forming phenomena in physical systems ranging from Turing patterns of embryonic development [34], to optics and lasers [23, 45, 46]. Additionally, it has been used as a first model throughout the mathematical literature of pattern formation. Of particular relevance here are studies where the Swift-Hohenberg equation models stripes and grain boundaries [31, 32, 33, 71, 47], spots and spatially localized patterns and patterned fronts [58, 48, 17, 4, 49], and external triggers controlling pattern formation [25, 28, 7]. Many of these sources served as inspiration for, or overlap in methodology and approach with, this thesis.

Many of these studies use a Swift-Hohenberg equation posed on the plane, possibly

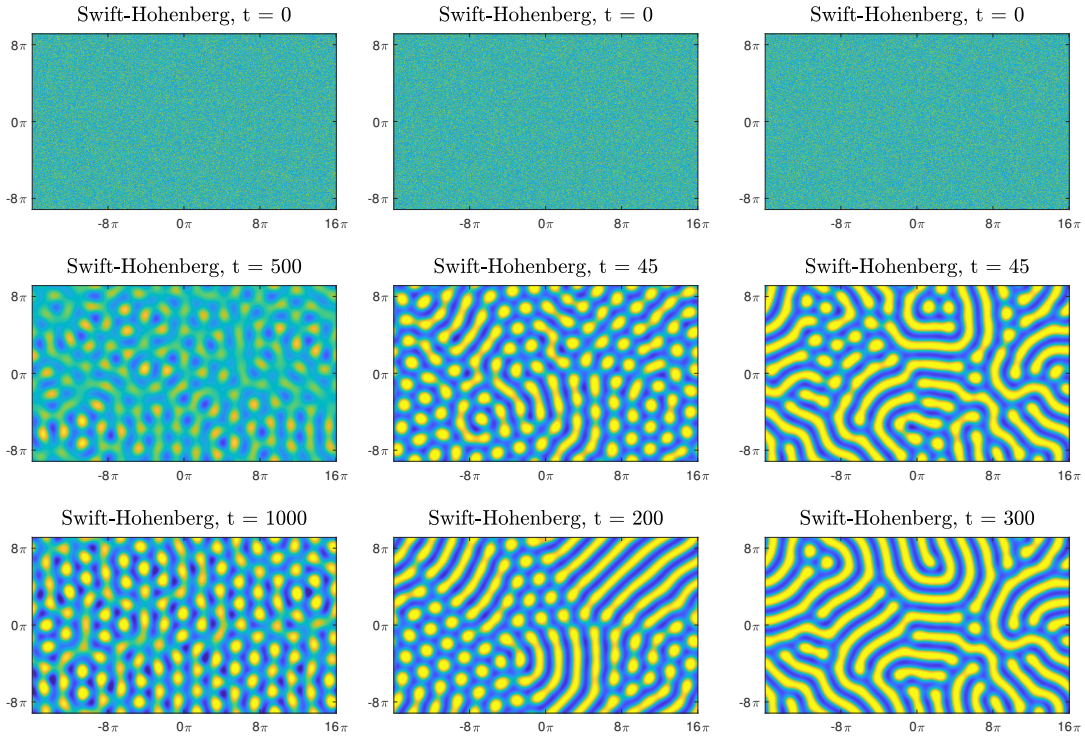


Figure 1.3: Snapshots of numerical simulations of (1.2) with (a) $\varepsilon = 0.1$, (b) $\varepsilon = 0.5$, and (c) $\varepsilon = 0.7$.

with a quadratic term,

$$u_t = -\left(1+\Delta\right)^2 u + \mu u + \nu u^2 - u^3, \qquad u \in \mathbb{R} \qquad (x,y) \in \mathbb{R}^2. \tag{1.2}$$

Among a rich bifurcation structure including numerous spatial patterns, the SH possesses a family of stripes $u_{\text{str}}$, and of hexagons $u_{\text{hex}}$, see [9, 13, 52, 64] among others. Specifically, for small $\mu > 0, \nu = 0$ there is a two-parameter family of stripes,

$$\mathbf{P}_{\text{str}} := \left\{ u_{\text{str}}(k_x x - \phi; k_x) \mid \phi \in [0, 2\pi), |k_x^2 - 1| < \sqrt{\mu} \right\}, \tag{1.3}$$

which are constante in $y, t$, even $u_{\text{str}}(-x) = u_{\text{str}}(x)$, and periodic in $x$, $u_{\text{str}}(k_x x - \phi; k_x) = u_{\text{str}}(k_x(x + 2\pi) - \phi; k_x)$, and constant in $y, t$.

These stripes still exits when $\nu > 0$, small, and they are joined by a family of

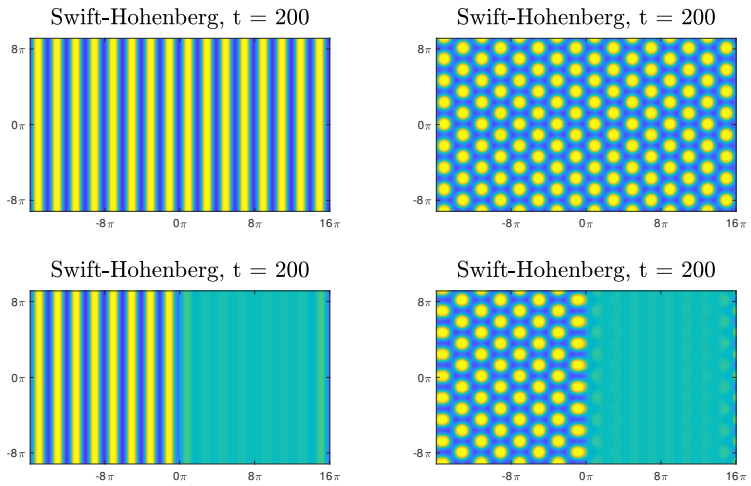


Figure 1.4: Stationary patterns in numerical simulations of (1.2) without (top) and with (bottom) spatial inhomogeneity.

hexagons,

$$\mathbf{P}_{\text{hex}} := \{u_{\text{hex}}(k_x x - \phi, k_y y; k_x) \mid \phi \in [0, 2\pi)\},$$

which are periodic in both $x$ and $y$, and where the wave-vector $\mathbf{k} = (k_x, k_y)$ satisfies $|\mathbf{k}^2 - 1| < \sqrt{\mu}$ and lies on a hexagonal lattice. These solutions are reviewed with more detail in 3.

### 1.2.2 Patterns Selected by Parameter Inhomogeneity

We use the Swift-Hohenberg equation to study patterns in an environment with spatial inhomogeneity. Specifically, we consider a situation where the environment in the left half of the domain suppresses the pattern-forming instability built into the SH equation. We model this situation using a parameter $\mu(x)$ that varies over the spatial domain so that the un-patterned state $u \equiv 0$ is stable for $x > 0$ and unstable for $x < 0$. Then the spatially homogeneous equation (1.2) has a spatial inhomogeneity at $x = 0$, becoming

$$u_t = -(1 + \Delta)^2 u + \mu(x)u + \nu u^2 - u^3, \qquad u \in \mathbb{R}, \qquad (x, y) \in \mathbb{R}^2, \qquad (1.4)$$

where the instability-triggering parameter has a *jump-type inhomogeneity* defined as

$$\mu(x) = \begin{cases} \varepsilon^2, & x < 0 \\ -\varepsilon^2, & x > 0 \end{cases} \qquad \text{for small} \qquad \varepsilon > 0. \tag{1.5}$$

Naturally, one may guess that this problem should have stationary patterns on the left ($x < 0$) and none on the right ($x > 0$). We refer to these solutions as *stationary patterned fronts*.

**Definition 1.1.** Let $u_{\text{pat}}(x, y)$ be a spatially periodic, steady-state solution to the spatially homogenous Swift-Hohenberg equation (1.2). We call $u_*(x, y)$ a *stationary patterned front* if it solves the spatially inhomogeneous Swift-Hohenberg (1.4) and has

(i) $u_*(x, y) \to 0$ as $x \to \infty$ (asymptotically zero on the right)

(ii) $|u_*(x, y) - u_{\text{pat}}(x, y)| \to 0$ as $x \to -\infty$ (asymptotically periodic on the right)

each uniformly in $y$.

Chapter 2 proves the existence of *stationary striped fronts* where the patterned solution $u_{\text{pat}} = u_{\text{str}}$ is a striped solution mentioned above, periodic in $x$ and constant in $y$. With some additional hypotheses, Chapter 3 demonstrates existence of *stationary hexagonal fronts* where $u_{\text{pat}} = u_{\text{hex}}$ is periodic in both $x$ and $y$ so that its maxima are arranged on a hexagonal lattice.

In both cases, we also show a more subtle result: Not every patterned solution present in the homogeneous problem has a corresponding patterned front. Specifically, the horizontal wavenumber $k_x$ on the left-half of patterned fronts is restricted to a narrow interval around 1. Furthermore, that wavenumber is uniquely determined by the phase of the asymptotic pattern. For more on this phenomena, see Section 1.2.3.

Similar jump-type inhomogeneities in the context of pattern formation have been investigated in the mathematical literature, for instance [8, 41, 50, 18, 26, 27, 28, 25, 40, 58]. In Turing's reaction-diffusion model, the idea was formally investigated using asymptotics in [8]. The analysis in [41, 50] for the nonlinear wave and Schrdinger equations is global, but relies on rather explicit knowledge of the phase portraits in spatial dynamics. In contrast, the analysis of reaction-diffusion spikes in [18] is global

but perturbative in nature. Previous work by Scheel, Goh, and others investigates existence of non-stationary striped wave-trains in the case of a moving parameter jump [26, 27, 28] and also in slowly-growing domains [25], which may be seen as an analogue of a slowly moving inhomogeneity. Effects of localized impurities are studied in [40]. In [58], Morrissey and Scheel develop basic concepts useful for stating our main result, which we discuss in the next section. Many of our techniques, such as overlapping phase portraits, were previously used in these scenarios. However, our use of normal form theory appears to be unique in the study of patterns in inhomogeneous environments.

### 1.2.3 Strain-Displacement Relations

We mentioned above that our stationary patterned fronts select patterns with particular wavenumbers from the families of stripes, or hexagons. This *wavenumber selection* is a common phenomenon in pattern formation. In our case, it is best understood through the viewpoint of strain-displacement relations. A strain-displacement relation describes the phase and wavenumber of a certain pattern that may occur in a given system.

In the case of stripes $\mathbf{P}_{\text{str}}$ in the homogeneous equation (1.2), the strain-displacement relation is described by the entire cylinder parameterizing the family $[0, 2\pi) \times J_{k_x}$, where $J_{k_x} = (\sqrt{1-\sqrt{\mu}}, \sqrt{1+\sqrt{\mu}})$. Given a phase $\phi$, we have periodic solutions with any wavenumber in $J_{k_x}$. Similarly, for a given wavenumber $k_x$, translation invariance $x \mapsto x - \phi$ of (1.2) guarantees a stripe solution with any phase.

In our inhomogeneous equation (1.4), it turns out that stationary striped fronts $u_*$ only exist asymptotic to members of $\mathbf{P}_{\text{str}}$ with wavenumbers $k_x = k_x(\phi)$ determined by the phase. We show that for a given $\varepsilon > 0$ sufficiently small, this function is given by an expansion of the form

$$k_x(\phi) = 1 + \frac{\varepsilon^2}{16}\cos(2\phi) + \mathcal{O}(\varepsilon^3). \tag{1.6}$$

Note that this implies that the interval of wavenumbers is restricted from the case above. Where before the bounds of $J_{k_x}$ were $\sim 1 \pm \sqrt{\mu}$, we now have bounds on $k_x$ that are $\sim 1 \pm \varepsilon^2 = 1 \pm \mu$. See Figure 2.1

We think of this selection principle heuristically as follows. Begin with a stationary striped front $u_*$ asymptotic to a certain striped solution $u_{\text{str}}$. Now suppose we vary

the asymptotic phase $\phi$ of the striped front $u_{\text{str}}$, perhaps abstractly or perhaps by some external mechanism. In doing so, we displace the maximum nearest zero, say at $x = -a+\phi < 0$, of the corresponding stripe $u_{\text{str}}$. However, the parameter inhomogeneity of the system disallows this maxima from approaching the jump at $x = 0$ too closely, otherwise the solution cannot converge to zero on the right fast enough – it is an effective boundary condition. Therefore as $\phi \to a$ the system compensates by compressing, or straining, the stripes in the left half of the domain, reducing their width and increasing their wavenumber $k_x$. When the stripes become too narrow, the system forces two stripes to merge, and decreasing the wavenumber – this explains the periodic nature of the strain-displacement relation. In simulations, a similar effect can be obtained by slowly moving the inhomogeneity, as seen in Section 2.6.3

This heuristic helps to explain the terminology; displacement refers to the change in asymptotic phase and strain refers to the compression and expansion of the stripes. For a mathematical definition of strain-displacement relations, see [58] or Definition 1.2 below.

Figure 2.1 shows a strain-displacement relation (blue) in the $(k, \theta)$ plane. Figure 2.2 shows two sample solutions with phase-dependent wavenumbers. The top sample solution corresponds to the point $(k, \theta) = (1.05, 0)$ on the strain-displacement relation of Figure 2.1 and the bottom solution corresponds to the point $(k, \theta) = (0.95, \frac{\pi}{2})$. The difference in asymptotic phases may be observed at $x = 0$ and the difference in wavenumbers may be observed by counting minima.

## 1.3 Pattern Formation via Dynamical Systems

In the remainder of the first chapter, we introduce techniques and methods generally, then comment on their use in our analysis. To this end, suppose that we have a nonlinear, scalar PDE model for pattern formation

$$u_t = f\left(u, \partial_x^i \partial_y^j u; \mu\right), \qquad u(x, y), \mu \in \mathbb{R}, \qquad 1 \leq i, j \leq n. \tag{1.7}$$

with $f$ smooth and satisfying some symmetry conditions. Although we are particularly interested in the case where this PDE is the Swift-Hohenberg equation, we hope that

our approach may inspire similar studies with other universal models of patterned phenomena. Additionally, the generality helps to distinguish our main ideas from technical considerations.

### 1.3.1 Spatial Dynamics

A popular method for analyzing the patterns of a given phenomenological model is to cast the problem as a dynamical system with a specific choice of evolution variable. Referred to as spatial dynamics, this technique has been employed in a wide variety of contexts and models throughout the pattern formation literature. For us, it has the effect that spatial patterns, fronts, and other coherent structures correspond to objects in phase space.

Since we are interested in striped patterns $u_{\text{str}}$, we choose the spatial direction $x$ as the evolution variable. This identifies $u_{\text{str}}$ with a periodic orbit. In problems with radially symmetric "target" patterns, choosing the radial variable $r^2 = x^2 + y^2$ as the evolution variable draws a correspondence between target patterns and periodic orbits. In the study of invasion fronts, one could choose a co-moving frame $\xi = x - ct$, with speed $c$. Now the traveling front corresponds to a heteroclinic connection between two equilibria. All of these examples, and more, can be found in the references mentioned above.

More concretely, suppose we wish to study stationary striped solutions to (1.7) and suppose that $j = 0$, i.e. there are no $\partial_y$ derivatives. Taking the steady-state ($u_t = 0$), one rewrites (1.7) as

$$U' = MU + F(U; \mu) \tag{1.8}$$

where we could choose $U = (u, u_x, u_{xx}, \ldots, u_x^{(n)})^\top \in \mathbb{R}^n$, where $' = \frac{\mathrm{d}}{\mathrm{d}x}$, $M$ is a sparse matrix of ones above the diagonal, and $F$ is the nonlinear part. Now the striped solutions $u_{\text{str}}(k_x x; k_x)$ of the PDE (1.7) correspond to a periodic orbit $U_{\text{per}}(k_x x; k_x)$ in the 4-dimensional phase space of ODE (1.10). In situations where the $y$-derivatives do not vanish, a similar approach yields a dynamical system on an appropriately chosen Banach space $\mathcal{X}$, instead of on $\mathbb{R}^n$. In this case, reduction techniques such as examining dynamics on the center manifold allow one to study a finite dimensional system once

again.

In the next chapter, this thesis employs a similar choice to study stripes in the SH equation. In Chapter 3, we study spots arranged on a hexagonal lattice. There we cannot assume that $\partial_y$ derivatives are zero. Thus, we identify hexagonal patterns with periodic orbits in a Banach space of functions that are periodic in $y$. In both cases, our stationary patterned fronts correspond to heteroclinic connections from a periodic orbit to the zero equilibrium $U \equiv 0$.

### 1.3.2 Normal Forms and Amplitude Equations

One advantage of posing the problem as a dynamical system, is that we gain access to the theory of normal forms. In general, normal form theory dictates that a differential equation satisfying certain hypotheses is equivalent to a *normal form equation* up to some change of coordinates called, the *normal form transformation*. The normal form equation is typically well-studied or might have desirable properties, such as being invariant under useful symmetries. Thus, understanding behavior of its solutions is a good approach to understanding the original equation. In this thesis, we present the normal form theory from the perspective of [30]. Our point of view is that normal form theory provides a mathematical framework for approximating the behavior of a pattern-forming model near the onset of instability.

From a more scientific perspective, this process is typical and falls under the idea of *amplitude equations*. These are equations that approximate the behavior of a physical model. They are often derived only formally using phenomenalogical information as discussed above in [15].

The Swift-Hohenberg (SH) equation has been studied from this perspective by deriving the real Ginzburg-Landau (GL) amplitude equations, see [72] among others. This approach has yielded results on existence and stability of patterns near onset. We derive the amplitude equations from SH using spatial dynamics and normal form theory. The main advantages are two-fold. First, this provides us with rigorous mathematical footing. Second, it allows us to compute the precise changes of coordinates needed to go back and forth between SH and the GL amplitude equations.

The latter is particularly vital for our situation. Because we consider SH with a parameter inhomogeneity, we obtain different amplitude equations on different halves

of the domain (left and right). Naively, one might describe the dynamics by a single amplitude equation with inhomogeneous coefficients. However, it turns out that this neglects the fact that each amplitude equation describes behavior of the system at a different parameter value. Taking our perspective, normal form theory provides us with a computable transformation that mediates this difference by bridging the jump-type inhomogeneity.

Suppose that the normal form of equation (1.10) is given by

$$V' = N(V;\mu), \quad \text{obtained via the transformation} \quad U = V + \Psi(V;\mu). \tag{1.9}$$

When we apply this theory to the same problem with environmental inhomogeneity,

$$V' = MU + F(U;\mu(x)), \qquad \mu(x) = -\operatorname{sgn}(x)\varepsilon^2, \tag{1.10}$$

we obtain two normal form equations and two transformations

$$\text{for } x<0, \quad \dot{V_-} = N(V_-;\varepsilon^2) \quad \text{via} \quad U = \Psi(V_-;\varepsilon^2), \tag{1.11}$$

$$\text{and for } x>0, \quad \dot{V_+} = N(V_+;-\varepsilon^2) \quad \text{via} \quad U = \Psi(V_+;-\varepsilon^2). \tag{1.12}$$

The variables of these two equations $V_-, V_+$ live in fundamentally different phase spaces. To compare them, one must undo and reapply the normal form transformation, yielding half of a commutator

$$\mathcal{T}(\varepsilon) := [\Psi(\cdot;\varepsilon^2)]^{-1} \circ \Psi(\cdot;\varepsilon^2), \tag{1.13}$$

see Figure 1.5 for a schematic.

In our problem, it turns out that $\mathcal{T}(\varepsilon) = \mathrm{Id} + \mathcal{O}(\varepsilon^2)$ and that the additional terms are important in the computation of the strain-displacement relation (1.6). We expect this expansion to hold generally, making the transformation $\mathcal{T}$ the key element in understanding the quantitative effects of the inhomogeneity.

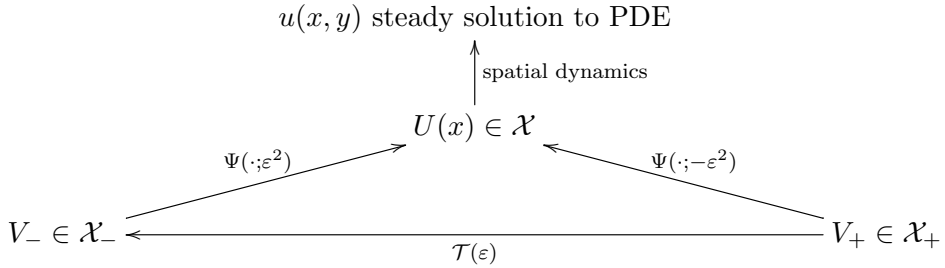


Figure 1.5: A schematic summary of transformations and variables.

### 1.3.3 Invariant Manifolds, Foliations, and Strain-Displacement Relations

Through our use of spatial dynamics, we wish to construct heteroclinic connections from periodic orbits $U_{\text{per}}$ to the zero equilibrium $U \equiv 0$ in a differential equation

$$\dot{U} = F(U), \qquad U \in \mathbb{R}^n \tag{1.14}$$

with the spatial flow $\Phi_x(\cdot)$. We do this through a heteroclinic gluing argument; by finding intersections of unstable and stable manifolds. To this end we recall a few basic definitions which can be found in standard references on dynamical systems and ordinary differential equations such as [65, 11].

Suppose that $D_U F|_0$ is hyperbolic, then there is a neighborhood $\mathcal{U}$ of 0 inside of which we can write the local stable manifold as a graph

$$\mathcal{W}^s_{\text{loc}} := \text{graph}(h)$$

of some function $h\colon \mathcal{U} \to E^u$ as smooth as the vector field $F$, where $E^u$ the linear unstable subspace. Recall that $\mathcal{W}^s_{\text{loc}}$ is forward invariant, it contains all solutions that stay in $\mathcal{U}$ for all $x$, and all solutions with initial condition in $\mathcal{W}^s_{\text{loc}}$ converge to 0 exponentially. We can then flow this local manifold backwards to obtain the *global stable manifold*, or simply the *stable manifold*

$$\mathcal{W}^s := \bigcup_{x<0} \Phi_x(\mathcal{W}^s_{\text{loc}})$$

Similarly, suppose we have a periodic orbit $U_{\text{per}}$ in the phase space of (1.14) and that it has only one Floquet exponent $\lambda = 0$, which is algebraically simple. Then there exists a neighborhood of $U_{\text{per}}$ which decomposes into a backwards-invariant foliation of (local) strong unstable fibers $W^{uu}_{\text{loc}}(x_0)$, for $x_0 \in U_{\text{per}}$. Flowing each of these forward, we obtain a global strong unstable fiber $W^{uu}(x_0) := \bigcup_{x>0} W^{uu}_{\text{loc}}(x_0)$ for $x_0 \in U_{\text{per}}$. The collection of all of these is the *(global) center unstable foliation* of the basic of attraction for the periodic orbit $U_{\text{per}}$

$$\mathcal{W}^{cu}_{U_{\text{per}}} := \bigcup_{x_0 \in U_{\text{per}}} W^{uu}(x_0).$$

We illustrate with a simple example where $\mathcal{W}^{cu}_{U_{\text{per}}}$ can be computed explicitly.

**Example 1.1.** Consider the following ODE, obtained from the steady-state Ginzburg-Landau equations,

$$\begin{aligned} a' &= b \\ b' &= -a + a|a|^2 \end{aligned} \qquad (a,b) \in \mathbb{C}^2, \tag{1.15}$$

and complex conjugate equations. For each $k \in (-1,1)$ (1.15) possesses a periodic orbit

$$a_{\text{per}}(x) = \sqrt{1-k^2}e^{\mathrm{i}kx}, \qquad b_{\text{per}}(x) = \mathrm{i}k\sqrt{1-k^2}e^{\mathrm{i}kx}.$$

Linearizing at $(a,b)_{\text{per}}$ and employing a change of coordinates

$$(a,b,\overline{a},\overline{b}) = (e^{\mathrm{i}kx}A, e^{\mathrm{i}kx}B, e^{-\mathrm{i}kx}\overline{A}, e^{-\mathrm{i}kx}\overline{B}),$$

we arrive at

$$\begin{bmatrix} a' \\ b' \\ \overline{a}' \\ \overline{b}' \end{bmatrix} = \begin{bmatrix} -\mathrm{i}k & 1 & 0 & 0 \\ 2(1-k^2)-1 & -\mathrm{i}k & (1-k^2) & 0 \\ 0 & 0 & \mathrm{i}k & 1 \\ (1-k^2) & 0 & 2(1-k^2)-1 & \mathrm{i}k \end{bmatrix} \begin{bmatrix} a \\ b \\ \overline{a} \\ \overline{b} \end{bmatrix}. \tag{1.16}$$

The Floquet exponents are the eigenvalues of the coefficient matrix, call it $B$, which we

find to be

$$\lambda \in \{0, \pm\sqrt{2}\sqrt{1-3k^2}$$

where 0 is algebraically simple, geometrically double. Thus, for $k < 1/3$ each strong unstable fiber $W^{uu}(x_0)$ is one-dimensional. Note that, due to rotational symmetry in the system, we may take $x_0 = \phi \in [0, 2\pi)$. The global center unstable foliation $\mathcal{W}^{cu}_{(a,b)_{\text{per}}}$ is now two-dimensional and consists of two branches, given explicitly by

$$\begin{aligned} a_d(x;k) &= \left(\sqrt{2}k + \mathrm{i}\sqrt{1-3k^2}\tanh\left(\sqrt{1-3k^2}x/\sqrt{2}\right)\right)e^{\mathrm{i}kx}, \qquad b_d = a_d' \\ a_u(x;k) &= \left(\sqrt{2}k + \mathrm{i}\sqrt{1-3k^2}\coth\left(\sqrt{1-3k^2}x/\sqrt{2}\right)\right)e^{\mathrm{i}kx}, \qquad b_u = a_u' \end{aligned}$$

In fact we may collect these foliations into a single invariant manifold that contains all solutions converging in backward time to the family of periodic orbits with $k^2 < 1/3$, obtaining

$$\mathcal{W}^{cu}_{\mathcal{P}} = \left\{ e^{\mathrm{i}\phi}(a_d, b_d)(x;k), e^{\mathrm{i}\phi}(a_u, b_u)(x;k) \mid k^2 < 1/3, \phi \in [0, 2\pi/k), x < 0 \right\}.$$

In the above situation, when we have a family of periodic orbits

$$\mathcal{P} = \{U_{\text{per}}(kx;k) \mid k \in J_k\}$$

for some interval $J_k$, and every one has only a single, algebraically simple Floquet exponent equal to 0 on the imaginary axis, we say that $\mathcal{P}$ is *normally hyperbolic*. In this situation the whole family $\mathcal{P}$ has a center unstable foliation with fibers parameterized by base points $(k, \phi) \in J_k \times S^1$

$$\begin{aligned} \mathcal{W}^{cu}_{\mathcal{P}} &:= \bigcup_{k \in J_k} \mathcal{W}^{cu}_{(a,b)_{\text{per}}} \\ &= \left\{ W^{uu}(\phi;k) \mid k \in J_k, \phi \in S^1 \right\} \end{aligned}$$

we call $k$ the *asymptotic wavenumber* and $\phi$ the *asymptotic phase*.

We can now rigorously define our idea from the last section, strain-displacement relations. Let the ODE (1.14) have a family of periodic orbits $\mathcal{P}$, as in the last paragraph.

**Definition 1.2.** Let $\mathcal{M}$ be a submanifold of the phase space with a non-empty intersection $\mathcal{W}^{cu}_{\mathcal{P}} \cap \mathcal{M}$. The *strain-displacement* relation determined by $\mathcal{M}$ is the set of values $(k, \phi)$ such that the fiber $W^{uu}(\phi; k)$ intersects $\mathcal{M}$. In symbols

$$\{(k, \phi) \mid W^{uu}(\phi; k) \cap \mathcal{M} \neq 0\}.$$

As a degenerate case, consider a manifold $\mathcal{M}$ intersecting every fiber of $\mathcal{W}^{cu}_{\mathcal{P}}$. Then the strain displacement relation is the whole cylinder $J_k \times S^1$, providing no restriction on the relationship between wavenumber and phase.

*Remark* 1.1. We remark that the most interesting case of strain-displacement relations occur when the intersection is one-dimensional, resulting in a curve in the $k, \phi$-plane, and robust, that is transverse the sense of definition 1.3. In their original introduction [58], these are built into the authors' definition. Examples with one dimensional intersections that are not transverse can be found in the case of snaking, see [4, 49] for instance. There the heteroclinic connection resulting from the intersection of stable and unstable manifolds vanishes in a saddle node bifurcation at the turning point in the "snake" of the bifurcation diagram.

**Example 1.2.** Continuing Example 1.1, we let

$$\mathcal{M} = \{(e^{\mathrm{i}\theta} a_d(0; k), e^{\mathrm{i}\theta} b_d(0; k) \mid \theta \in [0, 2\pi), k \in J_k\}.$$

Then, the intersection is

$$\mathcal{W}^{cu}_{\mathcal{P}} \cap \mathcal{M} = \{(e^{\mathrm{i}\theta}, 0) \mid \theta \in [0, 2\pi)\}$$

which hits fibers with $k = 0$ and every $\phi$. Thus, the strain-displacement relation is given by a vertical line in the $(k, \phi)$-plane. We refer to this situation as unique wavenumber selection. In general, we refer to the situation where not all $k \in J_k$ are attained in the strain-displacement relation as *wavenumber selection.*

In practice, $\mathcal{M}$ is typically a boundary manifold determined by boundary conditions, as in [58], or another invariant manifold such as the stable manifold $\mathcal{W}^s$ of $U \equiv 0$, as in this thesis. For more discussion and examples of strain-displacement relations, see [58].

### 1.3.4 Transversality and Fredholm Properties

We now turn to examine how a strain-displacement relation deforms with a parameter. Consider the equation

$$U' = F(U;\varepsilon), \qquad U \in \mathcal{X} \tag{1.17}$$

where $F(\cdot;\varepsilon)$ is smooth and $\mathcal{X} = \mathbb{R}^n$, or is more generally a Banach space. Suppose that for $\varepsilon = 0$, we have a strain-displacement relation for some manifold $\mathcal{M}(0)$, possibly also depending on $\varepsilon$. A natural question is to wonder if the strain-displacement relation persists smoothly for $\varepsilon > 0$. The answer comes from examining the intersection $P(\varepsilon) = \mathcal{W}^{cu}_{\mathcal{P}}(\varepsilon) \cap \mathcal{M}(\varepsilon)$. Suppose that, for $\varepsilon = 0$, this intersection $P(0)$ is one-dimensional so that we in fact have a strain-displacement curve. The persistence of $P(\varepsilon)$ for $\varepsilon > 0$, depends upon whether or not the intersection is transverse.

**Definition 1.3.** Suppose that two manifolds $\mathcal{W}$ and $\mathcal{M}$ share a 1-dimensional intersection $P$. We say that the intersection $P := \mathcal{W} \cap \mathcal{M}$ is *transverse* in $\mathbb{R}^n$ if for all $p \in P$ the sum of their tangent spaces covers $\mathbb{R}^n$, that is if

$$T_p\mathcal{W} \oplus T_p\mathcal{M} = \mathbb{R}^n.$$

In our situation, if $P(0)$ is transverse, then the Thom transversality theorem guarantees that for almost all sufficiently small $\varepsilon > 0$, the intersection $P(\varepsilon)$ persists smoothly in $\varepsilon$. Therefore the strain-displacement relation does as well.

In Section 2.5.2, we have precisely this situation. There we have 2 and 3-dimensional tangent spaces of the invariant manifolds at the intersection. Transversality is equivalent to these tangent spaces having 4 linearly independent directions. Fixing one parameter, we compute a $4 \times 4$ matrix by taking the derivative of the relation equating the conserved quantities (which define the invariant manifolds). In that situation we confirm transversality, thus persistence, simply by computing a determinant.

In the infinite dimensional setting, when $\mathcal{X}$ is a Banach space, there is a similar transversality theorem involving Fredholm indices. We recall a standard definition.

**Definition 1.4.** Let $\mathcal{L}\colon X \to Y$ be a linear operator between Banach spaces. Then $\mathcal{L}$ is Fredholm if it has finite-dimensional kernel $\ker \mathcal{L}$ and if the range $\operatorname{Rg} \mathcal{L}$ is closed with

finite codimension. The Fredholm index is defined as

$$\operatorname{ind} \mathcal{L} = \dim(\ker \mathcal{L}) - \operatorname{codim}(\operatorname{Rg} \mathcal{L}).$$

For us the infinite-dimensional transversality reduces to a more specific problem. For a given $p \in P(0)$, let $U_*$ be the solution containing $p$. Then $\|U_* - U_{\text{per}}\|_{\mathcal{X}}$ as $x \to -\infty$ and $U_* \to 0$ as $x \to \infty$. Let $\mathcal{L}(x) = U' - D_U F|_{U_*(x)}$ be the linearization of the vector field along $U_*$, with $\varepsilon = 0$. Then the intersection is transverse if $\mathcal{L}$ is invertible, which can be deduced from Fredholm properties, specifically index zero and a trivial kernel. In this situation, theorems of Palmer [62, 63] can be used to compute the Fredholm index of $\mathcal{L}$, since $\mathcal{L}(x)$ is asymptotic to the linearization at $U_{\text{per}}$ and at $U \equiv 0$. Palmer's work relates the functional analytic to the geometric through exponential dichotomies by exploiting the asymptotic structure of $\mathcal{L}$.

An additional advantage of this functional analytic perspective is that it allows us to compute the first order coefficients of the $\varepsilon$-expansion for in the curve $k(\phi)$ defining the strain-displacement relation. Assuming we know that $\mathcal{L}$ is invertible, one can apply the Implicit Function Theorem and Lyaponov-Schmidt reduction to get a Melnikov-type integral. For details in our case, see Section 3.5. Along the same lines, a functional analytic treatment of a similar geometric setting can be found in [12, Section 11.3]. The analysis there can be applied, for instance, in the classical nonlinear, damped harmonic oscillator $u'' - u + u^2 + cu' = 0$ with $u \in \mathbb{R}$, and damping parameter $c$. The stable and unstable manifolds of $u' = u = 0$ intersect transversely, creating a different homoclinic loop for each value $c$. A more contemporary example in yet another setting can be found in [69, Section 1.2].

# Chapter 2

# Striped Fronts

The content of this chapter originally appeared in [70].

## 2.1 Introduction

Among the most common patterns in nature are stripes. The cloud streets in Figure 1.1 can be compared to similar stripes appearing in thermal fluid convection experiments under the umbrella of Rayleigh-Bénard Convection (RBC). A shallow plate of fluid is heated with a constant temperature from below. For temperatures below a critical value, the heat diffuses slowly through the fluid creating a vertically linear temperature gradient. Upon increasing the heat, the fluid's homogeneous temperature gradient becomes a unstable. At this point small perturbations in the form of random noise can cause heated fluid to rise quickly in localized areas and cooler fluid to fall quickly nearby. The rising and falling fluid create polygonal convection cells in the form of squares, hexagons, and stripes (also called convection rolls). The Swift-Hohenberg equation

$$u_t = -\left(1 + \frac{\partial^2}{\partial x^2}\right)^2 u + \mu u - u^3, \qquad u, x \in \mathbb{R} \tag{1.1}$$

was originally introduced to study the patterns created by this instability.

The striped solutions we seek are small, steady-state, spatially-periodic, even solutions of the form

$$u(x,t) = u_{\text{str}}(x;k_x) \sim \varepsilon a e^{\mathrm{i}k_x x} + c.c., \qquad a \in \mathbb{C},$$

where $\varepsilon = \sqrt{\mu} > 0$ is small and $k_x$ is the wavenumber (spatial wave-length) of the stripe. We call these solutions stripes because they correspond to the family $\mathbf{P}_{\text{str}}$ of solutions to the SH equation in the $(x,y)$-plane.[1] For the remainder of this chapter, stripes refer to members of the family

$$\mathbf{P}_{\text{str}} := \left\{ u_{\text{str}}(k_x x - \phi; k_x) \mid \phi \in S^1, k_x \in J_{k_x} \right\}, \tag{2.1}$$

where $J_{k_x} = (-\varepsilon, \varepsilon)$. Such a family of solutions to (1.1) exist for every sufficiently small $\varepsilon > 0$. More information on existence and stability of $\mathbf{P}_{\text{str}}$ can be found in [52] and references therein.

We are interested in the effect of a spatial inhomogeneity on these patterns. Suppose that we modify the RBC experiment by heating only the left half-plate of fluid above the critical temperature. In this case, we may expect the fluid on the right to remain homogeneous and the fluid on the right to form patterns. The analysis presented in this chapter confirms this intuition and additionally determines that the range of spatial periods is significantly restricted from that occurring in the case where the full plate is heated. This selection of certain periods occurs in the full left-half plate, even far from the location of the temperature change.

We represent this temperature change with the jump-type parameter $\mu(x) = -\operatorname{sgn}(x)$ with inhomogeneity at $x = 0$. Thus we examine a 1-dimensional version of 1.4 with no quadratic term ($\nu = 0$), rewriting it here as

$$u_t = -\left(1 + \frac{\partial^2}{\partial x^2}\right)^2 u + \mu(x)u - u^3, \qquad u, x \in \mathbb{R}. \tag{2.2}$$

Intuitively, for $x > 0$ we might expect solutions of (2.2) to obey equation (1.1) with $\mu < 0$, that is we expect $u \equiv 0$ to be stable. Similarly, for $x < 0$ we may expect $u \equiv 0$

[1] Recalling that the solution in $\mathbf{P}_{\text{str}}$ are independent of $y$, it is clear that the analysis in this chapter, which is one-dimensional, extends trivially to a family of stripes for the planar SH equation.

to be unstable and instead see steady, periodic stripes $u_{\text{str}}$, as in the $\mu > 0$ case above. We refer to a solution of (2.2) that exhibits both these behaviors as a *stationary striped front*, see Definition 1.1.

We prove the existence of stationary patterned fronts. Furthermore, we prove that the asymptotic wavenumber of such a solution must satisfy a strain-displacement relation

$$k_x(\phi;\varepsilon) = 1 + \tfrac{\varepsilon^2}{16}\cos 2\phi + \mathcal{O}(\varepsilon^3)$$

where $k_x$ is the wavenumber of the asymptotic stripes and $\phi$ is the asymptotic phase. In the homogeneous $\mu = \varepsilon^2 > 0$ setting, the interval of wavenumbers mentioned above is $J_{k_x} \sim (-\varepsilon, \varepsilon)$. Our result implies that stationary striped fronts are asymptotic to stripes with wavenumbers in the smaller interval $(-\varepsilon^2, \varepsilon^2) \subsetneq J_{k_x}$. Note that, particularly because $\varepsilon$ is small, is a significant restriction on the wavenumbers – a phenomenon we refer to as *wavenumber selection*. See Figure 2.1. Our result can be stated formally as follows.

**Theorem 2.1.** *For sufficiently small $\varepsilon > 0$, there exists a one-parameter family stationary striped fronts $u_*(x)$ solving the Swift-Hohenberg equation with spatial inhomogeneity* (2.2). *The family $u_*(x;\phi) = u_*(x;\phi + 2\pi)$ is periodic in the parameter $\phi$. Each $u_*$ is asymptotic to a stripe $u_{\text{str}} \in \mathbf{P}_{\text{str}}$ whose phase $\phi$ determines its wavenumber $k_x$ according to a strain-displacement relation given by*

$$k_x(\phi;\varepsilon) = 1 + \tfrac{\varepsilon^2}{16}\cos 2\phi + \mathcal{O}(\varepsilon^3).$$

*Remark* 2.1. As a stationary striped front, each solution $u_*(x;\phi)$ has:

(i) $u_*(x;\phi) \to 0$ as $x \to \infty$, and

(ii) $|u_*(x;\phi) - u_{\text{str}}(xk_x - \phi; k_x)| \to 0$ as $x \to -\infty$,

for some $u_{\text{str}} \in \mathbf{P}_{\text{str}}$. See Definition 1.1

**Chapter Outline** The remainder of the chapter proves this result with modest excursions into exposition of necessary background material. In Section 2.2, we show an analogous but simpler result for a set of ordinary differential equations known as the real

Ginzburg-Landau equations. Here we use a heteroclinic gluing argument by finding the intersection of an unstable and stable manifold with the help of [58]. The real GL equation represents the SH equation near the onset of the pattern-forming instability, i.e. for small $u, \mu = \varepsilon^2$. In Sections 2.3 and 2.3.3, we discuss the explicit coordinate transformations used to obtain GL from SH. Section 2.3 includes normal form theory from [30], which we use for the first of the transformations. Next, we describe a co-rotating reference frame and a rescaling change of coordinates in Section 2.3.3. After rescaling and expressing the normal form equation in co-rotating coordinates, we have the desired form similar to the GL equation plus an order $\mathcal{O}(\varepsilon)$ perturbation. Persistence of the unstable and stable manifolds found earlier requires some technical considerations in 2.4.2. After all transformations have been applied and persistence verified, the two invariant manifolds we found in Section 2.2 do not lie in the same phase space, see Figure 2.3. To remedy this, in Section 2.5 we "move" the unstable manifold into the same phase space as the stable manifold, allowing us to make sense of the intersection found earlier. We next prove that this intersection is transverse, thus persisting in the full equations with smooth dependence on $\varepsilon$. Then we apply the Implicit Function Theorem to compute the first term in the $\varepsilon$-expansion of the strain-displacement relation $k_x(\phi)$, proving Theorem 2.1.

## 2.2 Ginzburg-Landau Amplitude Equations

The Ginzburg-Landau (GL) amplitude equations are often used to describe stripes in one dimension. In [51], they are derived as equations governing the amplitude of solutions to the Swift-Hohenberg equation (SH). Derivations of GL from SH have been repeated with a range of rigor, from formal asymptotics to careful proofs [61, 74, 38, 15, 72]. In Section 3.4, we conduct our own derivation using the normal form theory of [30]. In this section, we use the GL equations with a spatial inhomomogeneity

$$\begin{aligned} a' &= b \\ b' &= \operatorname{sgn}(x)a + a|a|^2 \end{aligned} \qquad (a,b) \in \mathbb{C}^2 \tag{2.3}$$

as a preliminary example. We describe essential equilibria, periodic orbits, and invariant manifolds – many of which may be described explicitly in this case. We then prove

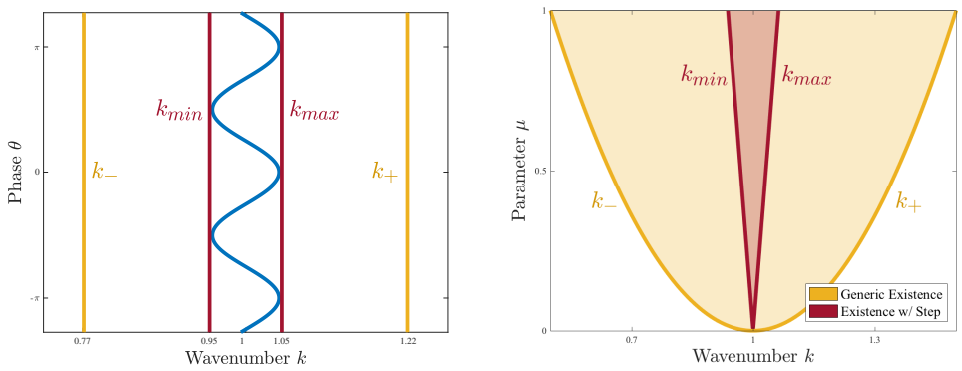


Figure 2.1: Bounds on wavenumbers $k_x$ of solutions to the Swift-Hohenberg equation with constant parameter ($k_\pm$, gold) and with jump-type parameter ($k_{\min/\max}$, red). (a) With $\mu = 0.8$, strain-displacement relation (blue) and bounds on wavenumber (gold, red). (b) Regions of existence for stripe solutions to (1.1) (gold) and stationary striped front solutions to (1.4) (red).

existence of a family of heteroclinic connections that serve as the foundation for our results in the SH equation.

The GL equations govern the complex amplitude $a(x)$ of a solution $u(x)$ to the steady-state SH equation. In particular, $u \sim \varepsilon\,\mathrm{Re}(e^{\mathrm{i}x}a(x))$ and so when $a \equiv 1$, we have that $u \sim \varepsilon\cos x$ is periodic. Thus, we're interested in equilibria of GL and solutions that tend to 0 as $x \to \infty$.

**Lemma 2.2.** *For any $\theta \in [0, 2\pi)$, the spatially inhomogeneous GL equations (2.3) possess a heteroclinic connection $(a_*, b_*)$ from the equilibrium $(e^{\mathrm{i}\theta}, 0) \to (0, 0)$. Furthermore, there is no other heteroclinic to $(0, 0)$ originating from either an equilibrium or a periodic orbit.*

The general strategy is to consider two separate equations on the half lines $x < 0$ and $x > 0$, then find an intersection of unstable and stable manifolds at $x = 0$. See Figure 2.2.

In the rest of this section we often rely on explicit solutions. These are made possible by the following conserved quantities for (2.3). For $x > 0$ we have the Hamiltonian $\mathcal{H}_+$

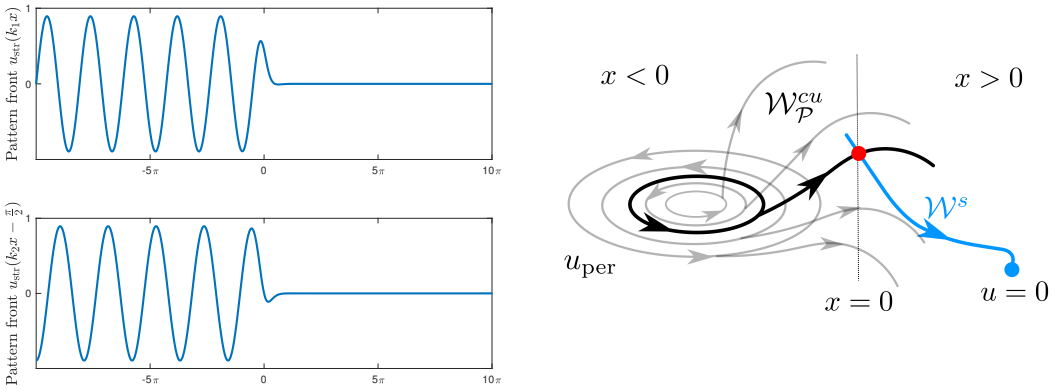


(a) (b)

Figure 2.2: (a) Half-stripe solutions with asymptotic phase shifts 0 (top) and $\frac{\pi}{2}$ (bottom). The dependence of wavenumber on phase is illustrated by the difference in number of maxima. (b) Schematic showing spatial dynamics with a heteroclinic from $u \equiv 0$ to a periodic solution.

and for $x < 0$ we have the Hamiltonian $\mathcal{H}_-$ where

$$\mathcal{H}_\pm = |b|^2 \mp |a|^2 - \tfrac{1}{2}|a|^4.$$

Next, notice that for both of $x < 0$ and $x > 0$, equation (2.3) is invariant under the $\mathbb{C}$-rotational symmetry $\mathcal{R}_\theta \colon (a, b) \mapsto (e^{\mathrm{i}\theta}a, e^{\mathrm{i}\theta}b)$. That is, if $(a(x), b(x))$ is a solution then so is $(e^{\mathrm{i}\theta}a(x), e^{\mathrm{i}\theta}b(x))$ for all $\theta \in [0, 2\pi)$. Together, this groups of rotations is a flow which, by Noether's Theorem [5], generates a vector field with first integral

$$M = \mathrm{Im}(a\bar{b}).$$

### 2.2.1 Dynamics for $x > 0$

Consider the equation on the positive half line $\{x > 0\}$

$$\begin{aligned} a' &= b \\ b' &= a + a|a|^2. \end{aligned} \tag{2.4}$$

**Lemma 2.3.** *The origin* $(0, 0)$ *is a hyperbolic equilibrium with 2-dimensional stable*

*manifold*

$$\mathcal{W}^s = \Big\{ \left( e^{\mathrm{i}\phi} r, e^{\mathrm{i}\phi} \sqrt{r^2 + \tfrac{1}{2} r^4} \right) \mid r > 0, \phi \in [0, 2\pi) \Big\}.$$

*Proof.* First, we find that $\mathcal{W}^s$ is 2-dimensional, which guarantees that we have one containment in the equality above. Since $a, b \in \mathbb{C}$, we append the complex conjugate equations and consider the equations in the full space $\tilde{\mathbb{C}}^2 = \{(a, b, \overline{a}, \overline{b}) \mid a, b \in \mathbb{C}\}$. Now the linearization of the vector field at $(0, 0)$ is

$$\begin{bmatrix} 0 & 1 & 0 & 0 \\ 1 & 0 & 0 & 0 \\ 0 & 0 & 0 & 1 \\ 0 & 0 & 1 & 0 \end{bmatrix} \begin{bmatrix} a \\ b \\ \overline{a} \\ \overline{b} \end{bmatrix}$$

which has two positive and two negative eigenvalues. Therefore the stable manifold $\mathcal{W}^s$ is 2-dimensional. Since the set on the right is 2-dimensional and stable manifolds are connected and smooth, all that's left to show is that

$$\mathcal{W}^s \supseteq \{ \left( e^{\mathrm{i}\phi} r, e^{\mathrm{i}\phi} \sqrt{r^2 + \tfrac{1}{2} r^4} \right) \mid r > 0, \phi \in [0, 2\pi) \}.$$

The following is an explicit real solution

$$(a_{Re}, b_{Re})(x) = \left( \frac{4e^x}{1 - 2e^{2x}}, \frac{16e^{3x}}{(1 - 2e^{2x})^2} + \frac{4e^x}{1 - 2e^{2x}} \right) \quad \text{for} \quad x \in (\sqrt{\ln 2}, \infty).$$

This orbit is contained in $\mathcal{W}^s$ because $(a_{Re}, b_{Re}) \to (0, 0)$ as $x \to \infty$ and $|(a_{Re}, b_{Re})|$ grows at least exponentially as $x \to \sqrt{\ln 2}$ from the right. Additionally, with some algebra we observe that this solution is of the form $\left( r, \sqrt{r^2 + \frac{1}{2} r^4} \right)$ for $r = r(x) = \frac{4e^x}{1 - 2e^{2x}}$.

Let $(a, b)$ be in the set on the right. Fix $r, \phi$ so that $(a, b) = (e^{\mathrm{i}\phi} r, e^{\mathrm{i}\phi} \sqrt{r^2 + \frac{1}{2} r^4})$. Now $(e^{-\mathrm{i}\phi} a, e^{-\mathrm{i}\phi} b) = (r, \sqrt{r^2 + \frac{1}{2} r^4}) = (a_{Re}, b_{Re})(x)$ for some $x \in (\sqrt{\ln 2}, \infty)$. Since the real solution $\{(a_{Re}, b_{Re}) \mid x \in (\sqrt{\ln 2}, \infty)\} \subseteq \mathcal{W}^s$, therefore $(e^{-\mathrm{i}\phi} a, e^{-\mathrm{i}\phi} b) \in \mathcal{W}^s$. By the rotational symmetry, $(a, b) \in \mathcal{W}^s$.

□

### 2.2.2 Dynamics for $x < 0$

On the negative half line $\{x < 0\}$, the equation becomes

$$\begin{aligned} a' &= b \\ b' &= -a + a|a|^2. \end{aligned} \tag{2.5}$$

There exists a family of periodic orbits $(a_{\text{per}}, b_{\text{per}})(k)$ parameterized by wavenumber $-1 < k < 1$ and defined by the solutions

$$(a_{\text{per}}, b_{\text{per}})(x; k) = (\sqrt{1-k^2}e^{\mathrm{i}kx}, ik\sqrt{1-k^2}e^{\mathrm{i}kx})$$

For fixed $k \neq 0$, rotating a member of this family results only in a phase shift, and leaves it unchanged as an orbit:

$$\begin{aligned} \mathcal{R}_\theta(a_{\text{per}}, b_{\text{per}})(x; k) &= (\sqrt{1-k^2}e^{\mathrm{i}kx+i\theta}, ik\sqrt{1-k^2}e^{\mathrm{i}kx+i\theta}) \\ &= (\sqrt{1-k^2}e^{\mathrm{i}k(x+\frac{\theta}{k})}, ik\sqrt{1-k^2}e^{\mathrm{i}k(x+\frac{\theta}{k})}) \\ &= (a_{\text{per}}, b_{\text{per}})(y; k) \qquad\qquad \text{for } y = x + \tfrac{\theta}{k} \in \mathbb{R} \end{aligned}$$

For $k = 0$, there is a circle of equilibria $(e^{\mathrm{i}\theta}, 0)$ given by rotating the equilibrium solution $(a_{\text{per}}, b_{\text{per}})(x; 0) = (1, 0)$. We think of this circle of equilibria as a degenerate case. We will explicitly construct a center unstable foliation of the normally hyperbolic submanifold

$$\mathcal{P} = \left\{(a_{\text{per}}, b_{\text{per}})(k) \mid k^2 < 1/3\right\}.$$

Using Floquet theory we showed in Example 1.1 that for each $k^2 < \frac{1}{3}$, the periodic orbit $(a_{\text{per}}, b_{\text{per}})(k)$ has a strong unstable fiber that is 1-dimensional. The collection of these fibers is a 2-dimensional center unstable foliation of the periodic orbit. Each fiber has has a bounded and an unbounded branch, both of which are given explicitly in [58]. For our purposes, the bounded branch is the important one, and we save remarks on the unbounded branch for the end of the section.

The bounded branch of an unstable fiber is given by

$$a_d(x;k) = \left(\sqrt{2}k + \mathrm{i}\sqrt{1-3k^2}\tanh\left(\sqrt{1-3k^2}x/\sqrt{2}\right)\right)e^{\mathrm{i}kx} \tag{2.6}$$

and, with a quick computation,

$$\begin{aligned} b_d(x;k) = a_d' = &-k\sqrt{1-3k^2}\tanh\left(\sqrt{1-3k^2}x/\sqrt{2}\right)e^{\mathrm{i}kx} &(2.7)\\ &+ i\left(\sqrt{2}k^2 + \frac{1-3k^2}{\sqrt{2}}\operatorname{sech}^2\left(\sqrt{1-3k^2}x/\sqrt{2}\right)\right)e^{\mathrm{i}kx}. &(2.8)\end{aligned}$$

For each $k^2 < \frac{1}{3}$, the reader may check that the pair $(a_d, b_d)$ is a solution to equations (2.5). We call these *defect* solutions since they are asymptotically close to the periodic $(a_{\mathrm{per}}, b_{\mathrm{per}})(k)$ except for a brief excursion near $x = 0$ caused by the tanh term. This excursion also creates a phase shift between the asymptotic periodic orbits on the left and right. Indeed, $|(a_d, b_d)(k) - (a_{\mathrm{per}}, b_{\mathrm{per}})(k)| \to 0$ as $x \to \pm\infty$.[2]

Rotating by $\mathcal{R}_\psi$ sends fibers to fibers and so the bounded branch of the center unstable foliation of the periodic orbit $(a_{\mathrm{per}}, b_{\mathrm{per}})(k)$ is given by

$$\mathcal{W}^u_{\mathrm{bdd}}(k,\psi) = \left\{\mathcal{R}_\psi\left(a_d(x;k), b_d(x;k)\right) \mid x \in \mathbb{R}\right\}.$$

For each $\psi$, we have a fiber given by the solution $\left(e^{\mathrm{i}\psi}a_d(x;k), e^{\mathrm{i}\psi}b_d(x;k)\right)$ which, as $x \to -\infty$, approaches the periodic orbit $(a_d(x;k), b_d(x;k))$ with a different phase. Thus, when $k = 0$, the solution $(a_d(x;0), b_d(x;0)) \to (1,0)$ as $x \to -\infty$. Similarly, each fiber $\mathcal{R}_\psi\left(a_d(x;0), b_d(x;0)\right) \to (e^{\mathrm{i}\psi}, 0)$.

**Lemma 2.4.** *The bounded branch of the center unstable foliation of the normally hyperbolic subfamily of periodic orbits $\mathcal{P} = \{(a_{per}, b_{per})(k) \mid k^2 < 1/3\}$ is given by*

$$\mathcal{W}^{cu}_{\mathcal{P},bdd} = \left\{\mathcal{R}_\psi\left(a_d(x;k), b_d(x;k)\right) \mid x \in \mathbb{R}, \psi \in [0, 2\pi), k^2 < 1/3\right\}. \tag{2.9}$$

*Remark* 2.2. The unbounded branch of the strong unstable fiber of a periodic orbit $(a_{\mathrm{per}}, b_{\mathrm{per}})(k)$ is given by

$$\mathcal{W}^{cu}_{\mathcal{P},\mathrm{un}}(k,\psi) = \left\{\mathcal{R}_\psi\left(a_u(x;k), b_u(x;k)\right) \mid x \in \mathbb{R}\right\}$$

[2] In fact, this convergence is exponential, as guaranteed by the Floquet Theorem.

where $a_u(x;k) = \left(\sqrt{2}k + \mathrm{i}\sqrt{1-3k^2}\coth\left(\sqrt{1-3k^2}x/\sqrt{2}\right)\right)e^{\mathrm{i}kx}$ and $b_u = a_u'$. This unbounded branch does not intersect the stable manifold $\mathcal{W}^s$ found in Lemma 2.3, and so is less relevant to our computation.

### 2.2.3 Heteroclinic Gluing – Intersection of Invariant Manifolds

**Lemma 2.5.** *The intersection of the stable manifold of* $(0,0)$ *in the* $x > 0$ *dynamics and the center unstable foliation of periodic orbits* $\mathcal{P}$ *in the* $x < 0$ *dynamics is*

$$\mathcal{W}^s \cap \mathcal{W}^{cu}_{\mathcal{P}} = \left\{ \left( \frac{1}{2}e^{\mathrm{i}\theta}, \frac{3}{4\sqrt{2}}e^{\mathrm{i}\theta} \right), \theta \in [0, 2\pi) \right\}. \tag{2.10}$$

*and occurs for parameter values* $r = \frac{1}{2}, x = \sqrt{2}\operatorname{arctanh}\frac{1}{2}, k = 0$, *and any* $\theta, \psi$ *such that* $\psi = \theta - \frac{\pi}{2} \mod 2\pi$.

*Proof.* We search only for the intersection $\mathcal{W}^s \cap \mathcal{W}^{cu}_{\mathcal{P},\mathrm{bbd}}$ with the bounded part of the stable manifold; one can verify that the unbounded branch of $\mathcal{W}^s_{\mathcal{P}}$ does not intersect the unstable manifold $\mathcal{W}^s$ but we omit the details. We set the parameterization of Lemma 2.3 equal to the parameterization in Lemma 2.4 and solve.

By using the conserved quantity $M = \mathrm{Im}(a\bar{b})$, we can show that $k = 0$. This significantly simplifies the algebra and allows us to obtain an exact solution. First, note that $M|_{\mathcal{W}^{cu}} = 0$, so $M|_{\mathcal{W}^{cu}_{\mathcal{P},\mathrm{bbd}}} = \mathrm{Im}(a_d\bar{b}_d) = 0$. By the specific structure of $\mathcal{W}^{cu}_{\mathcal{P},\mathrm{bbd}}$, we know that $k$ is constant along solutions contained in the stable foliation (this is also evident from our parameterization). Since $\mathrm{Im}(a_*\overline{b_*}) = -k(1-k^2)$ and $(a_d, b_d)(k) \to (a_{\mathrm{per}}, b_{\mathrm{per}})(k)$, we must have $-k(1-k^2) = 0$. Since $k^2 < \frac{1}{3}$, we see that $k = 0$. Plugging $k = 0$ into the equations and considering real and imaginary parts allows us to explicitly solve for the resulting parameter values. □

We are now ready to prove the result of the section.

*Proof of Lemma 2.2.* For $\theta = 0$, let $(a, b)$ be a solution to (2.3) with initial condition $(a(0), b(0)) = \left(\frac{1}{2}, \frac{3}{4\sqrt{2}}\right)$. Flowing backwards in $x$ gives us $(a, b) \to (0, 0)$ as $x \to \infty$ because $\left(\frac{1}{2}, \frac{3}{4\sqrt{2}}\right) \in \mathcal{W}^s$. Flowing forwards in $x$ gives us $(a, b) \to (1, 0) = \lim_{x\to\infty}(a_d(x;0), b_d(x;0))$ as $x \to -\infty$ because $\left(\frac{1}{2}, \frac{3}{4\sqrt{2}}\right) \in \mathcal{W}^{cu}_{\mathcal{P}}$.

For nonzero $\theta$, set the initial condition $(a(0), b(0)) = \mathcal{R}_\theta\left(\frac{1}{2}, \frac{3}{4\sqrt{2}}\right)$. □

In the following sections, we use a series of coordinate changes to reduce the original spatially inhomogeneous Swift-Hohenberg equation (2.2) to a system of equations which are equivalent to the ones studied here, at leading order in the parameter $\mu$.

## 2.3 Swift-Hohenberg in Normal Form

In this section we compute the normal form of the Swift-Hohenberg equation and truncate to obtain the Ginzburg-Landau equations of Section 2.2. Recall the space-dependent Swift-Hohenberg equation (2.2). In this section, we fix $\mu(x) \equiv \mu > 0$ as a small constant. The idea will be to apply the results of this section to $x < 0$ and $x > 0$ independently to obtain a normal form equation for each half of the real line.

### 2.3.1 Spatial Dynamics

We begin by writing the steady-state SH equation (1.1), with constant $\mu(x) \equiv \mu$ as a first order equation in $\mathbb{R}^4$. So

$$0 = u + 2u_{xx} + u_{xxxx} - \mu u + u^3$$

becomes

$$\frac{dU}{dx} = LU + R(U, \mu), \tag{2.11}$$

where

$$U = \begin{bmatrix} u \\ u_x \\ u_{xx} + u \\ u_{xxx} + u_x \end{bmatrix} \in \mathbb{R}^4, \quad L = \begin{bmatrix} 0 & 1 & 0 & 0 \\ -1 & 0 & 1 & 0 \\ 0 & 0 & 0 & 1 \\ 0 & 0 & -1 & 0 \end{bmatrix}, \quad R(U, \mu) = \begin{bmatrix} 0 \\ 0 \\ 0 \\ \mu U_1 \end{bmatrix} + \begin{bmatrix} 0 \\ 0 \\ 0 \\ -U_1^3 \end{bmatrix}.$$

In this form, our equation undergoes a "reversible-Hopf bifurcation" or a "reversible $1:1$ resonance" as described in [30, §4.3.3] at $\mu = 0$. The symmetry $u(x) = u(-x)$ of the SH equation has been replaced by the reversibility symmetry $\mathbf{S}$ defined by $\mathbf{S}U =$

$(U_1, -U_2, U_3, -U_4)^\top$, which anti-commutes with the vector field on the right-hand side of Equation (2.11). This reversibility plays an important role in the computation of the normal form equation and transformations below.

### 2.3.2 Normal Form Theorems

In this section, we present a normal form equation which represents the dynamics of the ODE in the last section for sufficiently small $\mu$ values. Our normal form equation is the same as that found in [30]. However, we also compute the leading $\mu$-dependent part of the transformation used to arrive at the normal form equation; it is essential for our future steps.

We define the space $\widetilde{\mathbb{C}^2} := \mathbb{C}^4/\langle (A,B,C,D) - (\overline{C},\overline{D},\overline{A},\overline{B})\rangle = \{(A,B,\overline{A},\overline{B}) \mid A,B \in \mathbb{C}\}$. Clearly $\widetilde{\mathbb{C}^2} \cong \mathbb{C}^2$, and so we drop the $\widetilde{\ }$ to simplify notation. Note that the matrix

$$\Theta = \begin{bmatrix} 1 & 0 & 1 & 0 \\ i & 1 & -\mathrm{i} & 1 \\ 0 & 2i & 0 & -2i \\ 0 & -2 & 0 & -2 \end{bmatrix} \qquad \text{maps} \qquad \mathbb{C}^2 \to \mathbb{R}^4.$$

The change of variables $U = \Theta(A,B)$ puts the linear part $L$ into Jordan normal form and yields an equation of the form

$$\begin{bmatrix} A_x \\ B_x \end{bmatrix} = \begin{bmatrix} i & 1 \\ 0 & i \end{bmatrix} \begin{bmatrix} A \\ B \end{bmatrix} + \widetilde{R}(A,B;\mu) \tag{2.12}$$

and the complex conjugate equations.

**Lemma 2.6** (Normal Form Equation)**.** *[30, Lem. 3.17] For any positive integer $N \geq 1$, there exist neighborhoods $\mathcal{U}, \mathcal{V}$ of $0$ in $\mathbb{C}^2$ and $\mathbb{R}$ respectively so that for any $\mu \in \mathcal{V}$ there exists a polynomial $\Phi(\,\cdot\,;\mu)\colon \mathbb{C}^2 \to \mathbb{C}^2$ of degree $N$ with the following properties:*

*(i) The coefficients of the monomials of degree $q$ in $\Phi(\,\cdot\,;\mu)$ are functions of $\mu$ of class $\mathcal{C}^{N-q}$,*

$$\Phi(0,0;0) = 0, \qquad \partial_{(A,B,\overline{A},\overline{B})}\Phi(0,0;0) = 0, \quad \textit{and} \quad \mathbf{S}\Phi(A,B;\mu) = \Phi(\overline{A},-\overline{B};\mu).$$

*(ii) For $(A, B) \in \mathcal{U}$, the change of variables*

$$(A, B) \mapsto \mathrm{Id} + \Phi(A, B; \mu) \tag{2.13}$$

*gives a transformation $\mathbb{C}^2 \leftrightarrow \mathbb{C}^2$ which transforms equation* (2.12) *into*

$$\begin{bmatrix} A_x \\ B_x \end{bmatrix} = \begin{bmatrix} i & 1 \\ 0 & i \end{bmatrix} \begin{bmatrix} A \\ B \end{bmatrix} + \begin{bmatrix} iP(A, B; \mu) & 0 \\ Q(A, B; \mu) & iP(A, B; \mu) \end{bmatrix} \begin{bmatrix} A \\ B \end{bmatrix} + G(A, B; \mu) \tag{2.14}$$

*where the remainder $G$ is smooth and $G(A, B; \mu) = o((|A| + |B|)^N)$ and $P, Q$ are real valued polynomials of degree $N - 1$ given by*

$$P(|A|^2, (A\overline{B} - \overline{A}B); \mu) = -\tfrac{1}{8}\mu + \tfrac{9}{16}|A|^2 + \mathcal{O}\left((|\mu| + (|A| + |B|)^2)^2\right)$$
$$Q(|A|^2, (A\overline{B} - \overline{A}B); \mu) = -\tfrac{1}{4}\mu + \tfrac{3}{4}|A|^2 + \tfrac{3i}{16}(A\overline{B} - \overline{A}B) + \mathcal{O}\left((|\mu| + (|A| + |B|)^2)^2\right).$$

This lemma is a restatement of Lemma 3.17 [30, §4.3.3] in the particular case of a double eigenvalue equal to $i$. In an example in the same section, the authors compute the first three coefficients in each of the polynomials $P, Q$ as they appear above. To do this they execute part of an algorithmic computation which is derived from their proof of the normal form theorem. The same algorithm may be used to compute the normal form transformation itself $\mathrm{Id} + \Phi(A, B; \mu)$. We do part of this in the proof of the next lemma.

There are a few important features of the normal form equation (2.14). When truncated by removing $G$, it is equivariant under the reversibility symmetry $\mathbf{S}$ and a Gauge symmetry $\mathcal{R}_\theta \colon (A, B) \mapsto (e^{\mathrm{i}\theta}A, e^{\mathrm{i}\theta}B)$. Furthermore, it possesses a pair of conserved quantities. We will introduce these after further transformations.

*Remark* 2.3. In practice, we compute this transformation as a composition of coordinate changes, each accurate up to a certain order in $\mu$ and $|A|, |B|$. We use the notation $\Phi_{p,q}$ for a polynomial with degree $p$ in $A$ and $B$, and degree $q$ in $\mu$. In our case, we first compute the cubic (in $|A|, |B|$) polynomial $\Phi_{3,0}$ with $\mu = 0$. Then we compute the lowest order $\mu$-dependent polynomial $\Phi_{1,1}$ (which turns out to be linear in both $\mu$ and $|A|, |B|$). Indeed, the transformation $\mathrm{Id} + \Phi_{3,0}$ has no effect on the $\mu$-dependent, $|A|, |B|$-linear terms of the vector field and vice versa for $\Phi_{1,1}$. Now the transformation of the

lemma is precisely the composition $\mathrm{Id}+\Phi(A,B;\mu) = (\mathrm{Id}+\Phi_{3,0}) \circ (\mathrm{Id}+\Phi_{1,1})$. For more detail on how the normal form transformations at different orders depend on each other, see [30, §3.2.3].

Using the algorithm from [30] we compute the vector coefficients in the polynomial for $N = 1$. The computations essentially amount to applications of the Fredholm alternative and solving systems of four linear equations.

**Lemma 2.7** (Normal Form Transformation)**.** *Let $\mathcal{V}$ be the neighborhood guaranteed by Lemma 2.6. For any $\mu \in \mathcal{V}$, a polynomial satisfying the conditions of Lemma 2.6 with $N = 1$ is*

$$\Phi_{1,1}(A,B;\mu) = \mu \begin{bmatrix} \frac{-3}{16} & \frac{-\mathrm{i}}{8} & \frac{3}{16} & \frac{-\mathrm{i}}{8} \\ \frac{i}{8} & \frac{-3}{16} & \frac{-\mathrm{i}}{8} & \frac{-1}{16} \\ \frac{3}{16} & \frac{i}{8} & \frac{-3}{16} & \frac{i}{8} \\ \frac{i}{8} & \frac{-1}{16} & \frac{-\mathrm{i}}{8} & \frac{-3}{16} \end{bmatrix} \begin{bmatrix} A \\ B \\ \overline{A} \\ \overline{B} \end{bmatrix} \tag{2.15}$$

*Proof.* There are two methods of proof. First, we could simply show that this polynomial satisfies the two conditions. This is routine enough that the reader may verify it independently. Second, we could show the explicit construction of this polynomial which follows the proof of the general normal form. This construction is included in Appendix A. □

*Remark* 2.4. Lemma 2.7 describes a smooth unfolding of the $\mu$-dependent linear terms in the equation (2.12). This contrasts with a classical Jordan normal form transformation of these terms which is not smooth in $\mu$. In this context, the lemma may be compared to Section 3.2.2 of [30] or to the original source [5].

### 2.3.3 Additional Transformations

To conclude this section we introduce two other coordinate transformations which eventually put our equations into a form that is simply an $\varepsilon$-perturbation of the Ginzburg-Landau equations discussed in Section 2.2. It is worth noting that while the normal form transformation depends on $\varepsilon$, the transformations discussed here do not, and thus they

will each be applied across the full real line. A representation of all the transformations discussed here, as well as the normal form transformations can be found in Figure 2.3.

**Lemma 2.8.** *There exists a change of coordinates which transforms Equation* (2.14) *into*

$$\begin{bmatrix} a' \\ b' \end{bmatrix} = \begin{bmatrix} 0 & 1 \\ 0 & 0 \end{bmatrix} \begin{bmatrix} a \\ b \end{bmatrix} + \begin{bmatrix} i\varepsilon\widetilde{P}(a,b;\varepsilon) & 0 \\ \widetilde{Q}(a,b;\varepsilon) & i\varepsilon\widetilde{P}(a,b;\varepsilon) \end{bmatrix} \begin{bmatrix} a \\ b \end{bmatrix} + \varepsilon^{N-2}\tilde{g}(a,b,y/\varepsilon;\varepsilon) \tag{2.16}$$

*where the transformed terms in normal form are*

$$\begin{aligned} \widetilde{P}(a,b;\varepsilon) &= \operatorname{sgn}(x)\frac{1}{4} + \frac{3}{8}|a|^2 + \mathcal{O}\left(\varepsilon^2\right) \\ \widetilde{Q}(a,b;\varepsilon) &= \operatorname{sgn}(x) + |a|^2 + \varepsilon\frac{i}{8}(a\bar{b} - \bar{a}b) + \mathcal{O}(\varepsilon^3) \end{aligned}$$

*and the remainder term $\tilde{g} = \mathcal{O}((|a| + \varepsilon|b|)^N)$ is periodic in the third variable.*

*Proof.* The transformation of the lemma may be realized as a composition of two transformations. First, we move to a co-rotating frame of reference. Second, we rescale $a, b$, and space $x$.

**A co-rotating reference frame** Consider the normal form in equations (2.13). Since $iA$ and $iB$ appear in $A_x$ and $B_x$ respectively, solutions to the normal form "rotate" in $\mathbb{C}^2$. In this section, we employ a coordinate transformation which puts the equations in a co-rotating reference frame. Furthermore, terms in the normal form with degree $\geq 1$ are unaffected by changing to this co-rotating frame of reference.

To move to the co-rotating frame, we append an equation for the rotation variable $\rho \in S^1$ so that we have the system

$$\begin{bmatrix} A_x \\ B_x \end{bmatrix} = \begin{bmatrix} i & 1 \\ 0 & i \end{bmatrix} \begin{bmatrix} A \\ B \end{bmatrix} + \begin{bmatrix} iP(A,B;\mu) & 0 \\ Q(A,B;\mu) & iP(A,B;\mu) \end{bmatrix} \begin{bmatrix} A \\ B \end{bmatrix} + G(A,B;\mu) \tag{2.17}$$

$$\rho_x = i\rho. \tag{2.18}$$

Now the full state space is $\mathbb{C}^2 \times S^1$. Consider the diffeomorphism

$$\begin{aligned} \mathrm{P}\colon \mathbb{C}^2 \times S^1 &\to \mathbb{C}^2 \times S^1 \\ (a, b, \rho) &\mapsto \mathrm{P}(a, b, \rho) = (\rho a, \rho b, \rho) \end{aligned}$$

where we treat $\rho \in S^1$ as $\rho \in \mathbb{C}$ with $|\rho| = 1$. Setting $(A, B, \rho) = \mathrm{P}(A_1, B_1, \rho)$ gives us the change of coordinates

$$A = A_1\rho \qquad B = B_1\rho \qquad \rho = \tilde{\rho}.$$

This leads to the equations in the co-rotating frame[3]

$$\begin{aligned} \begin{bmatrix} A_{1x} \\ B_{1x} \end{bmatrix} &= \begin{bmatrix} 0 & 1 \\ 0 & 0 \end{bmatrix} \begin{bmatrix} A_1 \\ B_1 \end{bmatrix} + \begin{bmatrix} iP(A_1, B_1; \mu) & 0 \\ Q(A_1, B_1; \mu) & iP(A_1, B_1; \mu) \end{bmatrix} \begin{bmatrix} A_1 \\ B_1 \end{bmatrix} + g(A_1, B_1, \rho; \mu) \\ \rho_x &= i\rho. \end{aligned} \tag{2.19}$$

where $g(A_1, B_1, \rho; \mu) = \rho^{-1}G(\rho A_1, \rho B_1; \mu)$ represents the transformed higher order terms. Notice that we have eliminated the $iA$ and $iB$, which represent the "rotational part" of the equation in normal form.

The key in computing the new equations is the fact that $P(A, B; \mu) = P(A_1, B_1; \mu)$ and similarly for $Q$. Indeed, recall that the the arguments of both $P, Q$ are quite particular

$$P(A, B; \mu) = P(|A|^2, \tfrac{\mathrm{i}}{2}(A\overline{B} - \overline{A}B); \mu), \qquad Q(A, B; \mu) = Q(|A|^2, \tfrac{\mathrm{i}}{2}(A\overline{B} - \overline{A}B); \mu).$$

Notice that

$$\begin{aligned} |A|^2 = |\rho a|^2 = |A_1|^2 \qquad \text{and} \qquad A\overline{B} - \overline{A}B &= \rho a \rho^{-1}\overline{b} - \rho^{-1}\overline{a}b \\ &= A_1\overline{B}_1 - \overline{A}_1 B_1. \end{aligned}$$

Thus $P(A, B; \mu) = P(A_1, B_1; \mu)$ and similarly for $Q$. This is a direct result of the

[3]We drop the ˜ on $\rho$ for convenience.

symmetry built into the normal form for a $1\colon 1$ resonance.

**Rescaling** Next we rescale $A_1, B_1$ and $x$. Define the diffeomorphism

$$\begin{aligned}\tau\colon \mathbb{C}^2 \times S^1 &\to \mathbb{C}^2 \times S^1\\ (a,b,\rho) &\mapsto \tau(a,b,\rho) = (\frac{\sqrt{\mu}}{\sqrt{3}}a, \frac{\mu}{2\sqrt{3}}b, \rho)\end{aligned}$$

Setting $(A_1, B_1, \rho, x) = (\tau(a,b,\rho), \frac{2}{\sqrt{\mu}}\tilde{x})$ gives us the rescaling coordinate transformation

$$A_1 = \frac{\sqrt{\mu}}{\sqrt{3}}a \qquad B_1 = \frac{\mu}{2\sqrt{3}}b \qquad \rho = \rho \qquad x = \frac{2}{\sqrt{\mu}}\tilde{x}. \tag{2.20}$$

Applying this to equations (2.19) yields

$$\begin{bmatrix} a' \\ b' \end{bmatrix} = \begin{bmatrix} 0 & 1 \\ 0 & 0 \end{bmatrix} \begin{bmatrix} a \\ b \end{bmatrix} + \begin{bmatrix} \sqrt{\mu}\tilde{P}(a,b;\mu) & 0 \\ \tilde{Q}(a,b;\mu) & \sqrt{\mu}\tilde{P}(a,b;\mu) \end{bmatrix} \begin{bmatrix} a \\ b \end{bmatrix} + \mu^{\frac{N-2}{2}}\tilde{g}(a,b,\rho;\mu)$$
$$\rho_y = i\frac{2}{\sqrt{\mu}}\rho.$$

where $' = \frac{d}{d\tilde{x}}$ and the transformed terms in normal form are

$$\begin{aligned}\tilde{P}(a,b,\mu) &= \operatorname{sgn}(x)\frac{\mathrm{i}}{4} + \frac{3i}{8}|a|^2 + \mathcal{O}\left(|\mu|\right)\\ \tilde{Q}(a,b,\mu) &= \operatorname{sgn}(x) + |a|^2 + \sqrt{\mu}\frac{\mathrm{i}}{8}(a\bar{b} - \bar{a}b) + \mathcal{O}(|\mu^{3/2}|)\end{aligned}$$

and the transformed terms not in normal form $\tilde{g} = \mathcal{O}((|a+\sqrt{\mu}|b|)^N)$ . We can eliminate the third equation by solving it for $\rho = \exp\left(2i\frac{\tilde{x}}{\sqrt{\mu}}\right)$ and plugging into $\tilde{g}$. Using the fact that $\mu = \varepsilon^2$, we have the equations (2.16) in the statement of the lemma. Notice that now, if we could take the singular limit $\varepsilon \to 0$, we would have precisely the equations (2.3) of Section 2.2. □

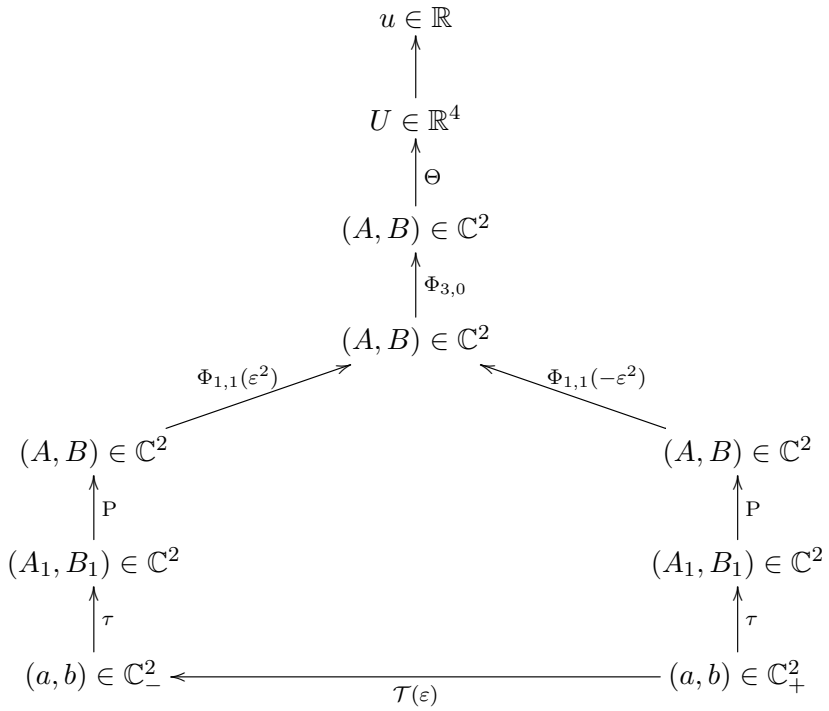


Figure 2.3: A schematic summary of transformations and variables.

## 2.4 Persistence of GL Dynamics

In this section, we describe how the dynamics of the full SH normal form equation (2.16) are approximated by the GL amplitude equations (2.3) of Section 2.2. Specifically, we describe the equilibria, periodic orbits, and invariant manifolds of (2.16) as being the same as those in (2.3) with an order-$\varepsilon$ correction. We separate the section into two steps. The first step uses standard ODE theory for the smoothness of invariant manifolds in parameters and includes explicit computation of this leading-order correction. In the second step, we consider terms not in the normal form as a rapidly oscillating perturbation use ideas from [21, 22, 39].

We drop the $\tilde{}$ on $\tilde{x}$, for notational convenience.

### 2.4.1 Dynamics of the Truncated Normal Form

By removing the terms not in normal form, $\varepsilon^{N-2}\tilde{g}$, from (2.16) we obtain the truncated normal form equation

$$\begin{bmatrix} a_y \\ b_y \end{bmatrix} = \begin{bmatrix} 0 & 1 \\ 0 & 0 \end{bmatrix} \begin{bmatrix} a \\ b \end{bmatrix} + \begin{bmatrix} i\varepsilon\widetilde{P}(a,b;\varepsilon) & 0 \\ \widetilde{Q}(a,b;\varepsilon) & i\varepsilon\widetilde{P}(a,b;\varepsilon) \end{bmatrix} \begin{bmatrix} a \\ b \end{bmatrix}, \tag{2.21}$$

where

$$\begin{aligned} \widetilde{P}(a,b;\varepsilon) &= \operatorname{sgn}(x)\frac{1}{4} + \frac{3}{8}|a|^2 + \mathcal{O}\left(\varepsilon^2\right) \\ \widetilde{Q}(a,b;\varepsilon) &= \operatorname{sgn}(x) + |a|^2 + \varepsilon\frac{i}{8}(a\bar{b} - \bar{a}b) + \mathcal{O}(\varepsilon^3). \end{aligned}$$

We justify this truncation in the next section. For now, we describe the dynamics of the truncated normal form by computing the order-$\varepsilon$ correction to the dynamical structures of (2.3).

Before proceeding, we point out that, for $x > 0$ or $x < 0$, this truncated equation is equivariant under the reversibility symmetry $\mathbf{S}$ and also the Gauge symmetry $\mathcal{R}_\theta$. Additionally, it has conserved quantities

$$\begin{aligned} M &= -\frac{i}{2}(a\bar{b} - \bar{a}b) = \operatorname{Im}(a\bar{b}) \\ H^{\pm}(\varepsilon) &= |b|^2 \mp |a|^2 - \tfrac{1}{2}|a|^4 + \varepsilon\tfrac{1}{4}|a|^2 M + \mathcal{O}(\varepsilon^2). \end{aligned} \tag{2.22}$$

These conserved quantities may be computed by applying the transformation of the lemma to the conserved quantities of the normal form, found in [30, §4.3.3].

#### Dynamics for $x > 0$

First, let us restrict to the positive half-line $x > 0$. Recall from Section 2.2.1 the stable manifold of the origin invariant under the GL equations

$$\mathcal{W}^s = \left\{ \left( e^{\mathrm{i}\phi} r, e^{\mathrm{i}\phi}\sqrt{r^2 + 1/2r^4} \right) \mid r \in \mathbb{R}_{\geq 0}, \theta \in [0, 2\pi) \right\}.$$

**Lemma 2.9.** *For sufficiently small $\varepsilon > 0$, the stable manifold of $(0,0)$ in equation (2.4) persists in equation (2.21) as $\mathcal{W}^s(\varepsilon)$. Furthermore, the two manifolds $\mathcal{W}^s$ and $\mathcal{W}^s(\varepsilon)$*

*differ by at most an $\varepsilon^2$-order correction.*

*Proof.* Persistence is guaranteed by standard ODE theory. All that remains is to show that the $\mathcal{O}(\varepsilon)$ term in the expansion for $\mathcal{W}^s(\varepsilon)$ is 0.

To see this, recall the conserved quantities $M$ and $H^+(\varepsilon)$ expressed in equation (2.22). We compute that $\{\nabla M, \nabla H^-(0)\}$ are linearly independent. Thus the level set $\{M \equiv 0, \quad H^-(\varepsilon) \equiv 0\}$ is a manifold with an explicit approximation for small $\varepsilon > 0$. Since this level set contains the origin, it contains the stable manifold $\mathcal{W}^s(\varepsilon)$ (thus providing us with an approximate expression for $\mathcal{W}^s(\varepsilon)$). Notice that the leading-order $\varepsilon$ of the conserved quantity $H^+(\varepsilon)$ appears with a factor $M$. Since $M \equiv 0$ on $\mathcal{W}^s(\varepsilon)$, this order-$\varepsilon$ term has no effect. □

**Dynamics for $x < 0$**

Restricting to the negative half-line $x < 0$, recall the GL amplitude equations (2.5) posses a normally hyperbolic family of periodic orbits $\mathcal{P}$ with center unstable foliation $\mathcal{W}^{cu}_{\mathcal{P}}$.

**Lemma 2.10.** *For sufficiently small $\varepsilon > 0$, the family of periodic orbits $\mathcal{P}$ for* (2.5) *persists in equations* (2.21) *as $\mathcal{P}(\varepsilon)$ with periodic orbits given at leading order by*

$$a_{per}(k;\varepsilon) = e^{ikx}\left(\sqrt{1-k^2} - \varepsilon\frac{k^3}{4\sqrt{1-k^2}} + \mathcal{O}(\varepsilon^2)\right)$$
$$b_{per}(k;\varepsilon) = e^{ikx}\left(\mathrm{i}k\sqrt{1-k^2} - \varepsilon\frac{-5k^4+4k^2-1}{8\sqrt{1-k^2}} + \mathcal{O}(\varepsilon^2)\right).$$

*The center unstable foliation $\mathcal{W}^{cu}_{\mathcal{P}}$ also persists as $\mathcal{W}^{cu}_{\mathcal{P}}(\varepsilon)$ and is given by an $\varepsilon$-order correction of the original. In particular, it can be expressed as the level set of the conserved quantities* (2.22) *evaluated at the periodic orbits $M|_{(a_{per},b_{per})}, H^+|_{(a_{per},b_{per})}$.*

*Proof.* Again, standard ODE theory guarantee's persistence and we need only compute the leading order expansion in $\varepsilon$.

Since (2.21) is equivariant under the Gauge symmetry $\mathcal{R}_\theta$, we may assume that the

periodic orbits have the form

$$\begin{aligned} a_{\text{per}}(k;\varepsilon) &= s(k;\varepsilon)e^{iky} \\ b_{\text{per}}(k;\varepsilon) &= \left(p(k;\varepsilon) + iq(k;\varepsilon)\right)e^{iky} \end{aligned}$$

for real functions $s, p, q\colon (-\frac{1}{\sqrt{3}}, \frac{1}{\sqrt{3}}) \to \mathbb{R}$. It is sufficient to restrict to a real amplitude for $a_{\text{per}}$ because we may combine the Gauge symmetry with the translation invariance to "rotate" the solution pair so that $a_{\text{per}}$ is real when $x = 0$. Plugging $(a_{\text{per}}, b_{\text{per}})$ into (2.21), we find that

$$\begin{aligned} s(k;\varepsilon) &= \sqrt{1-k^2} - \varepsilon\frac{k^3}{4\sqrt{1-k^2}} + \mathcal{O}(\varepsilon^2) \\ p(k;\varepsilon) &= 0 + \mathcal{O}(\varepsilon^2) \\ q(k;\varepsilon) &= k\sqrt{1-k^2} - \varepsilon\frac{-5k^4+4k^2-1}{8\sqrt{1-k^2}} + \mathcal{O}(\varepsilon^2). \end{aligned}$$

Next, we must investigate the $\mathcal{O}(\varepsilon)$ terms of $\mathcal{W}^s_{\mathcal{P}(\varepsilon)}$. As in the $x > 0$ case, a direct computation shows that $\{\nabla M, \nabla H^+(0)\}$ are linearly independent. Thus, the level set of the conserved quantities forms a manifold with an expression valid for small $\varepsilon > 0$.

Evaluating each of the conserved quantities at the relative equilibria $(a_{\text{per}}, b_{\text{per}})$, we obtain functions of $k, \varepsilon$

$$\begin{aligned} \mathcal{M}(k;\varepsilon) &:= M|_{(a_{\text{per}},b_{\text{per}})} = -k(1-k^2) + \varepsilon\frac{1}{8}(7k^4-4k^2+1) + \mathcal{O}(\varepsilon^2) \\ \mathcal{H}(k;\varepsilon) &:= H^-(\varepsilon)|_{(a_{\text{per}},b_{\text{per}})} = \frac{1}{2}(1-k^2)(1+3k^2) + \varepsilon\frac{1}{2}k(-4k^4+3k^2-1) + \mathcal{O}(\varepsilon^2). \end{aligned} \tag{2.23}$$

For each $k^2 < \frac{1}{3}$, the level set $\{M \equiv \mathcal{M}(k;\varepsilon), \quad H^-(\varepsilon) \equiv \mathcal{H}(k;\varepsilon)\}$ is a manifold containing the periodic orbit $(a_{\text{per}}, b_{\text{per}})(k;\varepsilon)$ and thus contains the unstable manifold of that periodic solution. Thus, we have an expression for the leading-order approximation of the center unstable foliation of the periodic orbits

$$\mathcal{W}^{cu}_{\mathcal{P}}(\varepsilon) \subseteq \bigcup_{k^2<\frac{1}{3}} \{M = \mathcal{M}(k;\varepsilon), \quad H^+(\varepsilon) = \mathcal{H}(k;\varepsilon)\}.$$

□

### 2.4.2 Rapidly Oscillating Perturbations

In this section we justify comparing the dynamics of equation (2.16) to the dynamics of the truncated normal form equation (2.21). Recall that the terms not in normal form $\tilde{g}(a, b, \tilde{x}/\varepsilon; \varepsilon)$ are periodic in the third variable, due to a factor $\sim e^{\tilde{x}/\varepsilon}$. Thus, since $\varepsilon > 0$ is small, we consider (2.16) as a rapidly oscillating perturbation of (2.21). From this framework, we can justify the truncation of $\tilde{g}$ by applying theorems on the persistence of invariant manifolds from [21, 22, 39]. This is primarily a technical consideration, and should not distract too much from the larger story.

**The $x > 0$ case**

**Lemma 2.11.** *For sufficiently small $\varepsilon > 0$, the stable manifold $\mathcal{W}^s(\varepsilon)$ of $(0, 0)$ in equation (2.21) persists in equation (2.16) with an $\varepsilon^{N-2}$-order correction.*

*Proof.* We will apply Theorem A' from [21] which says that the invariant manifolds of near-identity diffeomorphisms varies only by terms of high order in the parameter. To put our problem in the form of the theorem, let $V = \begin{bmatrix} a \\ b \end{bmatrix} \in \mathbb{C}^2$ and let $\phi_x(V)$ be the flow associated to the truncated equation (2.21).

Define a family of diffeomorphisms

$$\begin{aligned} G_\varepsilon &: \mathbb{C}^2 \to \mathbb{C}^2 \\ &V \mapsto G_\varepsilon(V) = \phi_\varepsilon(V). \end{aligned}$$

Similarly, let $\psi_{y,z}(V)$ be the evolution operator associated to the full equation (2.16). Recall that $\psi_{y,z}$ acts on a solution $V$ by $\psi_{y,z}(V(z)) = V(y)$. Define a second family of diffeomorphisms to be the period maps $\phi_{\pi\varepsilon,0}$

$$\begin{aligned} F_\varepsilon &: \mathbb{C}^2 \to \mathbb{C}^2 \\ &V \mapsto F_\varepsilon(V) = \psi_{\pi\varepsilon,0}(V) \end{aligned}$$

Noticing that for $\varepsilon = 0$ both $F_\varepsilon = G_\varepsilon = \mathrm{Id}$, we can expand

$$G_\varepsilon = \mathrm{Id} + G_1\varepsilon + G_2\varepsilon^2 + \cdots$$
$$F_\varepsilon = \mathrm{Id} + F_1\varepsilon + F_2\varepsilon^2 + \cdots .$$

In fact, by expanding solutions in terms of $\varepsilon$, we can show that $G_i = F_i$ for $i \leq N-2$, where $N$ is the order of the normal form used in Section 2.3. Therefore we know that $G_\varepsilon - F_\varepsilon = \mathcal{O}(\varepsilon^{N-2})$.

Since $(0,0) \in \mathbb{C}^2$ is a hyperbolic fixed point of both sets of equations, it is also a hyperbolic fixed point of the diffeomorphisms defined above. In fact, again by expansions, we have

$$\mathrm{Spec}\,(DF_\varepsilon(0)) = \mathrm{Spec}\,(DG_\varepsilon(0)) = \{1 \pm \varepsilon i + \mathcal{O}(\varepsilon^2)\}.$$

Let $W_{G_\varepsilon}, W_{F_\varepsilon}$ be the stable manifolds of $G_\varepsilon, F_\varepsilon$ respectively. The uniqueness of the stable manifold implies that $W_{G_\varepsilon} = \mathcal{W}^s(\varepsilon)$ and $W_{F_\varepsilon}$ is the stable manifold of $(0,0)$ in the full equation (2.16). Theorem A' in [21] implies that the stable manifold $W_{F_\varepsilon}$ is close to $W_{G_\varepsilon}$ by a factor of $\varepsilon^{N-2}$. Thus we have shown that

$$= W_{F_\varepsilon} = W_{G_\varepsilon} + \mathcal{O}(\varepsilon^{N-2}) = \mathcal{W}^s(\varepsilon) + \mathcal{O}(\varepsilon^{N-2}).$$

□

With a small abuse of notation, we henceforth use $\mathcal{W}^s(\varepsilon)$ to denote the stable manifold of $(0,0)$ in the full equation (2.16).

**The $x < 0$ Case**

**Lemma 2.12.** *For sufficiently small $\varepsilon > 0$, the family of periodic orbits $\mathcal{P}(\varepsilon)$ and its center unstable foliation, from* (2.21)*, persist in equation* (2.16)*. Each differs from its original by only an order $\varepsilon^{N-2}$-correction.*

To prove persistence in this lemma, we could again use the result of [21, 22] to construct an argument similar to that used in the $x > 0$ case. This would amount to a similarly tedious application in a more complicated situation. We instead refer the reader to [39]. where the authors show persistence of the desired objects. In [39], the

authors are specifically concerned with a vector field that satisfies the exact hypotheses of the normal form used in Section 2.3. They make use of the Hamiltonian structure of the normal form and also include more advanced ideas such as exponential dichotomies. While quite direct, their method is not generalizable as our argument using [21].

## 2.5 Computing a Strain-Displacement Relation

### 2.5.1 Different Phase Spaces

As mentioned above, Lemmas 2.6–2.8 are valid for $x < 0$ or $x > 0$, but not both together. In particular, the normal form transformation of Lemma 2.7 can be computed for $\varepsilon^2$ and for $-\varepsilon$ independently. This yields two distinct transformations, two distinct pairs of equations, and two separate phase spaces $\mathbb{C}^2_-, \mathbb{C}^2_+$. See Figure 2.3. Recall that our goal is a heteroclinic gluing argument; we wish to intersect an unstable manifold in $\mathbb{C}^2_-$ with a stable manifold in $\mathbb{C}^2_+$. We have already computed leading-order approximations for these manifolds in Section 2.4. However, since these manifolds do not lie in the same phase spaces, such an intersection is meaningless without some further justification. The next lemma provides the appropriate coordinate transformations to "move" the unstable manifold from the phase space $\mathbb{C}^2_-$ of the $\tilde{x} < 0$ dynamics to the phase space $\mathbb{C}^2_+$ of the $\tilde{x} > 0$ dynamics. Then an intersection computed in the second phase space will meaningfully represent a transition from one invariant manifold to the second.

**Lemma 2.13.** *For each $\varepsilon > 0$ sufficiently small, there exists a non-autonomous transformation $\mathcal{T}$ that maps the $\tilde{x} > 0$ phase space to the $\tilde{x} < 0$ phase space $\mathcal{T}\colon \mathbb{C}^2_+ \to \mathbb{C}^2_-$. This transformation is defined by*

$$\mathcal{T}(\varepsilon) := \tau^{-1} \circ \mathrm{P}^{-1}[\mathrm{Id} + \Phi_{1,1}(\varepsilon^2)]^{-1}[\mathrm{Id} + \Phi_{1,1}(-\varepsilon^2)] \circ \mathrm{P} \circ \tau \tag{2.24}$$

$$= \mathrm{Id} + \varepsilon \begin{bmatrix} 0 & 0 & 1 & 0 \\ \frac{-\mathrm{i}}{2} & 0 & \frac{i}{2}e^{-2ix} & 0 \\ 0 & 0 & 0 & 0 \\ \frac{-\mathrm{i}}{2}e^{2ix} & 0 & 0 & \frac{i}{2} \end{bmatrix} + \mathcal{O}(\varepsilon^2). \tag{2.25}$$

*Proof.* Figure 2.3 shows how we arrive at the composition above. The form on the second line is obtained by direct computation. The key part is the composition of normal form

transformations $[\mathrm{Id}+\Phi_{1,1}(\varepsilon^2)]^{-1}[\mathrm{Id}+\Phi_{1,1}(-\varepsilon^2)]$, which is discussed in Appendix A $\square$

Now we may apply this transformation to the stable manifold of $(0,0)$ in the $\tilde{x}>0$ dynamics. We compute a leading-order expression for the moved stable manifold

$$\begin{aligned}\widehat{\mathcal{W}}^s(\varepsilon) &:= \mathcal{T}(\varepsilon)\left[\mathcal{W}^s(\varepsilon)\right] \\ &= \mathcal{T}(\varepsilon)\mathcal{W}^s + \mathcal{O}(\varepsilon^2) \\ &= \left\{ e^{\mathrm{i}\phi}\left(r, \sqrt{r^2+\tfrac{1}{2}r^4} + \varepsilon(-ir/2 + ire^{-2i\phi}/2)\right) + \mathcal{O}(\varepsilon^2) \mid r>0, \phi\in[0,2\pi)\right\}.\end{aligned} \tag{2.26}$$

Now we may legitimately compare this object with the center unstable foliation of periodic orbits $\mathcal{W}^{cu}_{\mathcal{P}}(\varepsilon)$.

### 2.5.2 Intersection with $\varepsilon > 0$

Recall that Lemma 2.2 established an intersection of invariant manifolds for the GL amplitude equations (2.3). That intersection reappears in (2.16) when $\varepsilon = 0$ and the work of Section 2.4 suggests that it persists for $\varepsilon > 0$. Here we prove that the $\varepsilon = 0$ intersection is transverse, and thus does indeed persist for small $\varepsilon$. Additionally, we compute which values of $k$ occur in the intersection as function of $\varepsilon$, at leading-order.

**Lemma 2.14.** *For $\varepsilon = 0$, the intersection $\widehat{\mathcal{W}}^{cu}_{\mathcal{P}}(\varepsilon) \cap \mathcal{W}^s(\varepsilon)$ in the phase space of* (2.16) *is 1-dimensional and transverse.*

*Proof.* The intersection $\widehat{\mathcal{W}}^{cu}_{\mathcal{P}}(0) \cap \mathcal{W}^s(0)$ is a circle, as discussed in Lemma 2.2

Let $\varepsilon > 0$ be sufficiently small that the normal form theorems and persistence lemmas all apply. Recall that the center unstable foliation of periodic orbits $\mathcal{W}^{cu}_{\mathcal{P}}(\varepsilon)$ is equal to the $\varepsilon = 0$ version with an order-$\varepsilon$ correction. By appending $\mathcal{O}(\varepsilon)$ terms to our previous parametrization, we have the following leading-order parameterization of the bounded branch

$$\begin{aligned}\mathcal{W}^{cu}_{\mathcal{P},\mathrm{bdd}}(\varepsilon) &= \mathcal{W}^{cu}_{\mathcal{P},\mathrm{bdd}} + \mathcal{O}(\varepsilon) \\ &= \left\{ e^{\mathrm{i}\psi}\left(a_d(x;k), b_d(x;k)\right) + \mathcal{O}(\varepsilon) \mid x\in\mathbb{R}, \psi\in[0,2\pi), k^2 < 1/3\right\}.\end{aligned}$$

We leave the $\mathcal{O}(\varepsilon)$ terms undetermined, as they have no effect on the following calculation.

Define $F(r, \phi, y, k; \psi, \varepsilon)$ as the difference of the parameterizations for the moved stable manifold $\widehat{\mathcal{W}}^s(\varepsilon)$ and the bounded branch of the center unstable foliation of periodic orbits $\mathcal{W}^{cu}_{\mathcal{P}}(\varepsilon)$. Thus, by the $\varepsilon = 0$ intersection of Lemma 2.5, we have $F(\frac{1}{2}, \phi, \sqrt{2}\arctan\frac{1}{2}, 0; \phi - \frac{\pi}{2}, 0) = 0$ for any $\phi$. After a calculation, we find that for any $\phi \in [0, 2\pi)$ we have

$$\det\left(D_{(r,\psi,\tilde{x},k)}F(\tfrac{1}{2}, \phi, \sqrt{2}\arctan\tfrac{1}{2}, 0; \phi - \tfrac{\pi}{2}, 0)\right) = -4$$

So the derivative of $F$ is invertible at the intersection. This invertibility is equivalent to transversality in the sense described in Section 1.3.4. □

Going further, the Implicit Function Theorem implies existence of a nearby zero of $F$ for $\varepsilon > 0$ in a neighborhood of $\mathbb{R}_{\geq 0}$. This implies that the intersection persists for small $\varepsilon$. Our goal is to use an explicit expression for this intersection to obtain the order-$\varepsilon$ correction to the wavenumbers $k$ that occur in this intersection. To do so, we will need to use the conserved quantities in (2.22). Again using the same parameterization for $\widehat{\mathcal{W}}^s(\varepsilon)$, we evaluate the conserved quantities on the moved stable manifold

$$\begin{aligned} M|_{\widehat{\mathcal{W}}^s(\varepsilon)} &= \varepsilon\frac{r^2}{2}(1 - \cos 2\phi) \\ H^-(\varepsilon)|_{\widehat{\mathcal{W}}^s(\varepsilon)} &= 2r^2 + \varepsilon r\sqrt{r^2 + \tfrac{1}{2}r^4}\sin 2\phi + \varepsilon^2(1 - \cos 2\phi)(r^2 + \frac{r^4}{8}). \end{aligned}$$

These now provide leading-order approximations for the level set, in the $\tilde{x} < 0$ phase space, which contains the transformed stable manifold $\widehat{\mathcal{W}}^s(\varepsilon)$. Comparing these expressions to the ones defining the level sets of the center unstable foliation $\mathcal{W}^{cu}_{\mathcal{P}}(\varepsilon)$ we have the following lemma.

**Corollary 2.15.** *For sufficiently small $\varepsilon > 0$, there is a one-dimensional intersection $\widehat{\mathcal{W}}^{cu}_{\mathcal{P}}(\varepsilon) \cap \mathcal{W}^s(\varepsilon)$. This intersection defines the strain-displacement relation*

$$k = \frac{\varepsilon}{8}\cos(2\phi) + \mathcal{O}(\varepsilon^2).$$

*Proof.* The first statement is a consequence of Lemma 2.14, by Thom transversality.

For the second, we set

$$M|_{\widehat{\mathcal{W}^s(\varepsilon)}} = \mathcal{M}(k;\varepsilon), \qquad \text{and} \qquad H^-(\varepsilon)|_{\widehat{\mathcal{W}^s(\varepsilon)}} = \mathcal{H}(k;\varepsilon),$$

Where $\mathcal{M}, \mathcal{H}$ are given by the expressions in (2.23) Next, expand in $\varepsilon$ and compare terms of the same order in $\varepsilon$. Solving the resulting system of equations, we obtain $k = \frac{\varepsilon}{8}\cos(2\phi)$ and $r = \frac{1}{2}$ as one solution.

When $\varepsilon = 0$, we know the intersection occurs at $k = 0$ and with $r = \frac{1}{2}$. By the transversality mentioned above, we know that the intersection persists and remains unique under the $\varepsilon$-perturbation. Other solution pairs $(k, r)$ do not have the property that $(k, r) \to (0, \frac{1}{2})$ as $\varepsilon \to 0$. □

### 2.5.3 Proof of Theorem 2.1

*Proof of Theorem 2.1.* Let $\mathcal{V} \subseteq \mathbb{R}_{\geq 0}$ be a neighborhood of 0 contained in the neighborhoods guaranteed by Lemmas 2.6 and 2.14. Take $\varepsilon \in \mathcal{V}$ and for each $\theta \in [0, 2\pi)$, let $(a, b)_\theta \in \mathbb{C}^2$ be a point on the intersection $\mathcal{W}^{cu}_{\mathcal{P}}(\varepsilon) \cap \widehat{\mathcal{W}^s}(\varepsilon)$ such that $\theta$ is the phase of the leading order terms of $a$ as in the parameterization in 2.26. The existence of $(a, b)_\theta$ is guaranteed by the Implicit Function Theorem in Lemma 2.14. Let $\Psi(\varepsilon^2) = \Theta \circ (\mathrm{Id} + \Phi_{3,0}) \circ (\mathrm{Id} + \Phi_{1,1}(\varepsilon^2))$ be the full normal form transformation from Section 2.3.2. Let $U(x;\phi)$ be a solution to equation (2.11) with initial condition

$$U(0;\phi) = \Psi(\varepsilon^2)\left(\mathrm{P} \circ \tau((a,b)_\theta)); \varepsilon^2\right).$$

Take $u(x;\phi) = U_1(x;\phi)$, the first component.

In the limit $x \to \infty$, since

$$[\Psi(\varepsilon^2)]^{-1}\left(\mathrm{P}^{-1} \circ \tau^{-1}(U(x;\phi))\right) \in \mathcal{W}^s(\varepsilon),$$

we know that $U(x;\phi)$ is on the stable manifold of $0 \in \mathbb{R}^4$. Thus $|u(x;\phi)| \to 0$ as $x \to \infty$.

Next, consider the behavior of $u$ as $x \to -\infty$. Note that $U(x;\phi)$ is on a strong unstable fiber of a periodic orbit

$$U^{\mathrm{per}}(x;\phi) = \Psi\left(\mathrm{P} \circ \tau((a_{\mathrm{per}}, b_{\mathrm{per}})(\tilde{x};k); \varepsilon^2\right) \qquad \text{where} \qquad k = \frac{\varepsilon}{8}\cos(2\theta) + \mathcal{O}(\varepsilon^2).$$

After applying the various transformations, we see that the first component is $U_1^{\text{per}}(x;\phi) = u_{\text{per}}(k_x x - \phi; k_x)$, a periodic function with wavenumber

$$k_x(\theta;\varepsilon) = 1 + \frac{\varepsilon^2}{16}\cos(2\theta) + \mathcal{O}(\varepsilon^4). \tag{2.27}$$

As $x \to -\infty$ we see that $|u(x;\phi) - u_{\text{per}}(k_x x - \phi; k_x)| = |U_1(x;\phi) - U_1^{\text{per}}(x;\phi)| \to 0$.

All that's left is to establish the relation between the phase $\theta$ at the intersection and the phase $\phi$ of the asymptotic pattern. By comparing the phase of the defect solutions $a_d(x;k)$ at the intersection $\mathcal{W}^{cu}_{\mathcal{P}}(\varepsilon) \cap \widehat{\mathcal{W}}^s(\varepsilon)$ and in the limit $x \to -\infty$, we can establish the relation

$$\phi(\theta;\varepsilon) = \theta - \frac{\varepsilon}{4\sqrt{2}}\cos(2\theta) + \mathcal{O}(\varepsilon^2).$$

Substituting this into (2.27), we obtain the same leading order expansion now with $\theta$ replaced by $\phi$

$$\begin{aligned} k(\phi;\varepsilon) &= 1 + \frac{\varepsilon}{16}\cos\left(2\left(\phi + \mathcal{O}(\varepsilon)\right)\right) + \mathcal{O}(\varepsilon^4) \\ &= 1 + \frac{\varepsilon^2}{16}\cos(2\phi) + \mathcal{O}(\varepsilon^3). \end{aligned}$$

□

## 2.6 Numerics and Extensions

### 2.6.1 Numerical Continuation of Striped Fronts

We found excellent agreement between our theory and values of $k_x, \phi$ computed using numerical continuation. Numerical computation of strain-displacement relations is equivalent to computing a family of heteroclinic orbits connecting a family of periodics to an equilibrium. Our particular approach, following [58, §5], uses numerical farfield-core decomposition. More specifically, we use an ansatz $u(x) = \chi(x)u_*(k_x x - \phi; k_x) + w(x)$ with $\chi$ a smoothed out characteristic function of $(-\infty, -\ell]$, for some $\ell \gg 1$. One solves for the correction $w$ and the parameters $k_x, \phi$ after adding artificial homogeneous Dirichlet boundary conditions at $\pm L$ and imposing a phase condition near $x = L$, to enforce

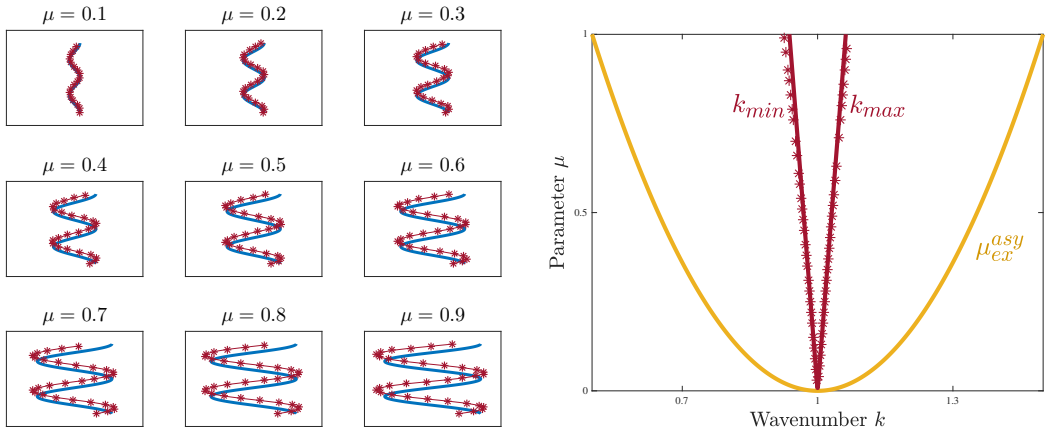


Figure 2.4: (a) Strain-Displacement relations computed with numerical continuation (red $*$) and predicted by theory (blue). Each curve is plotted with $k \in [0.92, 1.08]$, horizontal, and $\phi \in [-4.25, 4.25]$, vertical. (b) Maximal/minimal wavenumbers computed (red $*$) and predicted with/out (gold/red) jump-type inhomogeneity.

exponential localization of $w$.[4] The results indicate strong agreement with Theorem 2.1, even as $\mu$ approaches 1. See Figure 2.4.

### 2.6.2 Instabilities

Considering our one-dimensional stripe solutions $u_{\text{per}}(k_x x; k_x)$ as solutions of the planar Swift-Hohenberg equation without quadratic term

$$u_t = -(1+\Delta)^2 u + \mu u - u^3, \qquad u \in \mathbb{R} \qquad (x,y) \in \mathbb{R}^2. \tag{1.2}$$

with a homogeneous parameter $\mu \equiv \varepsilon^2$, we may study the spectrum of the linearization at $u_{\text{per}}$. It turns out that these stripes are linearly (and nonlinearly) stable only in a small subregion of the existence parabola in the $(k, \varepsilon)$ plane. The stability region is bounded by curves that are commonly referred to as the Eckhaus and zigzag boundaries, which possess asymptotic expansions near $\mu = 0$,

$$\mu_E = 3(1-k^2)^2 + \mathcal{O}((1-k^2)^3), \qquad (1-k^2) = -\mu_Z^2/512 + \mathcal{O}(\mu_Z^3).$$

[4] For details, see [58, §5] or Sections 3.5 and 4.1, where we execute a similar procedure for the amplitude equations of hexagonal patterns.

The Eckhaus boundary is present in one-dimensional systems, whereas the zigzag boundary invokes perturbations depending on $y$. See [52] and references therein for a detailed account of stability. We illustrate these stability boundaries in Figure 2.5.

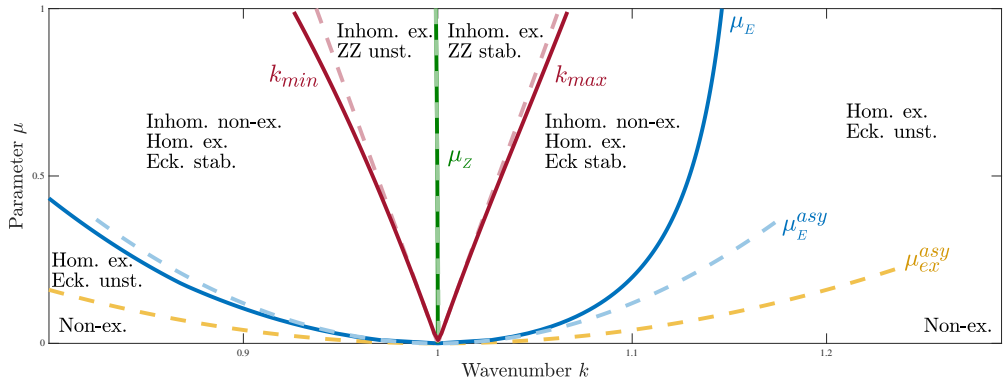


Figure 2.5: Regions of in/stability and existence for stripes in a system with homogeneous parameter and for half-stripes with a jump-type inhomogeneity; leading order asymptotics (dashed) and directly computed data (solid). See text for details.

After overlaying the regions of stability with the existence information (for both full stripes and striped fronts) contained in Figure 2.4, we have eight distinct regions. These appear in Figure 2.5 and are described in detail below, clockwise from bottom left:

- no stripes exist
  (Non-ex.)

- stripes exist with homogeneous parameter and are Eckhaus unstable, no striped fronts exist
  (Hom. ex., Eck. unst.)

- no striped fronts with inhomogeneity, full stripes exist and are Eckhaus stable but zigzag unstable
  (Inhom. non-ex., Hom. ex., Eck. stab.)

- striped fronts exist with inhomogeneity and are zigzag unstable, full stripes exist with previous stability
  (Inhom. ex., ZZ unst.)

- striped fronts exist and are stable, full stripes exist and are stable
  (Inhom. ex., ZZ stab.)
- no striped fronts exist, full stripes exist and are stable
  (Inhom. non-ex., Hom. ex., Eck. stab.)
- stripes exist and are Eckhaus unstable, no striped fronts exist
  (Hom. ex., Eck. unst.)
- no stripes exist
  (Non-ex.)

Note that half-stripes selected by the jump-type inhomogeneity have wavenumbers that are bounded away from the Eckhaus instability, but overlapping significantly with the zigzag-unstable region.

### 2.6.3 Growing Domain – Moving Inhomogeneity

The fact that the minimum selected wavenumber $k_{min}$ is zigzag unstable has dramatic consequences for pattern selection. However, the effects are not immediately visible in simulations because the system does not select a *unique* wavenumber. In particular, we would need to impose a condition $\phi \sim \pi/2$ on the phase in order to select $k_{min}$. This would represent an additional, external mechanism for selection. Instead, we pose our problem in the context of slowly growing domains and apply theory from [25]. We now illustrate a dramatic consequence of Theorem 2.1 with direct numerical simulations; the system self-selects a zigzag pattern.

Systems with slowly growing domains have been observed to exhibit pattern selection, e.g. in developing organisms in biology [42]. In [25], several model equations similar to ours are examined with a moving parameter inhomogeneity $\mu(x - ct)$ or on a linearly growing domain with boundary conditions. The main result is that the selected wavenumber $k_x$ depends on the speed $c$ according to

$$k_x(c) = k_{min} + \mathcal{O}(\sqrt{c})$$

where $k_{min}$ is the minimum wavenumber in the admissible band of wavenumbers occurring in the same system with a stationary parameter inhomogeneity. In our problem

(2.2), we expect $k_{min}$ to be zigzag unstable, see Figure 2.5. Thus, if we choose $c$ near 0, we may expect the system to select striped pattern solutions which are unstable to transverse perturbations.

### Simulations

We observed the selection and development of zigzag patterns in a direct numerical simulation of the problem (2.2) in two dimensions. We use a standard spectral method with $2^{11} \times 2^{11}$ Fourier modes, creating an effective $dx \approx 0.01$, and implicit Euler time stepping with $dt = 0.025$. All simulations are posed on a square domain with side

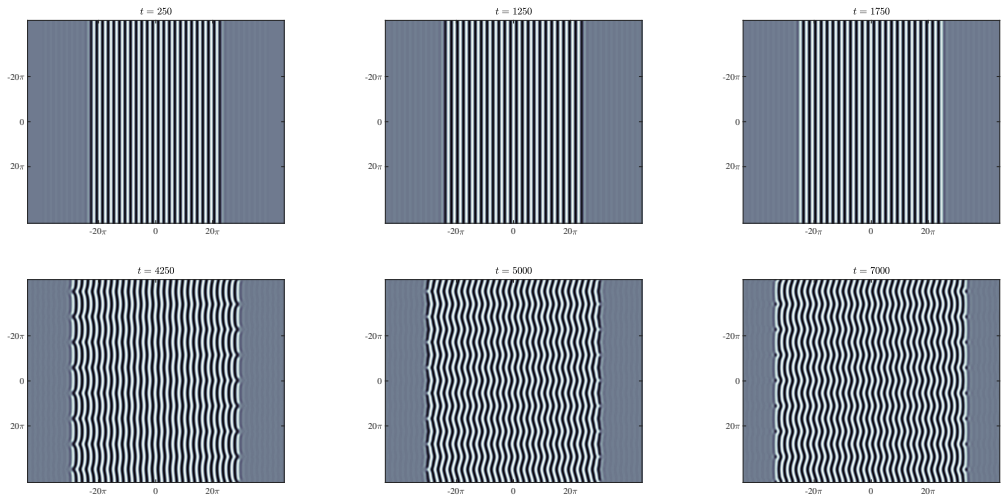


Figure 2.6: Snapshots from direct numerical simulation of the Swift-Hohenberg equation posed on a square domain with periodic boundary conditions; see text for detailed description. The simulation uses a spectral method with implicit Euler time-stepping and initial data that is periodic in the middle half of the domain and 0 elsewhere.

length $2L = 90\pi$ and periodic boundary conditions. We use a "plateau"-type parameter consisting of two jump-type inhomogeneities for compatibility with our periodic boundary conditions, which are necessary due to our use of a spectral method.[5] The two inhomogeneities move away from each other to emulate a growing domain. The size of both jumps is $\mu = \varepsilon^2 = 0.8$ and initial data is an even periodic pattern with initial

[5]The effect from the additional inhomogeneity is negligible, since such an effect decreases exponentially in the distance between jumps.

wavenumber $k_0$ in the middle half of the domain

$$u(x,y,0) = \begin{cases} \varepsilon\cos(k_0 x), & |x| < L/2 \\ 0, & |x| > L/2 \end{cases}.$$

We fix $c = 0.005$ and $k_0 = 1.05$. At $t_p = 1500$ we add a small, transverse perturbation

$$u_p(x,y,t_p) = \begin{cases} 0.1\cos\left(k_p x + 0.9\cos(8\pi y/L)\right), & |x| < L/2 + ct_p \\ 0, & |x| > L/2 + ct_p \end{cases}$$

where $k_p = 0.97125$ is the observable wavenumber achieved by the system at $t_p$ as numerically computed in independent trials.

Figure 2.6 shows snapshots for various $t$ values. When $t < 1500$, all stripes widen as the wavenumber decreases and the parameter plateau widens; no new stripes appear, should the reader choose to count. At $t = 1750$, a stripe has been added on the outside, indicating that the wavenumber has stopped decreasing. Also, notice that the transverse perturbation, added at $t = 1500$, is small enough that it is unobservable. At $t = 4250$ we can see the system moving away from the $y$-constant stripes. By $t = 5000$, the system seems to have relaxed to a stationary zigzag pattern. Indeed, for long times past $t = 7000$ the zigzag pattern remains stationary and continues to add new zigs and zags on the outside. We comment further on patterns in bounded regions in the next section.

## 2.7 Conclusions and Discussion

### Patterns in Bounded Regions

Experiments are usually performed in bounded domains, and one may therefore be interested in how the wavenumber selection mechanism described here interacts with left and right boundary conditions. In the center of the pattern-forming region, one expects that a strain-displacement relation is induced by the boundary at one side while the second boundary forces a different strain-displacement relation. Matching these two relations, and including correction terms that are exponentially small in the size of the

patterned region, has been carried out in [58, §5]. The result is a geometric subtraction (subtracting phases) and quantization (intersecting with $\phi = 2k_x L$) of the two strain-displacement relations. The argument there carries through in a straightforward fashion to the equivalent case of the parameter plateau used in simulations above,

$$\mu(x) = \begin{cases} \varepsilon^2, & |x| \leq L, \\ -\varepsilon^2, & |x| \geq L, \end{cases}$$

with $L$ large, confining the patterned region to a strip $|x| \leq L$. The set of equilibria can then be described "explicitly" in the thermodynamic limit of $L \to \infty$. Numerical results in a similar situation were presented in [25, Fig. 3].

**Boundary Conditions**

There is an undeniable analogy to be made between our problem (2.2) and the SH equation posed on a semi-infinite domain with Dirichlet boundary conditions

$$u_t = -\left(1 + \frac{\partial^2}{\partial x^2}\right)^2 u + \mu u - u^3, \qquad u \in \mathbb{R}, \qquad x \in [0, \infty) \qquad u(0,t) = u_x(0,t) = 0. \tag{2.28}$$

Problem (2.28) was formally and numerically explored during the early 1980s. In particular, the linear coefficient $\frac{1}{16}$ from our Theorem 2.1 also appears in [14, 20, 66]. The authors' methods use conserved quantities of amplitude equations introduced by [61] which are equivalent to our real Ginzburg-Landau equations (2.3) with $x < 0$. We have found no results from this period providing an explicit strain-displacement relation between the phase and wavenumber, although the idea is mentioned in [66].

On the other hand, one can envision a homotopy from parameter jump-type inhomogeneities to boundary conditions, treating parameter jumps $\mu(x) = \varepsilon^2$ for $x < 0$, as before, but $\mu(x) = -C\varepsilon^2 < 0$ for $x < 0$. Slightly generalizing our result to this scenario with $\mu = -C\varepsilon^2$ for some $C \geq 1$, one finds the same leading-order expansion with band width boundaries $1 \pm \varepsilon^2/16$ . Letting $C \to \infty$, or even using different scalings in $\mu$, one can arrive at Dirichlet boundary conditions in Ginzburg-Landau, or clamped boundary conditions in the SH equation, $u_x = u = 0$ at $x = 0$. It would be interesting to study

strain-displacement relations in such a broader class of parameter jumps, testing the universality of the $\varepsilon^2/16$-correction.

More recently, a similar boundary value problem was studied numerically through the strain-displacement framework in [58]. The main difference from our earlier analysis is that there is no unstable manifold of $u \equiv 0$ to consider. Instead, one simply intersect a boundary manifold, for instance $\mathcal{B} = \{u \mid u + u_{xx} = u_x + u_{xxx} = 0 \text{ at } x = 0\}$, with the stable manifold of the periodic solutions.

**Slow Parameter Ramps**

Even with the above attention to the problem with boundary conditions, a rigorous discussion of the problem with a jump-type parameter inhomogeneity is absent from the literature. Instead, some authors have considered a parameter that varies slowly in space. The first such study appears in [43] which shows that at any finite order, a sufficiently slow spatial parameter ramp selects a unique wavenumber. Given a maximal value of the parameter ramp, the authors of [67] compute the selected wavenumber to leading order. This contrasts with our case, in which a narrow band of wavenumbers is selected. One consequence of this qualitative difference is that the selected wavenumber is zigzag stable, and thus a slow parameter ramp cannot be used to select zigzag patterns in the way that we use a jump-type inhomogeneity to do so in Section 2.6.3.

It would be interesting to understand in more detail the transition from slow parameter ramps to boundary conditions or the parameter inhomogeneity we consider here. One approach would be to interpolate between a slow-ramp and a jump-type parameter. One could consider spatially inhomogeneous parameter profiles $\mu(x) = h(x;\gamma)$ which converge (in some sense) to a jump-type parameter and an arbitrarily slow ramp for extremal values of $\gamma$. A simple such family is given by $h(x,\gamma) = \varepsilon^2 \tanh(\gamma x)$. We expect that for $\gamma$ sufficiently large, our analysis here can be adapted without much additional work, leaving leading-order coefficients unchanged. Roughly speaking, one appends an equation for the parameter evolution, $h' = (\gamma/\varepsilon^2)(\varepsilon^2 - h)(\varepsilon^2 + h)$. Then the flows we found for $x > 0$ and $x < 0$ now reside in normally hyperbolic asymptotic subspaces where $h = \pm\varepsilon^2$. The fast flow in the direction of $h$ is trivial in the direction of $u$. Thus contributions to the strain-displacement relation come only from normal form transformations, as in the present work. We expect changes in the asymptotics

when normal hyperbolicity breaks down, for $\gamma \sim \varepsilon$, such that dynamics in $h$ cannot be thought of as instantaneous anymore and normal-form coordinate changes evolve in $h$ nontrivially. In the limit when $\gamma$ is very small, normal form changes can be performed adiabatically in $h$ and we recover the results on slow ramps.

### Stability

Linearizing at the striped front solutions constructed here, one expects to find continuous spectrum up to the origin. As argued in [58], an eigenvalue emerges from the edge of the essential spectrum when following solutions along the strain-displacement relation through an extremum of $k_x$. As a consequence, the slope, $k_x'(\phi)$ gives a parity index for stability. Generally, one might expect that decreasing $k_x$, that is, stretching the asymptotic pattern, would be associated with "pulling" on the pattern, that is, displacing the pattern to the right or increasing $\phi$. With this intuition, $k_x'(\phi) < 0$ would correspond to stable stationary fronts and $k_x'(\phi) > 0$ to "unphysical" unstable stationary fronts; see the discussion in [58, §2.4] and the numerical evidence in [25]. The present situation might be a good starting point to understand how this mechanistic intuition may relate to a spectral analysis of the linearization.

### Patterns in the Plane: Two Dimensions

In two space dimensions $(x, y) \in \mathbb{R}^2$, with parameter $\mu(x)$ with a one-dimensional inhomogeneity $\{x = 0\}$, stripes near $x = -\infty$ can possess arbitrary orientations $u_{\mathrm{str}}(k_x x + k_y y; \mathbf{k})$, with $\mathbf{k}^2 = k_x^2 + k_y^2$. In particular, one can now ask for solutions asymptotic to stripes that are perpendicular to the parameter jump, with $k_x = 0$, or at an oblique angle to the parameter jump. In the much simpler Allen-Cahn equation, and to some extent in the slightly more complicated Cahn-Hilliard equation, such solutions have been constructed in [55, 57, 56], showing in particular that stripes are either parallel or perpendicular to the parameter jump in this case. In the case of the Swift-Hohenberg equation, [28] has employed an approach using an infinite-dimensional center-manifold and normal form analysis following [32, 33, 71], which study grain boundaries. Numerical results in this scenario are forthcoming in [7].

Yet more intricate phenomena are to be expected when considering hexagonal patterns rather than stripes, as we will do in the next chapter.

# Chapter 3

# Hexagonal Fronts

## 3.1 Introduction

We exhibit a wavenumber selection mechanism for periodic patterns arranged on a hexagonal lattice. The selection stems from an inhomogeneity in the external environment. This inhomogeneity yields the background state stable in the right-half of the domain and unstable in the left half. The result is a domain half-covered by hexagonal patterns, see 4.9. Without the inhomogeneity, these hexagons typically appear with horizontal wavenumber in a characteristic interval. We find that the width of this interval is significantly restricted and that the wavenumber selected from this interval can be determined as a function of the horizontal phase shift of the periodic hexagons.

Just as in Chapter 2, we examine this pattern selection in the 2-dimensional Swift-Hohenberg equation where the linear term is adorned with a spatially inhomogeneous parameter $\mu = \mu(x) = -\operatorname{sgn}(x)\varepsilon^2$, for small $\varepsilon > 0$. In order to obtain the hexagonal patterns we also include a quadratic term, which breaks the odd symmetry possessed by the version of Chapter 2. For small $\nu > 0$, we investigate the equation

$$\frac{\partial u}{\partial t} = -\left(1+\Delta\right)^2 u + \mu(x)u + \nu u^2 - u^3, \qquad u \in \mathbb{R}, \qquad (x,y) \in \mathbb{R}^2. \tag{1.4}$$

We are interested in small, steady-state, spatially-periodic solutions that are even with

respect to their maxima

$$\mathbf{P}_{\text{hex}} := \{u_{\text{hex}}(k_x x - \phi, k_y y; k_x) \mid \phi \in [0, 2\pi)\}\,.$$

As discussed in the introduction, these solutions can be parameterized by their horizontal phase $\phi$ and their wavevector $\mathbf{k} = (k_x, k_y)$ satisfying $|\mathbf{k}^2 - 1| < \sqrt{\mu}$ on a hexagonal lattice. Bifurcations on such a hexagonal lattice have been studied in depth by [9], with an excellent overview provided by [37]. These sources derive amplitude equations which can be associated to the ODEs appearing in Section 3.2.

Solutions to the Swift-Hohenberg equation with spatially homogeneous parameter (1.2) have been studied in [9, 13, 52, 64] and shown to have the leading order form

$$u(x, y, t) = u(x, y) \sim \varepsilon \left( c_0 e^{\mathrm{i}\mathbf{k}_0 \cdot (x,y)} + c_+ e^{\mathrm{i}\mathbf{k}_+ \cdot (x,y)} + c_- e^{\mathrm{i}\mathbf{k}_- \cdot (x,y)} + c.c. \right), \quad c_\kappa \in \mathbb{C}$$

with wavevectors $\mathbf{k}_\kappa$ for $\kappa \in \{0, +, -\}$.

A hexagonal lattice has wavevectors at angles of $2\pi/3$ to each other. Therefore $\mathbf{k}_0 + \mathbf{k}_+ + \mathbf{k}_- = 0$. There are only two distinct choices for these wavevectors, up to planar symmetries, and we focus on the choice that positions the "seam" between hexagons vertically, see Figure 3.1. This choice ensures that the line $\{x = 0\}$, where the linear parameter jumps from $-\varepsilon^2$ to $\varepsilon^2$, is parallel to the seam between vertical lines of hexagons. Thus we set

$$\begin{aligned} \mathbf{k}_0 &= (-1, 0) \\ \mathbf{k}_+ &= (1/2, \sqrt{3}/2) \\ \mathbf{k}_- &= (1/2, -\sqrt{3}/2). \end{aligned}$$

We seek fronts connecting these hexagonal solutions, across the parameter inhomogeneity, to the trivial state. Our investigation includes

- a rigorous derivation of amplitude equations which describe dynamics on both sides of the jump simultaneously
- numerical evidence for the existence of *hexagonal fronts*, and for persistence
- a conceptual framework for computing strain-displacements relation for hexagonal

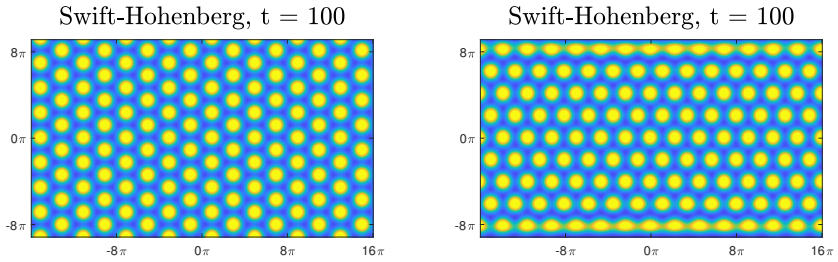


Figure 3.1: Patterns on two orientations of the hexagonal lattice. The one defined by wavevectors $\mathbf{k}_\kappa$ described in text has columns of maxima (left) while the other has rows of maxima (right).

fronts

- implementation of this framework to numerically compute numerical strain-displacement relations

Our main theorem of the chapters requires some explanatory remarks.

**Theorem 3.1.** *Assume Hypotheses 1 and 2. Then for sufficiently small $\varepsilon > 0$ and $\nu > 0$, there exists a one-parameter family stationary hexagonal fronts $u_*(x, y)$ solving the Swift-Hohenberg equation with spatial inhomogeneity* (1.4)*. The family $u_*(x, y; \phi) = u_*(x; \phi + 2\pi)$ is periodic in the parameter $\phi$. Each $u_*$ is asymptotic to a hexagonal pattern $u_{\text{hex}} \in \mathbf{P}_{\text{hex}}$ whose phase $\phi$ determines its wavenumber $k_x$ according to a strain-displacement relation*

$$k_x(\phi; \nu, \varepsilon) = \frac{1}{2} + \frac{\varepsilon k(\phi; \nu, \varepsilon)}{2} + \mathcal{O}(\varepsilon^3),$$

*where $k(\phi; \nu, \varepsilon)$ is given by the formula of Corollary 3.11.*

*Remark* 3.1. The hypotheses above merit some explanation, since we cannot yet state them in full.

- Hypothesis 1 assumes the existence of a heteroclinic in a simplified set of real amplitude equations describing the dynamics. We state it fully at the end of Section 3.2.3. We provide numerical evidence in Section 4.1.2.
- Hypothesis 2 assumes that the intersection defining the strain-displacement relation is transverse. It is stated in context in Section 3.4.3. We provide numerical evidence in Sections 4.1.3 and 4.1.5.

The formula in Corollary 3.11 comes from a Melnikov-type computation in Section 3.5.2. It gives $k$ in terms of $\phi, \nu, \varepsilon$, and an integral over the heteroclinic solution that is not obtainable in an explicit form. Therefore, while we have an "explicit" formula, it cannot be readily employed – even at first order. Instead, we numerically compute $k(\phi; \nu, \varepsilon)$ in Section 4.1.5.[1] Based on our computations, a best guess with $\nu = \varepsilon$ would be $k(\phi; \varepsilon, \varepsilon) \approx \frac{\varepsilon}{8}\cos(\phi)$. With this guess, we would have

$$k_x(\phi; \nu, \varepsilon) = \frac{1}{2} + \frac{\varepsilon^2}{16} + \mathcal{O}(\varepsilon^3),$$

in agreement with the case of striped fronts in Chapter 2.

Other studies of similar *hexagonal fronts* include [17] and [48]. In the former, the authors study propagating hexagonal fronts where the trivial state, due to instability, is invaded by the hexagonal pattern. Additionally, they classify other propagating fronts involving hexagons, rolls, and the trivial state. They prove existence and use numerical continuation to find the speed of propagation as a function of the linear parameter $\mu$. Our methods of spatial dynamics and center manifold reduction are directly inspired by this work. We differ from these authors in that we study stationary fronts, which are made possible in large part by our inhomogeneous parameter $\mu(x)$.

Stationary hexagonal fronts, and other spatially localized patterns, are the subject of [48]. The authors focus on a parameter regime of bistability, where both the hexagonal pattern and the trivial state is stable. This occurs for values of $\mu < 0$, and consequently results from [48] may be applied on the right half of our domain. The main results are a comprehensive bifurcation analysis of complex snaking behavior. This snaking behavior leads to an array of spatially localized patches of varying shape and size. In their analysis they find a spatially-conserved quantity for the 2D SH equation and use it to arrive at a selection mechanism for the wavenumber of hexagonal patterns. This is quite similar to our 1D argument in Chapter 2 and their conserved quantity may provide an alternative path to explicit computation of the strain-displacement curve.

Finally, the work of [33] also studies stationary fronts in the 2D SH equation. These fronts represent a phenomenon known as a *grain boundary* where two areas of stripes that are not parallel meet to create a defect. This work proves an existence result

[1] If the reader flips to this section now, note that $\nu = \varepsilon\delta$.

for grain boundaries that includes a selection mechanism whereby the wavenumber is determined by the angle between the stripes in the two patches. Their approach computes amplitude equation by using spatial dynamics, center manifold reduction, and normal form theory. Our normal form computations in Section 3.4 closely follow the approach of [33], going beyond that work to compute the normal form for quadratic and the actual transformation for the linear terms.

**Outline** The remainder of the chapter is organized as follows. The next section introduces the amplitude equations and discusses the equilibria, periodic solutions, and invariant manifolds which are the major players in constructing a heteroclinic orbit across the parameter jump. In Section 3.3, we begin deriving the amplitude equations from SH equation through a procedure similar to [17]. We end that section with a finite-dimensional ODE for the dynamics of the reduced vector field using variables in the center subspace. Section 3.4 computes the normal form equation and, through meticulous analysis, the transformations that must be applied to arrive there. We follow the method of computation in [33] and use the power of the theory contained in [30]. The end of this section includes an overview of all the changes of coordinates to navigate from the SH equation to the amplitude equations, summarized in Figure 3.2. Here we also by use the linear normal form transformation to compute the key bridge transformation, which crosses the parameter jump. In Section 3.5, we outline a conceptual framework for the numerics of Section 4.1. This framework explains how the numerics justify our hypotheses and results. Additionally, it outlines a path forward for analytically computing the strain-displacement relation (and hence the selected wavenumber). We leave our discussion of some consequences of our results and other questions until after we present numerics in the next chapter, in Section 4.3.

## 3.2 Amplitude Equations for Hexagons

We establish existence of hexagonal patterns as steady-state solutions to SH equation by using amplitude equations which approximate the behavior of the Swift-Hohenberg equation at the onset of the pattern forming instability. We relate these solutions to equilibria of these ODEs. Employing spatial dynamics, we relate spatial transitions

between patterned states in Swift-Hohenberg to heteroclinic connections in the amplitude equations. We aim to construct these heteroclinic connections by gluing pieces of solutions from a pair of equations, left and right. This leading-order approximation is made rigorous in Sections 3.3-3.4.2 and the intersection is demonstrated (numerically) to exist and be transverse in Section 4.1 of the next chapter.

This section describes the relevant equilibria, periodic orbits, and invariant manifolds. We conduct a brief count of the dimensions of unstable and stable manifolds. This serves as a heuristic suggesting that, generically, we should expect a 1-dimensional transverse intersection. We end the section with a precise statement of an existence hypothesis, which is supported by numerics.

To compute the following amplitude equations for solutions on a hexagonal lattice in the Swift-Hohenberg equation with $\mu(x) = -\operatorname{sgn}(x)\varepsilon^2 > 0$ we use spatial dynamics, the center manifold theorem, and normal form theory in the procedure described in Sections 3.3-3.4. The resulting equations (3.57) are then truncated to include only terms of order $\mathcal{O}(1)$ in the parameter $\varepsilon$. We then have ODEs in $\mathbb{C}^6$

$$\begin{aligned}
c_0' &= d_0 \\
d_0' &= \tfrac{1}{4}\left(\operatorname{sgn}(x)c_0 - \delta 2\overline{c_+c_-} + 3c_0(|c_0|^2 + 2|c_+|^2 + 2|c_-|^2)\right) \\
c_+' &= d_+ \\
d_+' &= \operatorname{sgn}(x)c_+ - \delta 2\overline{c_0c_-} + 3c_+(2|c_0|^2 + |c_+|^2 + 2|c_-|^2) \\
c_-' &= d_- \\
d_-' &= \operatorname{sgn}(x)c_- - \delta 2\overline{c_0c_+} + 3c_-(2|c_0|^2 + 2|c_+|^2 + |c_-|^2).
\end{aligned} \tag{3.1}$$

In (3.1), the derivative corresponds to a spatial derivative in the $x$ direction in the Swift-Hohenberg equation. The variable $c_0$ corresponds to the amplitude of a spatially periodic pattern in Swift-Hohenberg with wave-vector $\mathbf{k} = (-1, 0)$. The variables $c_\pm$ correspond to the amplitudes of spatially periodic patterns in Swift-Hohenberg with wave-vector $\mathbf{k} = (\frac{1}{2}, \pm\frac{\sqrt{3}}{2})$.

The general amplitude equations for steady bifurcations on a hexagonal lattice can be found in [37, §5.4]. Our ODEs may be most closely related to the steady-states of a PDE describing the evolution of instabilities of the hexagonal patters in [37, §9.1].

*Remark* 3.2. Naively, one might justify the truncation of $\mathcal{O}(\varepsilon)$-terms through usual

ODE theory for continuity in parameters. As shown in Section 3.4.2, this simplification would brush over two details.

First, there is a technical consideration that some of the truncated terms have a factor of $e^{ix/\varepsilon}$, which can have a significant effect on the dynamics as $\varepsilon \to 0$. To deal with these, one considers them as a "rapidly rotating" perturbation and uses results from [39]

Second, and more importantly, we must take into account additional $\mathcal{O}(\varepsilon)$ terms once we want to take $\varepsilon > 0$. These terms come from the "commutator" of the normal form transformation involved in translating between the different phase spaces obtained by the inhomogeneous transformations on each halves of the domain $x < 0$ and $x > 0$. These terms are essential for computing the effect of the inhomogeneous parameter $\mu(x)$ on the wavenumber of the selected hexagons.

**Hexagons** For equilibria with $c_0 = c_+ = c_-$, the superposition of these three patterns corresponds to perfectly symmetric planar hexagonal patterns. Near these equilibria, we seek periodic orbits with wavenumber $k$ and amplitude $|c_0| \approx |c_+| = |c_-|$. These correspond to small modulations of the spatially periodic patterns in Swift-Hohenberg with wave-vectors $\mathbf{k}_0 \approx (-1 + \varepsilon k, 0)$ and $\mathbf{k}_\pm \approx (\frac{1+\varepsilon k}{2}, \pm\frac{\sqrt{3}}{2})$, as can be computed by carefully undoing the transformations of the following section.

Before proceeding, we make use of an important simplification. Note that the last two equations are redundant under the assumption $c_+ = c_-$, which is true for the equilibria we seek. Thus the subspace $\{c_+ = c_-\}$ is invariant and we may restrict our attention to this subspace. For the remainder of this section, we consider the ODEs in variable $\mathbf{c} = (c_0, d_0, c_+, d_+) \in \mathbb{C}^4$

$$\begin{aligned} c_0' &= d_0 \\ d_0' &= \tfrac{1}{4}\left(\operatorname{sgn}(x)c_0 - \delta 2\overline{c_+}^2 + 3c_0(|c_0|^2 + 4|c_+|^2)\right) \\ c_+' &= d_+ \\ d_+' &= \operatorname{sgn}(x)c_+ - \delta 2\overline{c_0 c_+} + 3c_+(2|c_0|^2 + 3|c_+|^2) \end{aligned} \tag{3.2}$$

*Remark* 3.3. This restriction to the $\{c_+ = c_-\}$ subspace corresponds to restricting to hexagonal patterns that are even in $y$. These are precisely the patterns captured by the

normal form procedure executed in the next section and thus this restriction holds even for higher order terms than the ones appearing in the present amplitude equations.

Finally, note that these equations are invariant under a complex rotation $\mathbf{c} \to \mathcal{R}_\theta \mathbf{c}$ for each choice of $x < 0$ and $x > 0$. We denote the complex rotation by

$$\mathcal{R}_\theta \mathbf{c} := e^{\mathrm{i}\theta R}\mathbf{c} \tag{3.3}$$

$$= \begin{bmatrix} e^{-\mathrm{i}\theta} & 0 & 0 & 0 \\ 0 & e^{-\mathrm{i}\theta} & 0 & 0 \\ 0 & 0 & e^{\frac{\mathrm{i}}{2}\theta} & 0 \\ 0 & 0 & 0 & e^{\frac{\mathrm{i}}{2}\theta} \end{bmatrix} \begin{bmatrix} c_0 \\ d_0 \\ c_+ \\ d_+ \end{bmatrix}. \tag{3.4}$$

Now we describe the equilibria, periodic orbits, and relevant invariant manifolds for the dynamics of this ODE for each of $x < 0$ and $x > 0$.

### 3.2.1 Dynamics for $x > 0$

Fixing $x > 0$, we have the ODEs

$$\begin{aligned} c_0' &= d_0 \\ d_0' &= \tfrac{1}{4}\left(c_0 - \delta 2\overline{c_+}^2 + 3c_0(|c_0|^2 + 4|c_+|^2)\right) \\ c_+' &= d_+ \\ d_+' &= c_+ - \delta 2\overline{c_0 c_+} + 3c_+(2|c_0|^2 + 3|c_+|^2). \end{aligned} \tag{3.5}$$

**Lemma 3.2.** *In equation* (3.5) *the trivial equilibrium* $\mathbf{c_0} := \{c_0 = c_+ \equiv 0\}$ *is hyperbolic with a 4-dimensional stable manifold* $\mathcal{W}^s$*, for all values of* $\delta > 0$.

*Proof.* We begin by inspecting the real subspace $\{c_0, c_+ \in \mathbb{R}\} \cong \mathbb{R}^4$. Due to the rotational symmetry, results in the real subspace have relevant consequences in the full phase space. Additionally, it is convenient for developing intuition and we can visualize it in the $c_0, c_+$-plane.

**Real Subspace.** Since there are no complex coefficients, the real subspace $\{c_0, c_+ \in \mathbb{R}\} \cong \mathbb{R}^4$ is invariant and we first restrict our attention here. Solving for equilibria, we

algebraically find three, so long as $\delta > \sqrt{15}$,

$$\begin{aligned} \mathbf{c}_0 &= \{c_0 = c_+ = 0\} \\ \mathbf{c}_{\text{dnhex}} &= \left\{ c_0 = c_+ = \tfrac{\delta}{15}(1 - \sqrt{1 - \tfrac{15}{\delta^2}}) \right\} \\ \mathbf{c}_{\text{hex}} &= \left\{ c_0 = c_+ = \tfrac{\delta}{15}(1 + \sqrt{1 - \tfrac{15}{\delta^2}}) \right\}. \end{aligned} \tag{3.6}$$

The equilibrium $\mathbf{c}_{\text{dnhex}}$ corresponds to a solution that is unstable in the PDE. The equilibrium $\mathbf{c}_{\text{hex}}$ corresponds to hexagonal patterns, which are not our focus in the $x > 0$ dynamics.

We compute the linearization of (3.5) about the trivial equilibrium $\mathbf{c}_0$ and find that $\mathbf{c}_0$ is hyperbolic with a 2-dimensional real stable manifold $\mathcal{W}^{s,\mathbb{R}}$.

**Full Phase Space.** After a longer, but still straightforward computation, one finds that the trivial equilibrium $\mathbf{c}_0$ is still hyperbolic in the full, complex phase space $\cong \mathbb{C}^4$. The complex stable manifold $\mathcal{W}^s$ is 4-dimensional.

□

### 3.2.2 Dynamics for $x < 0$

Now we consider $x > 0$, we have the ODEs

$$\begin{aligned} c_0' &= d_0 \\ d_0' &= \tfrac{1}{4}\left(-c_0 - \delta 2\overline{c_+}^2 + 3c_0(|c_0|^2 + 4|c_+|^2)\right) \\ c_+' &= d_+ \\ d_+' &= -c_+ - \delta 2\overline{c_0 c_+} + 3c_+(2|c_0|^2 + 3|c_+|^2). \end{aligned} \tag{3.7}$$

**Lemma 3.3.** *Equation* (3.7) *possesses a 2-dimensional family of periodic orbits parameterized by a wavenumber $k$ and a phase $\theta$. For $\delta > \frac{\sqrt{3}}{4}$, there is a subfamily $\mathcal{P}$ that is a normally hyperbolic manifold with a 5-dimensional unstable foliation $\mathcal{W}^{cu}_{\mathcal{P}}$.*

*Proof.* **Real Subspace.** Again, we begin by examining the real subspace $\{c_0, c_+ \in$

$\mathbb{R}\} \cong \mathbb{R}^4$, which is invariant. We can algebraically compute three real equilibria:

$$\begin{aligned}
\mathbf{c}_{\text{rect}} &= \left\{ c_0 = \delta\tfrac{2}{3}, c_+ = \tfrac{\delta}{3}\sqrt{\tfrac{1}{\delta^2} - \tfrac{4}{3}} \right\} \\
\mathbf{c}_{\text{dnhex}} &= \left\{ c_0 = c_+ = \tfrac{\delta}{15}(1 - \sqrt{1 + \tfrac{15}{\delta^2}}) \right\} \\
\mathbf{c}_{\text{hex}} &= \left\{ c_0 = c_+ = \tfrac{\delta}{15}(1 + \sqrt{1 + \tfrac{15}{\delta^2}}) \right\}
\end{aligned} \tag{3.8}$$

The first equilibrium $\mathbf{c}_{\text{rect}}$ corresponds to a rectangular pattern in the Swift-Hohenberg equation, arranged on the hexagonal lattice. The second two correspond to hexagonal patterns in the Swift-Hohenberg equation with differing phases. The second equilibrium, $\mathbf{c}_{\text{hex}}$ corresponds to "up hexagons", where the interior of each hexagon has a positive value of the SH equation variable and the space on the lattice has a negative value. The last equilibrium, $\mathbf{c}_{\text{dnhex}}$ corresponds to "down hexagons", where these values are reversed. It turns out that down hexagons are unstable in the full PDE and so we focus on the equilibrium $\mathbf{c}_{\text{hex}}$.

By computing the linearization in the real subspace, we conclude that for $\delta > \frac{\sqrt{3}}{4}$, the last equilibrium $\mathbf{c}_{\text{hex}}$ is hyperbolic with a 2-dimensional real unstable manifold $\mathcal{W}^{u,\mathbb{R}}_{\mathbf{c}_{\text{hex}}}$.

**Full Phase Space.** Due to rotational symmetry under $\mathcal{R}_\theta$, there is a circle of equilibria $\{\mathcal{R}_\theta \mathbf{c}_{\text{hex}} \mid \theta \in [0, 2\pi)\}$. A somewhat lengthy computations confirms that each of these possesses its own 3-dimensional unstable manifold. Thus the circle has a 4-dimensional unstable foliation $\mathcal{W}^u_{\mathcal{R}_\theta \mathbf{c}_{\text{hex}}}$.

Next we move to a co-rotating reference frame in search of periodic orbits nearby this circle of equilibria. We apply the change of coordinates $\mathbf{c} \to \mathcal{R}_{kx}\mathbf{c}$. Now periodic orbits with wavenumber $k$ in (3.7) correspond to equilibria in the resulting family of equations parameterized by $k$,

$$\begin{aligned}
c_0' &= \mathrm{i}kc_0 + d_0 \\
d_0' &= \mathrm{i}kd_0 + \tfrac{1}{4}\left(-c_0 - \delta 2\overline{c_+ c_-} + 3c_0(|c_0|^2 + 2|c_+|^2 + 2|c_-|^2)\right) \\
c_+' &= -\tfrac{\mathrm{i}k}{2}c_+ + d_+ \\
d_+' &= -\tfrac{\mathrm{i}k}{2}d_+ - c_+ - \delta 2\overline{c_0 c_-} + 3c_+(2|c_0|^2 + |c_+|^2 + 2|c_-|^2)
\end{aligned} \tag{3.9}$$

For each value of $k \in (-2, 2)$ we can algebraically find such an equilibrium.

Seeing this is another algebraic exercise, which we carry out explicitly here because it shows how one computes the magnitude of the corresponding periodic orbit at leading order in $k$. Combining the first and second equation in (3.9) we arrive at

$$-k^2 c_0 = \tfrac{1}{4}(-c_0 - 2\delta c_+^2 + 3c_0(c_0^2 + 4c_+^2)) \implies c_+^2 = \frac{c_0(1-4k^2) - 3c_0^3}{12c_0 - 2\delta}$$

Combining the third and fourth equations, and plugging in this expression for $c_+^2$, we have

$$\frac{-k^2}{4} = -1 - 2\delta c_0 + 3\left(2c_0^2 + 3\left(\frac{c_0(1-4k^2) - 3c_0^3}{12c_0 - 2\delta}\right)\right),$$

which can be solved for three real roots as functions of $k, \delta$. For values of $\delta > 0$, the discriminant of the associated cubic polynomial in $c_0$ is greater than zero – guaranteeing existence of three roots. Each root corresponds to a real equilibrium of (3.9). In particular, we note that the third root yields an equilibrium $\mathbf{c}_{\text{hex}}(k)$ that converges to $\mathbf{c}_{\text{hex}}$ as $k \to 0$.

Linearizing, we see that this equilibrium possesses a 3-dimensional unstable manifold for any $k$ an interval $I$ around 0.

Undoing our change of coordinates, this equilibrium corresponds to a periodic orbit $\{\mathcal{R}_{kx}\mathbf{c}_{\text{hex}}(k)\}$ in equation (3.7). Again employing the rotational symmetry, we see that this periodic can have arbitrary phase by composing with a rotation $\mathcal{R}_\theta$. Thus, we've found a 2-dimensional family of periodic orbits parameterized by the wavenumber $k$ and a phase $\theta$ of its members,

$$\mathcal{P} = \{\mathcal{R}_{kx+\theta}\mathbf{c}_{\text{hex}}(k) \mid k \in I, \theta \in (0, 2\pi]\}$$

Note that the circle of equilibria $\{\mathcal{R}_\theta \mathbf{c}_{\text{hex}}\}$ of (3.7) is embedded in $\mathcal{P}$ by choosing $k = 0$.

For each choice of $k$ and $\theta$, recall that the corresponding periodic orbit $\mathcal{R}_{kx+\theta}\mathbf{c}_{\text{hex}}(k)$ has a 3-dimensional strong unstable fiber $W^{uu}(k, \theta)$. Thus the full family $\mathcal{P}$ has a 5-dimensional center unstable foliation

$$\mathcal{W}^{cu}_{\mathcal{P}} = \bigcup_{k,\theta} \mathcal{W}^{cu}_{\mathcal{R}_{kx+\theta}\mathbf{c}_{\text{hex}}(k)} = \left\{W^{uu}(k, \theta) \mid k \in J_k, \theta \in S^1\right\}$$

for some $J_k \subseteq (-2, 2)$. □

*Remark* 3.4. Computing the dimension of the center unstable foliation uses a co-rotating frame in order to indirectly compute Floquet exponents. We used a similar approach in Example 1.1 and in Section 2.2.2. The full, somewhat tedious, computation in the present higher-dimensional context is omitted.

### 3.2.3 An Apparent 1D Intersection

All this dimension counting of invariant manifolds leads us to a key observation. The sum of the dimension of the unstable foliation of periodic orbits $\mathcal{P}$ in (3.7) and the dimension of stable manifold of the trivial equilibrium $\mathbf{c_0}$ is $5 + 4 = 9$. The ambient phase space $\mathbb{C}^4$ is only 8-dimensional, and so we expect an intersection of dimension $9 - 8 = 1$. Technically, there are two ambient phase spaces; one for equations (3.7) and one for equations (3.5). The reader may imagine laying one over the other to visualize this intersection. This intersection turns out to be a circle, obtained by rotating the intersection in the real subspace.

**Hypothesis 1** (Existence for $\varepsilon = 0$)**.** *In the real subspace* $\{c_0, c_+ \in \mathbb{R}\} \cong \mathbb{R}^4$ *of the phase space for equations* (3.2)*, for any* $\delta > \sqrt{3}/4$*, the unstable manifold of* $\mathbf{c}_{hex}$ *intersects the stable manifold of* $\mathbf{c}_0$ *in a single point*

$$\mathcal{W}^{u,\mathbb{R}}_{\mathbf{c}_{hex}} \bigcap \mathcal{W}^{s,\mathbb{R}} = \{s\}.$$

*Thus there is exists a real heteroclinic orbit* $\mathbf{c}_{hex} \to \mathbf{c}_0$*.*

This claim is equivalent to an ODE boundary-value problem in $\mathbb{R}^4$. Due to a lack of monotonicity, basic methods such as invariant regions or sub-solutions are unavailable. We provide numerical evidence substantiating the hypothesis in Section 4.1.2. For the remainder we assume this existence in our argument.

**Proposition 3.4.** *Assume that Hypothesis 1 holds and that* $\delta > \sqrt{3}/4$*. In the full phase space* $\mathbb{C}^4$ *of equations* (3.2)*, the center unstable foliation of the periodic orbits* $\mathcal{P}$ *intersects the stable manifold of the trivial equilibrium* $\mathbf{c}_0$ *in a circle*

$$\mathcal{W}^{cu}_{\mathcal{P}} \bigcap \mathcal{W}^{s} = \mathcal{S}.$$

*The circle $\mathcal{S} = \{\mathcal{R}_\theta s\}$ is obtained by complex rotation of the real intersection point in the hypothesis.*

*It follows that there exists a 1-parameter family of heteroclinic orbits $\mathbf{c}_*(\theta)$ from the complex-rotated hexagons $\mathcal{R}_\theta \mathbf{c}_{hex} \to \mathbf{c}_0$ to the trivial equilibrium.*

*Proof.* Due to the invariance of equations (3.2) under the complex rotation $\mathcal{R}_\theta$ discussed in Section 3.2, we can rotate the objects in the real subspace provided by the hypothesis. This proves that the intersection includes the circle described above. Dimension counting rules out any additional part of the intersection. □

Section 4.1.3 documents numerical evidence for the circle of intersection.

*Remark* 3.5. This proposition implies that, for all $\theta$, the only heteroclinic connection is to an equilibrium and so $k = 0$. This leads to a vertical strain-displacement relation for the amplitude equations. We refer to such vertical relations as a *wavenumber selection* phenomenon, implying selection of a unique wavenumber. The forthcoming derivation of the amplitude equations adds in $\mathcal{O}(\varepsilon)$ terms. These terms perturb the vertical strain-displacement relation slightly, causing it to wiggle but remain roughly vertical. Thus the final result is dubbed *wavenumber restriction*, with a narrow interval of possible $k$.

Next, we rigorously derive the ODEs of this section from the full steady-state Swift-Hohenberg equation.

## 3.3 Spatial Dynamics and the Center Manifold

In the following three sections our aim is to describe all small, bounded solutions of the inhomogeneous Switft-Hohenberg equation (1.4) by a set of ODEs. Up to an order-$\varepsilon$ perturbation, these ODEs turn out to be the amplitude equations (3.1) from the previous section. We begin by formulating our PDE as a dynamical system in a Banach space and then reducing to a finite-dimensional problem via the center manifold theorem.

Recall that the hexagonal patterns we seek have a wave-vector $\mathbf{k} = (k_x, k_y)$ with vertical wavenumber $k_y = \frac{\sqrt{3}}{2}$. We rescale the variable $y \mapsto k_y y$ so that now we search for solutions with vertical period $2\pi$ in the new vertical variable. The equation becomes

$$0 = -\left(1 + k_y^2 \partial_y^2\right)^2 u - 2\left(1 + k_y^2 \partial_y^2\right) u_{xx} + \mu u + \nu u^2 - u^3. \tag{3.10}$$

We treat $x$ as the evolution variable and write this as a first order equation

$$\frac{dU}{\mathrm{d}x} = \mathcal{L}U + \mathcal{F}(U;\mu,\nu) \tag{3.11}$$

with $U$ the infinite dimensional phase space

$$\mathcal{X} := H^3_{\mathrm{per}}(0,2\pi) \times H^2_{\mathrm{per}}(0,2\pi) \times H^1_{\mathrm{per}}(0,2\pi) \times L^2(0,2\pi)$$
$$\text{where } H^j_{\mathrm{per}}(0,2\pi) = \{u \in H^j_{\mathrm{loc}}(\mathbb{R}) \mid u(z+2\pi) = u(z), \text{ for all } z \in \mathbb{R}\}.$$

In the equation above,

$$U = \begin{bmatrix} u \\ u_x \\ u_{xx} + (1+k_y^2\partial_y^2)u \\ u_{xxx} + (1+k_y^2\partial_y^2)u_x \end{bmatrix}, \qquad \mathcal{F}(U;\mu,\nu) = \begin{bmatrix} 0 \\ 0 \\ 0 \\ \mu u + \nu u^2 - u^3 \end{bmatrix},$$

$$\text{and} \qquad \mathcal{L} = \begin{bmatrix} 0 & 1 & 0 & 0 \\ -(1+k_y^2\partial_y^2) & 0 & 1 & 0 \\ 0 & 0 & 0 & 1 \\ 0 & 0 & -(1+k_y^2\partial_y^2) & 0 \end{bmatrix}.$$

This system represents an infinite dimensional dynamical system. Next we consider only dynamics of small bounded solutions. Such solutions compose the center manifold [30], which here is finite dimensional; we will arrive at an ODE in $\mathbb{C}^6$.

### 3.3.1 Center Manifold Reduction

To represent the dynamics on the center manifold, we compute the projection of equation (3.11) on the *center subspace*, a linear space spanned by the eigenfunctions of $\mathcal{L}$ corresponding to purely imaginary eigenvalues.

The spectrum $\operatorname{spec}\mathcal{L} = \{\pm\mathrm{i}, \pm\mathrm{i}\sqrt{1-k_y^2}\} = \{\pm\mathrm{i}, \pm\frac{\mathrm{i}}{2}\}$, with all eigenvalues algebraically double. The first $\pm\mathrm{i}$ are geometrically simple, while $\pm\frac{\mathrm{i}}{2}$ are geometrically double. These eigenvalues correspond to the $x$ component of the hexagonal symmetry lattice with our chosen orientation. We choose to use $\{-\mathrm{i}, \frac{\mathrm{i}}{2}\}$, and consider the other three as complex conjugates, with eigenfunctions $E_\kappa$ and generalized eigenfunctions $F_\kappa$,

for $\kappa \in \{0, +, -\}$, as follows

$$-\mathrm{i}: \quad E_0 = \begin{bmatrix} 1 \\ -\mathrm{i} \\ 0 \\ 0 \end{bmatrix}, \quad F_0 = \begin{bmatrix} 0 \\ 1 \\ -2\mathrm{i} \\ -2 \end{bmatrix}$$

$$\tfrac{\mathrm{i}}{2} = \mathrm{i}k_x: \quad E_\pm(y) = \begin{bmatrix} 1 \\ \mathrm{i}k_x \\ 0 \\ 0 \end{bmatrix} e^{\pm \mathrm{i}y}, \quad F_\pm(y) = \begin{bmatrix} 0 \\ 1 \\ 2\mathrm{i}k_x \\ -2k_x^2 \end{bmatrix} e^{\pm \mathrm{i}y}.$$

(Recall that $\mathcal{L}F_\kappa = \lambda_\kappa F_\kappa + E_\kappa$.)

We obtain a twelve-dimensional center subspace $\mathcal{X}_c$ with basis $\{E_\kappa, F_\kappa, \overline{E_\kappa}, \overline{F_\kappa} \mid \kappa = 0, \pm\}$. The spectral projection $\mathcal{P}_c : \mathcal{X} \to \mathcal{X}_c$ is given by

$$\mathcal{P}_c U = \sum_{\kappa \in \{0,\pm\}} \left( \langle U, E_\kappa^{\mathrm{ad}} \rangle E_\kappa + \langle U, F_\kappa^{\mathrm{ad}} \rangle F_\kappa + \langle U, \overline{E_\kappa^{\mathrm{ad}}} \rangle \overline{E_\kappa} + \langle U, \overline{F_\kappa^{\mathrm{ad}}} \rangle \overline{F_\kappa} \right),$$

where $\langle U\,, V \rangle = \sum_{j=1}^{4} \langle U_j, V_j \rangle_{L^2(0,2\pi)}$ denotes the scalar product on $(L^2(0, 2\pi))^4$. Using the adjoint operator

$$\mathcal{L}^{\mathrm{ad}} = \begin{bmatrix} 0 & -(1 + k_y^2 \partial_y^2) & 0 & 0 \\ 1 & 0 & 0 & 0 \\ 0 & 1 & 0 & -(1 + k_y^2 \partial_y^2) \\ 0 & 0 & 1 & 0 \end{bmatrix}$$

and definition of the adjoint vectors $E_\kappa^{\mathrm{ad}}, F_\kappa^{\mathrm{ad}}$ we may compute

$$E_0^{\mathrm{ad}} = \tfrac{1}{8\pi}\begin{bmatrix} 2 \\ -2\mathrm{i} \\ 0 \\ -\mathrm{i} \end{bmatrix}, \qquad F_0^{\mathrm{ad}} = \tfrac{1}{8\pi}\begin{bmatrix} 0 \\ 0 \\ -\mathrm{i} \\ -1 \end{bmatrix}$$

$$\text{and} \quad E_\pm^{\mathrm{ad}}(y) = \tfrac{1}{8\pi}\begin{bmatrix} 2 \\ 2\mathrm{i}/k_x \\ 0 \\ \mathrm{i}/k_x^3 \end{bmatrix} e^{\pm \mathrm{i}y}, \quad F_\pm^{\mathrm{ad}}(y) = \tfrac{1}{8\pi}\begin{bmatrix} 0 \\ 0 \\ \mathrm{i}/k_x \\ -1/k_x^2 \end{bmatrix} e^{\pm \mathrm{i}y}.$$

After an argument for the existence of a spectral gap and the boundedness of the resolvent operator[2], we can apply the center manifold theorem (see, for instance [30, §2.2]). We state the outcome below, after a brief remark to clarify our use of the symbol $\mu$.

*Remark* 3.6. Formally, we must apply the theorem twice, once for $x > 0$ and $\mu(x) \equiv -\varepsilon^2 < 0$ and again for $x < 0$ and $\mu(x) \equiv \varepsilon^2 > 0$. This yields two center manifolds, which can be compared by projecting one along the foliation of the other. This projection is trivial, for terms we are interested in studying here, so practically speaking this is not a technical obstacle. For the sake of brevity, we state the results all at once using the notation $\mu = -\operatorname{sgn}(x)\varepsilon^2$ and trust that the reader understands this is truly two statements.

**On the Center Manifold**

There exist three neighborhoods of the origin $\mathcal{U}_c \subset \mathcal{X}_c, \mathcal{U} \subset (\mathrm{Id} - \mathcal{P}_c)\mathrm{dom}\mathcal{L}, \mathcal{M} \subset \mathbb{R}^2$ and a map $\Psi \colon \mathcal{U}_c \times \mathcal{M} \to \mathrm{dom}\mathcal{L}$ of class $C^n$, for arbitrary but fixed $n \geq 1$. For any $(\mu, \nu) \in \mathcal{M}$, the bounded solutions of (3.11) with $U(x) \in \mathcal{U}_c \times \mathcal{U}$ for $x \in \mathbb{R}^+$ are contained in the center manifold given by the graph of $\Psi(\cdot; \mu, \nu)$. Thus they may be written

$$U(x) = U_c(x) + \Psi(U_c; \mu, \nu), \qquad \text{for } U_c \in \mathcal{U}_c. \tag{3.12}$$

[2]We omit these since they could be repeated from [33, §2]

Additionally, the center manifold is tangent to the center subspace in that

$$\|\Psi(U_c;\mu,\nu)\|_{\mathrm{dom}\mathcal{L}} = \mathcal{O}\left((\mu+\nu)\|U_c\| + \|U_c\|^2\right).$$

Plugging (3.12) into (3.11) and projecting with $\mathcal{P}_c$ we have a reduced equation for $U_c \in \mathcal{X}_c$, the center subspace,

$$\frac{dU_c}{\mathrm{d}x} = \mathcal{L}U_c + \mathcal{P}_c\mathcal{F}(U_c + \Psi(U_c;\mu,\nu);\mu,\nu) \tag{3.13}$$

which governs dynamics on the center manifold. Expanding the nonlinearity $\mathcal{F}$ and using the estimate on $\Psi$, we have

$$\begin{aligned}\frac{dU_c}{\mathrm{d}x} &= \mathcal{L}U_c + \mathcal{P}_c\mathcal{F}(U_c;\mu,\nu)\\ &+ \mathcal{O}\left(\mu^2\|U_c\| + \mu\nu\|U_c\| + \mu\|U_c\|^2 + \nu^2\|U_c\|^2 + \nu\|U_c\|^3 + \|U_c\|^4\right).\end{aligned}$$

Next we use the basis of $\mathcal{X}_c$ to write

$$U_c(x) = \sum_{\kappa\in\{0,+,-\}} \left(A_\kappa(x)E_\kappa + B_\kappa(x)F_\kappa + \overline{A_\kappa}(x)\overline{E_\kappa} + \overline{B_\kappa}(x)\overline{F_\kappa}\right),$$

and we will compute the terms of the reduced system to leading order

$$\frac{dU_c}{\mathrm{d}x} = \mathcal{L}U_c + \mathcal{P}_c\mathcal{F}(U_c;\mu,\nu). \tag{3.14}$$

In the basis for $\mathcal{X}_c$ described above, we compute the leading-order Taylor expansion up to order three of the reduced vector field.

$$\begin{aligned}
A_0' &= -\mathrm{i}A_0 + B_0 + \tfrac{\mathrm{i}}{4}\left(\mu a_0 + \nu(a_0^2 + 2a_+\overline{a_+}) - (a_0^3 + 6a_0a_+\overline{a_+})\right)\\
B_0' &= -\mathrm{i}B_0 - \tfrac{1}{4}\left(\mu a_0 + \nu(a_0^2 + 2a_+\overline{a_+}) - (a_0^3 + 6a_0a_+\overline{a_+})\right)\\
A_+' &= \tfrac{\mathrm{i}}{2}A_+ + B_+ - 2\mathrm{i}\left(\mu a_+ + \nu(2a_0a_+) - 3(a_0^2a_+ + a_+^2\overline{a_+})\right)\\
B_+' &= \tfrac{\mathrm{i}}{2}B_+ - \left(\mu a_+ + \nu(2a_0a_+) - 3(a_0^2a_+ + a_+^2\overline{a_+})\right)\\
A_-' &= \tfrac{\mathrm{i}}{2}A_- + B_- - 2\mathrm{i}\left(\mu\overline{a_+} + \nu(2a_0\overline{a_+}) - 3(a_0^2\overline{a_+} + a_+^2\overline{a_+})\right)\\
B_-' &= \tfrac{\mathrm{i}}{2}B_- - \left(\mu\overline{a_+} + \nu(2a_0\overline{a_+}) - 3(a_0^2\overline{a_+} + a_+^2\overline{a_+})\right)
\end{aligned} \tag{3.15}$$

and complex conjugate equations, where $'$ denotes the derivative with respect to $x$ and

$$a_0 = A_0 + \overline{A_0} \qquad \text{and} \qquad a_+ = A_+ + \overline{A_-}.$$

Note also that we have now fixed $k_x = 1/2$.

## 3.4 Normal Form Theorems and Transformations

Next we apply a series of coordinate changes that simplify (3.15), putting it into a normal form that matches the amplitude equations of Section 3.2. We first apply three transformations, in the form of homogeneous polynomials, that fit into the larger theory of normal forms. The full power of the theory in [30] provides existence of a normal form equation of arbitrarily high order in the variables $A_\kappa, B_\kappa$ and in parameters $\mu, \nu$. The proof of this existence is constructive, involving the iterative computation of the normal form at each order. Along the way, one may also compute the actual coordinate changes necessary to obtain the new equations.

Practically speaking, our goals only require the first three leading-order transformations:

- $\Phi_{1,1,0}$ which is $A_\kappa, B_\kappa$-linear and $\mu$-dependent;
- $\Phi_{2,0,1}$ which is $A_\kappa, B_\kappa$-quadratic and $\nu$-dependent;
- $\Phi_{3,0,0}$ which is $A_\kappa, B_\kappa$-cubic and $\mu, \nu$-independent.

Applying these transformations to equations (3.15), we will arrive at the normal form equations:

$$\begin{aligned}
C_0' &= -\mathrm{i}C_0 + D_0 \\
D_0' &= -\mathrm{i}D_0 + \tfrac{1}{4}\left(P_0(\mathbf{C}) - \mathrm{i}Q_0(\mathbf{C},\mathbf{D})\right) \\
C_+' &= \tfrac{\mathrm{i}}{2}C_+ + D_+ \\
D_+' &= \tfrac{\mathrm{i}}{2}D_+ + \left(P_+(\mathbf{C}) + 2\mathrm{i}Q_+(\mathbf{C},\mathbf{D})\right) \\
C_-' &= \tfrac{\mathrm{i}}{2}C_- + D_- \\
D_-' &= \tfrac{\mathrm{i}}{2}D_- + \left(P_-(\mathbf{C}) + 2\mathrm{i}Q_-(\mathbf{C},\mathbf{D})\right)
\end{aligned} + \mathbf{G}(\mathbf{C},\mathbf{D},\mu,\nu), \tag{3.16}$$

where $\mathbf{C} = (C_0, C_+, C_-)$ and similarly for $\mathbf{D}$. Here the polynomials representing the *terms in normal form* are given by

$$\begin{aligned} P_{\kappa=0}(\mathbf{C}) &= \operatorname{sgn}(x)\varepsilon^2 C_0 - \nu 2\overline{C_+ C_-} + 3C_0(|C_0|^2 + 2|C_+|^2 + 2|C_-|^2) \\ Q_{\kappa=0}(\mathbf{C},\mathbf{D}) &= \operatorname{sgn}(x)\varepsilon^2 D_0 - \nu 2(\overline{C_+ D_-} + \overline{C_- D_+}) \\ &\quad + 3C_0\left(C_0\overline{D_0} + \overline{C_0}D_0 + 2(\overline{C_+}D_+ + C_+\overline{D_+}) + 2(\overline{C_-}D_- + C_-\overline{D_-})\right) \\ &\quad + 3D_0(|C_0|^2 + 2|C_+|^2 + 2|C_-|^2) \end{aligned}$$

and with $P_\pm, Q_\pm$ obtained by permuting indices $\kappa \in \{0, +, -\}$ in the inputs. It's important to note that these polynomials are invariant under the complex rotation $\mathcal{R}_\theta$ on $\mathbb{C}^6$, originally from Section 3.2. The vector polynomial consisting of higher-order terms

$$\mathbf{G}(\mathbf{C},\mathbf{D},\mu,\nu) = \mathcal{O}(|\mu|^2\|\mathbf{C}+\mathbf{D}\|, |\nu|^2\|\mathbf{C}+\mathbf{D}\|^3, \|\mathbf{C}+\mathbf{D}\|^5)$$

represents the *terms not in normal form*.

*Remark* 3.7 (Higher-Order Normal Forms). In fact, one may apply additional normal form transformations that transform the additional terms in $\mathbf{G}$ into higher order terms in $P_\kappa, Q_\kappa$. In practice, we aim to carry out leading-order computations which are unaffected by these higher-order terms in the normal form. However, this theoretical consideration is important because it allows us to consider $\mathbf{G}$ as a small term. To do this, we would invoke a normal form theorem of arbitrarily high order $N$, resulting in terms in normal form $P_\kappa, Q_\kappa = \mathcal{O}(\|\mathbf{C}+\mathbf{D}\|^{N-2})$ and terms not in normal form $\mathbf{G} = \mathcal{O}(\|\mathbf{C}+\mathbf{D}\|^{N-1})$. Since we are concerned with small solutions, $\|\mathbf{C}+\mathbf{D}\|$ near 0, the terms not in normal form $\mathbf{G}$ are arbitrarily small.

Importantly, the terms in normal form $P_\kappa, Q_\kappa$ still posses the rotational symmetry $\mathcal{R}_\theta$, regardless of the fact that we do not compute their explicit form. This is a basic consequence of the normal form theorem, as can be found in [30].

These transformations are independent of each other and so we may compute them in any order we choose. The $A_\kappa, B_\kappa$-cubic transformation $\Phi_{3,0,0}$ is similar to the computation in Chapter 2 and is carried out in detail in [33], so we omit it here. We first compute the quadratic, $\nu$-dependent transformation, following the approach of [33]. Afterwards, we compute the linear, $\mu$-dependent transformation, which turns out to be

the most important for quantifying the selected wavenumbers in the following sections.

Consider the quadratic part of (3.15) with $\mu = 0$

$$\begin{aligned}
A_0' &= -\mathrm{i}A_0 + B_0 + \tfrac{\mathrm{i}}{4}\nu(a_0^2 + 2a_+\overline{a_+}) \\
B_0' &= -\mathrm{i}B_0 - \tfrac{1}{4}\nu(a_0^2 + 2a_+\overline{a_+}) \\
A_+' &= \tfrac{\mathrm{i}}{2}A_+ + B_+ - 2\mathrm{i}\nu(2a_0a_+) \\
B_+' &= \tfrac{\mathrm{i}}{2}B_+ - \nu(2a_0a_+) \\
A_-' &= \tfrac{\mathrm{i}}{2}A_- + B_- - 2\mathrm{i}\nu(2a_0\overline{a_+}) \\
B_-' &= \tfrac{\mathrm{i}}{2}B_- - \nu(2a_0\overline{a_+})
\end{aligned} \tag{3.17}$$

where again $a_0 = A_0 + \overline{A}_0$ and $a_+ = A_+ + \overline{A}_-$.

**Lemma 3.5** (Quadratic Normal Form)**.** *There exist six homogeneous polynomials $\Theta_0, \Theta_\pm, \Pi_0, \Pi_\pm$ of degree two in the complex variables $\mathbf{C} = (C_0, C_+, C_-, c.c.), \mathbf{D} = (D_0, D_+, D_-, c.c.)$ such that the change of variables*

$$\begin{aligned}
A_0 &= C_0 + \nu\Theta_0(\mathbf{C},\mathbf{D}), \qquad & B_0 &= D_0 + \nu\Pi_0(\mathbf{C},\mathbf{D}) \\
A_\pm &= C_\pm + \nu\Theta_\pm(\mathbf{C},\mathbf{D}), \qquad & B_\pm &= D_\pm + \nu\Pi_\pm(\mathbf{C},\mathbf{D})
\end{aligned} \tag{3.18}$$

*transforms* (3.17) *into*

$$\begin{aligned}
C_0' &= -\mathrm{i}C_0 + D_0 \\
D_0' &= -\mathrm{i}D_0 - \tfrac{1}{4}\nu\left(2\overline{C_+C_-} - 2\mathrm{i}(\overline{C_+D_-} + \overline{C_-D_+})\right) \\
C_+' &= \tfrac{\mathrm{i}}{2}C_+ + D_+ \\
D_+' &= \tfrac{\mathrm{i}}{2}D_+ - \nu\left(2\overline{C_0C_-} + 4\mathrm{i}(\overline{C_-D_0} + \overline{C_0D_-})\right) \qquad + \mathcal{O}(|\nu|^2\|\mathbf{C}+\mathbf{D}\|^3) \\
C_-' &= \tfrac{\mathrm{i}}{2}C_- + D_- \\
D_-' &= \tfrac{\mathrm{i}}{2}D_- - \nu\left(2\overline{C_0C_+}4\mathrm{i}(\overline{C_+D_0} + \overline{C_0D_+})\right).
\end{aligned} \tag{3.19}$$

This lemma is a direct consequence of the normal form theorem in [30, Section 3.2], but we provide a constructive proof below. Our constructive proof computes not only the normal form equation (3.19), but also the change of coordinates needed to get there. We're not aware of a reference where these computations have been fully carried out and doing so is necessary for computing the effect of the inhomogeneous parameter $\mu(x)$, as

explained in Section 3.4.2.

*Proof.* To ease notation, we use the variables

$$U = (A_0, B_0, A_+, B_+, A_-, B_-)^\top$$
$$V = (\mathbf{C}, \mathbf{D})^\top = (C_0, D_0, C_+, D_+, C_-, D_-)^\top.$$

We also let $\nu R(U) = \nu(R_0, Q_0, R_+, Q_+, R_-, Q_-)^\top$ be the quadratic terms on the right hand side of (3.17). We let $\nu N = \nu(N_0, M_0, N_+, M_+, N_-, M_-)^\top$ be a quadratic polynomial representing the terms in the normal form equation. Now we may rewrite (3.17) as

$$U' = LU + \nu R(U) \tag{3.20}$$

and rewrite (3.19) as

$$V' = LV + \nu N(V) \tag{3.21}$$

where in both we use

$$L = \begin{bmatrix} -\mathrm{i} & 1 & 0 & 0 & 0 & 0 \\ 0 & -\mathrm{i} & 0 & 0 & 0 & 0 \\ 0 & 0 & \frac{\mathrm{i}}{2} & 1 & 0 & 0 \\ 0 & 0 & 0 & \frac{\mathrm{i}}{2} & 0 & 0 \\ 0 & 0 & 0 & 0 & \frac{\mathrm{i}}{2} & 1 \\ 0 & 0 & 0 & 0 & 0 & \frac{\mathrm{i}}{2} \end{bmatrix}.$$

We seek a transformation of the form

$$U = V + \nu\Phi(V) := V + \nu\left(\Theta_0(V), \Pi_0(V), \Theta_+(V), \Pi_+(V), \Theta_-(V), \Pi_-, c.c.\right)^\top. \tag{3.22}$$

Differentiating this equation and using both (3.20) and (3.21), arrange terms and divide out a factor of $\nu$ to arrive at

$$D\Phi \cdot LV - L \cdot \Phi(V) = R(V + \nu\Phi(V)) - N(V) + D\Phi \cdot N(V) \tag{3.23}$$

We use the left-hand side to define the *homological operator* $\mathcal{A}_L^2$ on the space $\mathcal{P}_2^6$ of quadratic, vector-valued polynomials on $\mathbb{C}^6$.

$$\mathcal{A}_L^2 \colon \mathcal{P}_2^6 \to \mathcal{P}_2^6 \tag{3.24}$$

$$\Psi(V) \mapsto \mathcal{A}_L^2\left(\Psi(V)\right) := D\Psi \cdot LV - L \cdot \Psi(V). \tag{3.25}$$

Using the fact that $\Phi, N, R$ are all of order $\|V\|^2$, we can expand terms on the right of (3.23), group higher order terms, and rewrite it as

$$\mathcal{A}_L^2 \Phi = R(V) - N(V) + \mathcal{O}(|\nu|^2 \|V\|^3). \tag{3.26}$$

Next, we drop the higher order terms and rewrite the left hand side in terms of a new linear operator on quadratic, scalar polynomials

$$\mathcal{D} \colon \mathcal{P}_2 \to \mathcal{P}_2 \tag{3.27}$$

$$f \mapsto \mathcal{D}\left(f\right) := \partial_{C_0}(-\mathrm{i}C_0 + D_0) + \partial_{D_0} f(-\imath D_0) \tag{3.28}$$

$$+ \partial_{C_+} f(\tfrac{\mathrm{i}}{2}C_+ + D_+) + \partial_{D_+} f(D_+) \tag{3.29}$$

$$+ \partial_{C_-} f(\tfrac{\mathrm{i}}{2}C_- + D_-) + \partial_{D_-} f(D_-) + c.c. \tag{3.30}$$

Now we can rewrite (3.23) as a set of scalar equations

$$(\mathcal{D} + \mathrm{i})\Theta_0 - \Pi_0 = R_0 - N_0 \tag{3.31}$$

$$(\mathcal{D} + \mathrm{i})\Pi = Q_0 - M_0 \tag{3.32}$$

$$(\mathcal{D} + \tfrac{\mathrm{i}}{2})\Theta_+ - \Pi_+ = R_+ - N_+ \tag{3.33}$$

$$(\mathcal{D} + \tfrac{\mathrm{i}}{2})\Pi_+ = Q_+ - M_+ \tag{3.34}$$

$$(\mathcal{D} + \tfrac{\mathrm{i}}{2})\Theta_- - \Pi_- = R_- - N_- \tag{3.35}$$

$$(\mathcal{D} + \tfrac{\mathrm{i}}{2})\Pi_- = Q_- - M_- \tag{3.36}$$

Recall that we know $R_\kappa, Q_\kappa$ and that our aim is to find solutions $\Theta_\kappa, \Pi_\kappa, N_\kappa, M_\kappa$. To do this, our next goal is to find the range of the operators $(\mathcal{D} + \mathrm{i})$ and $(\mathcal{D} - \frac{\mathrm{i}}{2})$. By computing the kernel of the adjoints with respect to a unique scalar product on $\mathcal{P}_2$

(discussed in [30, §3.1]), we obtain

$$\mathrm{Rg}(\mathcal{D}+\mathrm{i}) = \{\overline{C}_+^2, \overline{C}_-^2, \overline{C}_+\overline{C}_-, \overline{C}_-\overline{D}_+ - \overline{C}_+\overline{D}_-\}^\perp \tag{3.37}$$

$$\mathrm{Rg}(\mathcal{D}+\tfrac{\mathrm{i}}{2}) = \{\overline{C}_0\overline{C}_+, \overline{C}_0\overline{C}_-, \overline{C}_+\overline{D}_0 - \overline{C}_0\overline{D}_+, \overline{C}_-\overline{D}_0 - \overline{C}_0\overline{D}_-\}^\perp \tag{3.38}$$

Now proceed with solving the first two equations above. Starting with (3.32), note that

$$Q_0 = \tfrac{-1}{2}\overline{C}_+\overline{C}_- + \{\text{terms} \in \mathrm{Rg}(\mathcal{D}+\mathrm{i})\}$$

Choose $M_0 = \frac{-1}{2}\overline{C}_+\overline{C}_- + S_0$ for some $S_0 \in \mathrm{Rg}(\mathcal{D}+\mathrm{i})$ so that (3.32) can be satisfied with an appropriate choice of $\Pi_0$. Now considering (3.31), recall

$$R_0 = \tfrac{\mathrm{i}}{2}\overline{C}_+\overline{C}_- + \{\text{terms} \in \mathrm{Rg}(\mathcal{D}+\mathrm{i})\}$$

We can satisfy (3.31) by choosing $N_0 = 0$ and $S_0 = \frac{\mathrm{i}}{4}(\overline{C}_+\overline{D}_- + \overline{C}_-\overline{D}_+)$. Since

$$\Pi_0 = (\mathcal{D}+\mathrm{i})^{-1}(-S_0 + \{\text{terms} \in \mathrm{Rg}(\mathcal{D}+\mathrm{i})\}),$$

this choice of $S_0$ ensures that $\Pi_0$ includes a term of the form $(\mathcal{D}+\mathrm{i})^{-1}(-S_0) = \frac{-\mathrm{i}}{2}\overline{C}_+\overline{C}_-$, which then cancels with the $R_0$ in (3.31). We have now satisfied both (3.31) and (3.32) and solved for $N_0, M_0$. By tracking the additional terms, here omitted for brevity, one may also explicitly solve for $\Theta_0, \Pi_0$. (This will be carried out in the proof for the linear, $\mu$-dependent normal for transformation below.)

We should note that our choices for $N_0$ and $S_0$ amount to projecting along a decomposition of $\mathcal{P}_2^6$ chosen to be orthogonal with respect to the specific scalar product mentioned above. In particular, the choice of this scalar product ensures $\left(\mathcal{A}_L^2\right)^{\mathrm{ad}} = \mathcal{A}_{L^{\mathrm{ad}}}^2$ and the orthogonal projection onto the kernel of $\mathcal{A}_{L^{\mathrm{ad}}}^2$ leaves $\mathcal{P}_2^6$ invariant.

A similar method is employed to solve (3.33)-(3.36). □

The final normal form transformation is the most important in computing the $\mathcal{O}(\varepsilon)$ terms in the bounds on the selected wavenumbers, which is our ultimate goal. This transformation is applied inhomogeneously in the spatial variable, to match the parameter $\mu(x)$. In essence, we apply the normal form theory once for $x < 0$ with $\mu(x) = \varepsilon^2$

and again for $x > 0$ with $\mu(x) = -\varepsilon^2$. This results in two separate phase spaces, a difficulty addressed in the next section. For now, we state the results for a constant $\mu$, which could be negative or positive, then apply them once in each case.

Consider the linear part of equation (3.15)

$$\begin{aligned}
A_0' &= -\mathrm{i}A_0 + B_0 + \tfrac{\mathrm{i}}{4}\mu(A_0 + \overline{A_0}) \\
B_0' &= -\mathrm{i}B_0 - \tfrac{1}{4}\mu(A_0 + \overline{A_0}) \\
A_+' &= \tfrac{\mathrm{i}}{2}A_+ + B_+ - 2\mathrm{i}\mu(A_+ + \overline{A_-}) \\
B_+' &= \tfrac{\mathrm{i}}{2}B_+ - \mu(A_+ + \overline{A_-}) \\
A_-' &= \tfrac{\mathrm{i}}{2}A_- + B_- - 2\mathrm{i}\mu(\overline{A_+} + A_-) \\
B_-' &= \tfrac{\mathrm{i}}{2}B_- - \mu(\overline{A_+} + A_-)
\end{aligned} \tag{3.39}$$

**Lemma 3.6** (Linear Normal Form)**.** *There exist six linear maps $\Lambda_0, \Lambda_\pm, \Gamma_0, \Gamma_\pm$ such that for $\mu$ sufficiently small, the linear change of variables such that the change of variables*

$$\begin{aligned}
A_0 &= C_0 + \mu\Lambda_0(\mathbf{C}, \mathbf{D}), \qquad & B_0 &= D_0 + \mu\Gamma_0(\mathbf{C}, \mathbf{D}) \\
A_\pm &= C_\pm + \mu\Lambda_\pm(\mathbf{C}, \mathbf{D}), \qquad & B_\pm &= D_\pm + \mu\Gamma_\pm(\mathbf{C}, \mathbf{D})
\end{aligned} \tag{3.40}$$

*transforms* (3.39) *into*

$$\begin{aligned}
C_0' &= -\mathrm{i}C_0 + D_0 \\
D_0' &= -\mathrm{i}D_0 + \tfrac{1}{4}\mu\left(-C_0 - \mathrm{i}D_0\right) \\
C_+' &= \tfrac{\mathrm{i}}{2}C_+ + D_+ \\
D_+' &= \tfrac{\mathrm{i}}{2}D_+ + \mu\left(-C_+ - 2\mathrm{i}D_+\right) \\
C_-' &= \tfrac{\mathrm{i}}{2}C_- + D_- \\
D_-' &= \tfrac{\mathrm{i}}{2}D_- + \left(-C_- - 2\mathrm{i}D_-\right).
\end{aligned} + \mathcal{O}(|\mu|^2\|\mathbf{C} + \mathbf{D}\|) \tag{3.41}$$

*Proof.* Using the same notation as in the proof of Lemma 3.5, we seek a transformation of the form

$$U = V + \mu\Phi(V) := V + \mu\left(\Lambda_0(V), \Gamma_0(V), \Lambda_+(V), \Gamma_+(V), \Lambda_-(V), \Gamma_-(V)\right)^\top. \tag{3.42}$$

Differentiating, rearranging terms, truncating higher order terms in $\mu$ leads us to a

homological equation

$$\mathcal{A}_L^1\Phi := D\Phi \cdot LV - L\Phi(V) = R(V) - N(V), \tag{3.43}$$

where now the homological operator $\mathcal{A}_L^1$ is linear and acts on the space of vector-valued, "linear polynomials" $\mathcal{P}_1^6 = \{\Psi\colon \mathbb{C}^6 \to \mathbb{C}^6\}$. The problem, to solve for $\Phi, N$ is now explicitly one of finite dimensional linear algebra. Still, it is easiest to use the same framework in the proof of Lemma 3.5, above. We break apart equation (3.43) into six scalar equations

$$(\mathcal{D} + \mathrm{i})\Lambda_0 - \Gamma_0 = R_0 - N_0 \tag{3.44}$$

$$(\mathcal{D} + \mathrm{i})\Gamma = Q_0 - M_0 \tag{3.45}$$

$$(\mathcal{D} + \tfrac{\mathrm{i}}{2})\Lambda_+ - \Gamma_+ = R_+ - N_+ \tag{3.46}$$

$$(\mathcal{D} + \tfrac{\mathrm{i}}{2})\Gamma_+ = Q_+ - M_+ \tag{3.47}$$

$$(\mathcal{D} + \tfrac{\mathrm{i}}{2})\Lambda_- - \Gamma_- = R_- - N_- \tag{3.48}$$

$$(\mathcal{D} + \tfrac{\mathrm{i}}{2})\Pi_- = Q_- - M_- \tag{3.49}$$

We compute the range in the space of linear polynomials $\mathcal{P}_1 = \{f\colon \mathbb{C}^6 \to \mathbb{C}\}$ of the operators on the left

$$\mathrm{Rg}(\mathcal{D} + \mathrm{i}) = \{C_0\}^\top \qquad\qquad \mathrm{Rg}(\mathcal{D} - \tfrac{\mathrm{i}}{2}) = \{C_+, C_-\}. \tag{3.50}$$

Next, we solve (3.45). Recalling that $Q_0 = \frac{-1}{4}(C_0 + \overline{C}_0)$, we choose $M_0 = \frac{-1}{4}C_0 + S_0$ and will set $S_0$ later. Now we may legititmately set $\Gamma_0 = (\mathcal{D} + \mathrm{i})^{-1}\left(\frac{-1}{4}\overline{C_0} - S_0\right)$ and compute it once we choose $S_0$. Turning to (3.44), we have

$$\begin{aligned}(\mathcal{D} + \mathrm{i})\Lambda_0 &= \Gamma_0 + R_0 - N_0 \\ &= (\mathcal{D} + \mathrm{i})^{-1}(\tfrac{-1}{4}\overline{C_0}) - (\mathcal{D} + \mathrm{i})^{-1}S_0 + \tfrac{\mathrm{i}}{4}(C_0 + \overline{C}_0) - N_0 \\ &= (\mathcal{D} + \mathrm{i})^{-1}(\tfrac{-1}{4}\overline{C_0}) + \tfrac{\mathrm{i}}{4}\overline{C}_0\end{aligned}$$

by choosing $N_0 = 0$ and $S_0 = \frac{i}{4}D_0$, so that $(\mathcal{D} + \mathrm{i})^{-1}S_0 = \frac{\mathrm{i}}{4}C_0$. Continuing on the right

hand side, we compute

$$(\mathcal{D}+\mathrm{i})\Lambda_0 = \tfrac{3\mathrm{i}}{8}\overline{C}_0 + \tfrac{\mathrm{i}}{8}\overline{D}_0.$$

Now we can invert $(\mathcal{D}+\mathrm{i})$ and obtain

$$\Lambda_0 = \tfrac{3}{16}\overline{C}_0 + \tfrac{1}{8}\overline{D}_0 \tag{3.51}$$

$$\Gamma_0 = (\mathcal{D}+\mathrm{i})^{-1}\left(\tfrac{-1}{4}\overline{C_0} - S_0\right) \tag{3.52}$$

$$= (\mathcal{D}+\mathrm{i})^{-1}\left(\tfrac{-1}{4}\overline{C_0} - \tfrac{\mathrm{i}}{4}D_0\right) \tag{3.53}$$

$$= \tfrac{-\mathrm{i}}{4}C_0 + \tfrac{\mathrm{i}}{8}\overline{C}_0 - \tfrac{1}{16}\overline{D}_0. \tag{3.54}$$

Most of these computations were verified using the computer algebra system Mathematica.

Using similar procedures, one obtains the normal form terms $N_\pm, M_\pm$ as seen in equation (3.41) and the full normal form transformation

$$U = V + \mu\Phi(V) = V + \mu\begin{bmatrix}\Lambda_0(V)\\ \Gamma_0(V)\\ \Lambda_+(V)\\ \Gamma_+(V)\\ \Lambda_-(V)\\ \Gamma_-(V)\end{bmatrix} \tag{3.55}$$

$$= V + \mu\begin{bmatrix}\tfrac{3}{16}\overline{C}_0 + \tfrac{\mathrm{i}}{8}\overline{D}_0\\ \tfrac{-\mathrm{i}}{4}C_0 + \tfrac{\mathrm{i}}{8}\overline{C}_0 - \tfrac{1}{16}\overline{D}_0\\ 3\overline{C}_- - 4\mathrm{i}\overline{D}_-\\ 2\mathrm{i}C_+ - \mathrm{i}\overline{C}_- - \overline{D}_-\\ 3\overline{C}_+ - 4\mathrm{i}\overline{D}_+\\ 2\mathrm{i}C_- - \mathrm{i}\overline{C}_+ - \overline{D}_-\end{bmatrix}. \tag{3.56}$$

□

### 3.4.1 Additional Coordinate Changes

The last steps to obtain the amplitude equations from the normal form in equations (3.16) is to move to a co-rotating reference frame and to apply a convenient rescaling. We search for solutions of the form $\begin{bmatrix}\mathbf{C}\\ \mathbf{D}\end{bmatrix} = e^{Rx}\begin{bmatrix}\widetilde{\mathbf{C}}\\ \widetilde{\mathbf{D}}\end{bmatrix}$ where $R = \mathrm{diag}(-\mathrm{i}, -\mathrm{i}, \frac{\mathrm{i}}{2}, \frac{\mathrm{i}}{2}, \frac{\mathrm{i}}{2}, \frac{\mathrm{i}}{2})$ and with the scaling

$$\hat{x} = \varepsilon x, \quad \nu = \varepsilon\delta, \quad \widetilde{C_\kappa} = \varepsilon c_\kappa, \quad \widetilde{D_\kappa} = \varepsilon^2 d_\kappa, \qquad \text{for each } \kappa \in \{0, +, -\}. \tag{3.57}$$

In these coordinates, after dropping the $\hat{}$, the normal form equations become

$$\begin{aligned} c_0' &= d_0 \\ d_0' &= \tfrac{1}{4}\left(P_0(\mathbf{c}) - \mathrm{i}\varepsilon Q_0(\mathbf{c},\mathbf{d})\right) \\ c_+' &= d_+ \\ d_+' &= \left(P_+(\mathbf{c}) + \varepsilon 2\mathrm{i} Q_+(\mathbf{c},\mathbf{d})\right) \\ c_-' &= d_- \\ d_-' &= \left(P_-(\mathbf{c}) + \varepsilon 2\mathrm{i} Q_-(\mathbf{c},\mathbf{d})\right) \end{aligned} + \mathbf{g}(\mathbf{c},\mathbf{d},e^{\mathrm{i}x/\varepsilon};\varepsilon,\delta) \tag{3.58}$$

where now $\varepsilon$-dependence has been scaled out of the polynomials

$$\begin{aligned} P_{\kappa=0}(\mathbf{c}) &= \operatorname{sgn} x c_0 - \nu 2\overline{c_+ c_-} + 3c_0(|c_0|^2 + 2|c_+|^2 + 2|c_-|^2) \\ Q_{\kappa=0}(\mathbf{c},\mathbf{d}) &= \operatorname{sgn} x d_0 - \nu 2(\overline{c_+}\,\overline{d_-} + \overline{c_-}\,\overline{d_+}) \\ &\quad + 3c_0\left(c_0\overline{d_0} + \overline{c_0}d_0 + 2(\overline{c_+}d_+ + c_+\overline{d_+}) + 2(\overline{c_-}d_- + c_-\overline{d_-})\right) \\ &\quad + 3d_0(|c_0|^2 + 2|c_+|^2 + 2|c_-|^2) \end{aligned}$$

and the terms not in normal form have a rotational component denoted by a complex exponential in the argument

$$\mathbf{g}(\mathbf{c},\mathbf{d},e^{\mathrm{i}x/\varepsilon};\varepsilon,\delta) = \mathcal{O}(\varepsilon^3).$$

The reader my now identify equations (3.1) by disregarding the terms with an $\varepsilon$. However, this requires further justification because (3.58) represents *two* normal form equations (for the reduced vector field on the center subspace); one for $x < 0$ and one for $x > 0$. These are each obtained by slightly different normal form transformations, because the $A_\kappa, B_\kappa$-linear and $\mu$-dependent transformation is different for each of $\mu = -\varepsilon^2$ and $\mu = \varepsilon^2$. Thus, these two equations govern dynamics in two different phase spaces.

### 3.4.2 Different Phase Spaces

We wish to compare objects two different phase spaces, corresponding to the two equations for each of $x < 0$ and $x > 0$ that differ only by a sign on a linear term. In order to do this, we compute a transformation that takes the variables of the $x > 0$ equation and rewrites them in the variables of the $x < 0$ equation. The important part of this transformation comes from the linear, $\mu$-dependent normal form transformation $\Phi_{1,1,0}(\mu)$, which we computed in Section 3.4. In particular, we must compute $[\Phi_{1,1,0}(\varepsilon^2)]^{-1} \circ \Phi_{1,1,0}(-\varepsilon^2)$.

Figure 3.2 shows a schematic diagram which describes all of the coordinate changes and transformations. At the top is the variable $u$, which is a four-times differentiable function that solves the steady-state Swift-Hohenberg equation with spatial inhomogeneity (1.4). Next down is the vector function $U(x)$, where each of its entries is a periodic function in $y$. We treat $x$ as the evolution variable and conduct a center manifold reduction to arrive at the variable $U_C = (A_\kappa, B_\kappa)$. These two steps are described in Section 3.3. The next three steps down are described in Section 3.4 and depict the cubic normal form transformation, the quadratic $\nu$-dependent normal form transformation, and then finally two different linear $\mu$-dependent normal form transformations. Since these last two are indeed different coordinate changes, they split the phase space. The final two transformations on both sides correspond to moving to a co-rotating reference frame and rescaling, as described in Section 3.4.1. The final coordinate change along the bottom is described in the next lemma.

**Lemma 3.7** (Translation between Phase Spaces)**.** *There is an coordinate change* $\mathcal{T} : \mathbb{C}^6 \to \mathbb{C}^6$ *from the variables of equations* (3.58) *with* $x > 0$ *to the variables of* (3.58) *with* $x < 0$.

*At leading order, the transformation depends only on $x, \varepsilon$ and can be written as*

$$v_{<0} = \mathcal{T}(\varepsilon)v_{>0} = v_{>0} + \varepsilon \begin{bmatrix} 0 \\ -\frac{i}{4}(2c_0 - \overline{c_0}e^{2\mathrm{i}x}) \\ 0 \\ 2\mathrm{i}(2c_+ - \overline{c_-}e^{-\mathrm{i}x}) \\ 0 \\ 2\mathrm{i}(2c_- - \overline{c_+}e^{-\mathrm{i}x}) \end{bmatrix} + \mathcal{O}(\varepsilon^2) \tag{3.59}$$

*Proof.* The transformation is simply the composition of rescaling, co-rotating, and the two normal forma transformations $\Phi_{1,1,0}(\varepsilon^2), \Phi_{1,1,0}(-\varepsilon^2)$. We find the leading-order formula by direct computation. □

Applying the transformation of Lemma 3.7 to equations (3.58), we compute the leading-order full, inhomogeneous (i.e. non-autonomous) equations in the $x < 0$ variables $(c_\kappa, d_\kappa)$

$$\begin{aligned} c_0' &= d_0 - \varepsilon\chi_0(x)\tfrac{\mathrm{i}}{4}(2c_0 - \overline{c_0}e^{2\mathrm{i}x}) \\ d_0' &= \tfrac{1}{4}\left(P_0(\mathbf{c}) - \varepsilon\mathrm{i}Q_0(\mathbf{c},\mathbf{d}) + \varepsilon\chi_0(x)\mathrm{i}(2d_0 - \overline{d_0}e^{2\mathrm{i}x} - 2\mathrm{i}\overline{c_0}e^{2\mathrm{i}x})\right) \\ c_+' &= d_+ + \varepsilon\chi_0(x)2\mathrm{i}(2c_+ - \overline{c_-}e^{-\mathrm{i}x}) \\ d_+' &= P_+(\mathbf{c}) + \varepsilon 2\mathrm{i}Q_+(\mathbf{c},\mathbf{d}) - \varepsilon\chi_0(x)2\mathrm{i}(2d_+ - \overline{d_-}e^{-\mathrm{i}x} - i\overline{c_-}e^{-\mathrm{i}x}) \\ c_-' &= d_- + \varepsilon\chi_0(x)2\mathrm{i}(2c_- - \overline{c_+}e^{-\mathrm{i}x}) \\ d_-' &= P_-(\mathbf{c}) + \varepsilon 2\mathrm{i}Q_-(\mathbf{c},\mathbf{d}) - \varepsilon\chi_0(x)2\mathrm{i}(2d_- - \overline{d_+}e^{-\mathrm{i}x} - i\overline{c_+}e^{-\mathrm{i}x}) \end{aligned} + \mathbf{g}_{\mathcal{T}}(x, \mathbf{c}, \mathbf{d}, e^{\mathrm{i}x/\varepsilon}; \varepsilon, \delta) \tag{3.60}$$

where $P_\kappa, Q_\kappa$ are still understood to have $\mathrm{sgn}(x)$ in their linear order terms, with

$$\chi_0(x) = \begin{cases} 0, & x < 0 \\ 1, & x > 0 \end{cases},$$

and $\mathbf{g}_{\mathcal{T}} = \mathcal{O}(\varepsilon^3)$ is now piecewise-defined on the real line, representing terms not in normal form on both sides of $x = 0$.

To ease notation, we rewrite (3.60) as a single vector equation in the variable $v =$

$(c_0, d_0, c_+, d_+, c_-, d_-)^\top \in \mathbb{C}^6$ and obtain

$$v' = n(x, v; \delta, \varepsilon) + \varepsilon\chi_0(x)T(v, e^{\mathrm{i}x}) + g(x, v, e^{\mathrm{i}x/\varepsilon}; \varepsilon, \delta). \tag{3.61}$$

Here $n(x, v; \delta, \varepsilon)$ denotes the terms in normal form, including the inhomogeneous linear terms with $\mathrm{sgn}(x)$ and the $\varepsilon$-terms. The function $T$ denotes the terms stemming from the transformation $\mathcal{T}$ of Section 3.4.2. The function $g = \mathbf{g}_{\mathcal{T}}$.

### 3.4.3 Persistent Dynamics

We wish to approximate the dynamics of the last equation by the $\mathcal{O}(\varepsilon^0)$ amplitude equations of Section 3.2. As mentioned before, this involves two steps. First, is a technical consideration already discussed in Chapter 2. The issue has to do with the terms $g$ that are not in normal form, and thus do not have the invariance under the rotation $\mathcal{R}_\theta$. (Recall that these terms can be forced to be of arbitrarily high order in $\varepsilon$ by using a higher-order normal form.) Note that these terms have rapidly oscillating behavior in the form of $e^{\mathrm{i}x/\varepsilon}$. As in Section 2.4.2 results from [39, 21, 22] tell us that the relevant equilibria, periodic orbits, and invariant manifolds do indeed persist with these $\varepsilon^3$-perturbations. Thus we may drop the $g$. The second step is appealing to standard ODE theory and the invariance of a flow under small perturbations. Thus we may drop the $\mathcal{O}(\varepsilon)$ terms consisting of the $Q_\kappa$ and the terms with $\chi_0$. We have proved the following theorem which

**Proposition 3.8.** *For sufficiently small $\varepsilon > 0$, all small and bounded solutions to the steady-state Swift-Hohenberg equation* (1.4) *are captured by* (3.61)*. Furthermore, the dynamics of* (3.61) *are "$\varepsilon$-close" to the dynamics of the amplitude equations* (3.1)*.*

In Section 3.2, we discussed the invariant manifolds of ODEs (3.7) (for $x < 0$) and (3.5) (for $x > 0$). We argued, with the help of numerics in Section 4.1.2, that the inhomogeneous equation (3.2) possesses a family of heteroclinic orbits $\mathbf{c}_*(\theta)$ resulting from the circle of intersection $\mathcal{S} = \mathcal{W}^{cu}_{\mathcal{P}} \cap \mathcal{W}^s$ of the unstable manifold of periodic orbits and the stable manifold of the zero equilibrium. The goal of this section is to provide evidence that these heteroclinics persist in (3.61), with $\varepsilon$-perturbations. This is accomplished by arguing that the intersection $\mathcal{S}$ is transverse. In doing so, we outline

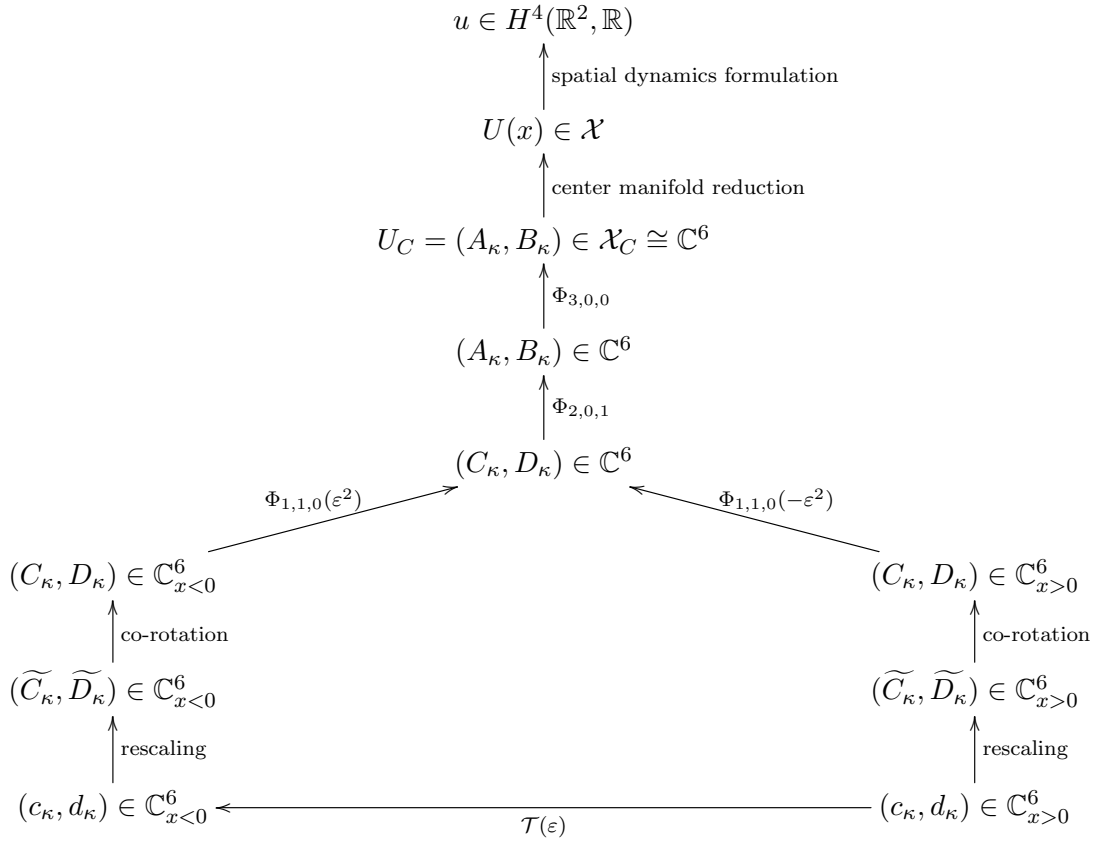


Figure 3.2: A schematic summary of all phase spaces, variables, and coordinate changes.

a framework for computing the wavenumber of the periodic orbits on the left of the heteroclinic.

Theorem 3.1 implies that the following equilibria, periodic orbits, and invariant manifolds all persist, most now with a dependence on small $\varepsilon$.

$$\begin{array}{rl} \text{in equations (3.1)} & \text{in equations (3.61)} \\ \mathbf{c}_0 & \longrightarrow \mathbf{c}_0(\varepsilon) \equiv \mathbf{c}_0 \equiv 0 \\ \mathcal{P} & \longrightarrow \mathcal{P}(\varepsilon) \\ \mathcal{W}^s & \longrightarrow \mathcal{W}^s(\varepsilon) \\ \mathcal{W}^{cu}_{\mathcal{P}} & \longrightarrow \mathcal{W}^{cu}_{\mathcal{P}}(\varepsilon) \end{array}$$

In particular, the invariant manifolds certainly retain their dimension and, by the same dimension-counting at the end of Section 3.2, we have another hint that the intersection should persist in the absence of some degeneracy.

**Hypothesis 2.** *The intersection of Proposition 3.4 is transverse.*

This hypothesis is verified numerically by relating the geometric notion of transversality to the invertibility of a linear operator in a functional equation, and then solving this equation numerically. This relation is a typical bridge between the intuitive geometry and more elegant methods of proof from functional analysis. See the brief discussion, with references, in Section 1.3.4. To utilize this, we establish the appropriate equation using a technique called *far field core* (FFC) decomposition. This technique is designed for easy numerical implementation, which we do in Section 4.1 and obtain numerical evidence that supports the hypothesis above.

As a corollary to this transversality, we obtain the existence of heteroclinics for $\varepsilon > 0$, comparable to the Corollary 2.15 for stripes.

**Corollary 3.9.** *The transverse intersection $\mathcal{S}$ in the phase space of* (3.1) *persists for sufficiently small $\varepsilon$ in* (3.61) *as $\mathcal{S}(\varepsilon)$. Consequently, there is also a family of heteroclinic orbits $\mathbf{c}_*(\theta;\delta,\varepsilon)$ from $\mathbf{c}_{\text{hex}}(\theta;\delta,\varepsilon) \to \mathbf{c}_0$.*

The remainder of this chapter is devoted to establishing the functional analytic framework which allows us verify our two main hypotheses numerically. Additionally, this framework provides a formula, in the form of a Melnikov-type integral, for the first term in the expansion of the strain-displacement relation, which could be applied if we had an explicit expression for the heteroclinic.

## 3.5 Conceptual Framework for Computing Strain-Displacement Relations

The main idea is to decompose the desired solution into the perfect periodic pattern in the farfield ($x \sim -\infty$) and a defect solution that is exponentially localized on a compact subset of the domain. Using this decomposition as an ansatz, we cast our problem as a well-posed equation on a function space with appropriately chosen exponential weight.

While an intersection of unstable and stable manifolds before corresponded to a family of heteroclinic connections, it now corresponds to a family of localized solutions. This method is referred to as a *farfield-core* (FFC) decomposition and has been used in similar situations in [58, 47].

The FFC method provides us with two major advantages. First, it allows us to numerically check transversality by implementing what amounts to a boundary value problem on a large domain. We carry out this check in Section 4.1. Second, FFC provides an analytical path towards computing the leading-order terms of the strain-displacement relation. Since transversality now corresponds to an invertible linearization, the Implicit Function Theorem provides a formula for the wavenumber in terms of the parameters $\varepsilon, \delta$ and the phase of the asymptotic pattern. Below, we state this formula and note that it is only explicit assuming we have a heteroclinic solutions.

*Remark* 3.8. Comparing with the case of stripes in Chapter 2, one may view FFC as a substitute for the conserved quantities readily available in the simpler amplitude equations for stripes. These allowed us to set up a finite system of equations which may be compared to the functional equation obtained below. The 2D SH equation with quadratic terms also possesses a conserved quantity, as seen in [48], which suggests that one might attempt an alternative to FFC or combination of the two approaches.

### 3.5.1 Farfield-Core Decomposition

To state the farfield-core functional equation, we truncate (3.61) to remove the term $g$, the part not in normal form, obtaining

$$v' = n(x, v; \delta, \varepsilon) + \varepsilon\chi_0(x)T(v, e^{\mathrm{i}x}). \tag{3.62}$$

Recall that $n$ stands for the terms in normal form and $T$ represents the terms originating from the half commutator of normal form transformations computed in Section 3.4.2. Next, we move to the the co-rotating reference frame $v \to \mathcal{R}_{kx}v = e^{\mathrm{i}Rxk}v$, previously used in Section 3.2. We arrive at an $\varepsilon$-perturbation of the rotated amplitude equations (3.9), rewritten as

$$v' = -kRv + n(x, v; \delta, \varepsilon) + \varepsilon\chi_0(x)T(\mathcal{R}_{xk}v, e^{\mathrm{i}x}) \tag{3.63}$$

Recall that the equations (3.9), possessed an equilibrium solution $\mathbf{c}_{\rm hex}(k;\delta)$ and all rotations $\mathbf{c}_{\rm hex}(k,\theta;\delta) := \mathcal{R}_\theta \mathbf{c}_{\rm hex}(k;\delta)$. These correspond to the asymptotic hexagonal patterns on the left and persist as $v_{\rm hex}(k,\theta;\delta,\varepsilon)$ with order $\varepsilon$-corrections.

Let $\chi(x)$ be a smooth function with $\chi(x) = 1$ for $x < \ell_1$ and $\chi(x) = 0$ for $x > \ell_2$ and with $\ell_1 < \ell_2 \ll -1$. Now we substitute a second ansatz

$$v = \chi(x) v_{\rm hex}(k,\theta;\delta,\varepsilon) + w \tag{3.64}$$

where $w$ is taken to be an exponentially localized function, made precise below. This represents the decomposition of solutions into a periodic part in the far field $v_{\rm hex}$ (constant due to our co-rotating frame) and $w$, an exponentially localized transition to zero. We now wish to solve

$$\begin{aligned} w' = &-\chi k R v_{\rm hex}(k,\theta;\delta,\varepsilon) - kRw + n\big(x, \chi v_{\rm hex}(k,\theta;\delta,\varepsilon) + w;\delta,\varepsilon\big) \\ &+ \varepsilon\chi_0 T\left(\chi \mathcal{R}_{xk} v_{\rm hex}(k,\theta;\delta,\varepsilon) + \mathcal{R}_{xk} w, e^{{\rm i}x}\right). \end{aligned} \tag{3.65}$$

In fact, if we allow ourselves to assume Hypothesis 1 (existence of a real heteroclinic), then we already have one solution when $\varepsilon = 0$. Recall that this hypothesis implies the existence of a real heteroclinic $\mathbf{c}_*(\delta)$ from $\mathbf{c}_{\rm hex}(\delta) \to \mathbf{c}_0$. This real solution is taken from the family of heteroclinics in Proposition 3.4 by fixing $\theta = 0$ and $k = 0$. In fact, for any $\theta \in [0, 2\pi)$, we have a heteroclinic $\mathbf{c}_*(\theta;\delta)$ from $\mathbf{c}_{\rm hex}(\theta;\delta) \to \mathbf{c}_0$.[3]

Fixing $\theta = \phi_* \in [0, 2\pi)$ and $\delta = \delta_* > \sqrt{3}/4$, we write

$$v_* := \mathbf{c}_*(\phi_*;\delta_*),$$

which now solves (3.63) when $\varepsilon = 0$ and $k = 0$. Thus, we also have an exponentially localized solution of (3.65)

$$w_* = v_* - \chi(x) v_{\rm hex}(0,\phi_*;\delta_*,0).$$

Let $p_* = (w_*, 0, \phi_*; \delta_*, 0)$. We now seek quadruples $(w, k, \theta; \delta, \varepsilon)$ near $p_*$ that solve (3.65).

[3]Importantly, we have only assumed one of our hypotheses. We have not assumed Hypothesis 2, that the $\varepsilon = 0$ intersection is transverse and thus persists for small $\varepsilon > 0$.

In order to apply the Implicit Function Theorem, we next write (3.65) as a functional equation in the exponentially weighted space $(L^2_\eta)^6$. Here $L^2_\eta$ has the half-weighted norm induced from $L^2$

$$\|u\|^2_{L^2_\eta} = \int_{-\infty}^0 (e^{-\eta x}|u(x)|)^2 \,\mathrm{d}x + \int_0^\infty |u(x)|^2 \,\mathrm{d}x.$$

The precise value of the weight $\eta$ is irrelevant, only that it must satisfy $0 < \eta \ll 1$ and should be chosen less than the smallest real part of the spatial eigenvalues of the linearization of (3.65) at one of the equilibria $v_{\mathrm{hex}}$.

Next we let $\mathcal{L}$ be the linearization of (3.65) at $p_*$,

$$\mathcal{L}(x)w := w' - n'(x, v_*; \delta_*, 0)w.$$

and let $N$ be the nonlinear part. Finally, we can define $\mathcal{F}\colon (H^1_\eta)^6 \to L^2_\eta)^6$ by

$$\mathcal{F}(w, k; \varepsilon) := \mathcal{L}(x)w - N(x, w, k, \phi_*; \delta_*, \varepsilon).$$

The full equation is now simply

$$\mathcal{F}(w, k; \varepsilon) = 0. \tag{3.66}$$

Well-posedness and smoothness of $\mathcal{F}$ can be seen by estimates on $x < \ell_2$ alone because of the $\chi = 0$ on the other half of the domain. We omit the details.

In Section 4.1, we find solutions to a numerical analogue of this problem for various small $\varepsilon > 0$. These solutions serve as our primary evidence of transversality of the $\varepsilon = 0$ intersection and, consequently, persistence of the heteroclinics for nonzero $\varepsilon$.

From another perspective, the convergence of the Newton's method involved in the numerical analogue suggests that some linearization of $\mathcal{F}$ at $p_*$ is invertible. This is the invertibility mentioned in Section 1.3.4 and, thanks to the FFC formulation, can be deduced from properties of $\mathcal{L}$.

**Proposition 3.10.** *In the following, all derivatives are evaluated at $p_*$. Suppose that*

*(i)* $\ker \mathcal{L} = \{0\}$

*(ii)* $\partial_k \mathcal{F} \notin \mathrm{Rg}(\mathcal{L})$.

*Then $\partial_{(w,k)}\mathcal{F}$ is invertible.*

*Proof.* Treating $k$ as a variable, we can compute

$$\partial_{(w,k)}\mathcal{F}|_{p_*}(x) = \left[\begin{array}{c|c} \mathcal{L}(x) & \partial_k N|_{p_*}(x) \end{array}\right]. \tag{3.67}$$

Using Palmer's ideas in [62, 63] we can see that $\mathcal{L}$ is Fredholm with index -1, because it generates exponential dichotomies on $(-\infty, 0]$ and $[0, \infty)$. Appending the derivative with respect to $k$ increases the index by 1, by an application of the Fredholm Alternative and our assumption *(ii)*. Therefore, we now have that $\partial_{(w,k)}\mathcal{F}$ is Fredholm with index 0. By our assumption *(i)* we can see that $\ker \partial_{(w,k)}\mathcal{F} = \{0\}$. Thus, $\partial_{(w,k)}\mathcal{F}$ is invertible.[4] □

The Implicit Function Theorem now provides existence of functions $g_w(\varepsilon), g_k(\varepsilon), g_\theta(\varepsilon)$ such that the triple $(g_w(\varepsilon), g_k(\varepsilon); \varepsilon)$ is a solution to (3.66) near $p_*$. Undoing the ansatz (3.64) with $w(\cdot) = g_w(\varepsilon)$ and $k = g_k(\varepsilon)$, we have a heteroclinic solution

$$v_{\text{het}}(x; k, \phi_*; \delta_*, \varepsilon) = \chi(x) v_{\text{hex}}(g_k(\varepsilon), \phi_*; \delta_*, \varepsilon) + g_w(\varepsilon)(x)$$

to equation (3.63). Note that the entire argument here can safely be repeated for any $\phi_* \in [0, 2\pi)$ and any $\delta > 0$, because $\partial_\theta \mathcal{F} \notin \text{Rg}(\mathcal{L})$ and $\partial_\delta \mathcal{F} \notin \text{Rg}(\mathcal{L})$.

### 3.5.2 A Melnikov-type Integral Formula

To go further, the Implicit Function Theorem combined with Lyaponuv-Schmidt reduction allows us to compute the leading coefficient in the expansion for $k = g_k(\varepsilon)$. As we shall see, this gives a non-trivial strain-displacement relation that is $\varepsilon$-close (in some sense) to the vertical line $\{k(\theta) = 0\}$ mentioned above.

**Corollary 3.11.** *Suppose that the hypotheses of Proposition 3.10 hold. Then we can compute the leading term $k_1$ in a strain-displacement relation $k = g_k(\varepsilon) = k_1\varepsilon + \mathcal{O}(\varepsilon^2)$,*

[4] This invertibility implies the transversality of Hypothesis 2 by the general equivalence discussed in Section 1.3.4.

*obtaining*

$$k_1(\phi_*;\delta_*) = -\frac{\langle \psi, \partial_\varepsilon \mathcal{F}|_{p_*}\rangle}{\langle \psi, \partial_k N|_{p_*}\rangle}. \tag{3.68}$$

*for any* $\psi \in \ker(\mathcal{L}^*)$.

*Proof.* We plug our new solution $(g_w(\varepsilon), g_k(\varepsilon); \varepsilon)$ into (3.66) and have

$$\mathcal{F}(g_w(\varepsilon), g_k(\varepsilon), \phi_*; \delta_*, \varepsilon) = 0, \qquad \text{for all sufficiently small } \varepsilon > 0.$$

Differentiating this equation with respect to $\varepsilon$ at $\varepsilon = 0$, we compute

$$\begin{aligned}\frac{\mathrm{d}}{\mathrm{d}\varepsilon}\mathcal{F} &= \partial_w \mathcal{F}|_{p_*}\frac{\mathrm{d}g_w}{\mathrm{d}\varepsilon} + \partial_k \mathcal{F}|_{p_*}\frac{\mathrm{d}g_k}{\mathrm{d}\varepsilon} + \partial_\varepsilon \mathcal{F}|_{p_*}\\ &= \mathcal{L}\frac{\mathrm{d}g_w}{\mathrm{d}\varepsilon} + \partial_k N|_{p_*} k_1 + \partial_\varepsilon \mathcal{F}|_{p_*}\\ &= 0\end{aligned}$$

Now, let $\psi \in \ker(\mathcal{L})$ and we use it to project the last equation onto the kernel. Recall that here the inner product $\langle \cdot, \cdot \rangle$ is the one on $(L^2_\theta)^6$, inherited from the weighted space $L^2_\eta$. We compute

$$\begin{aligned}0 &= \langle \psi, \mathcal{L}\frac{\mathrm{d}g_w}{\mathrm{d}\varepsilon}\rangle + \langle \psi \partial_k N|_{p_*} k_1\rangle + \langle \psi, \partial_\varepsilon \mathcal{F}|_{p_*}\rangle\\ &= \langle \mathcal{L}^*\psi, \frac{\mathrm{d}g_w}{\mathrm{d}\varepsilon}\rangle + k_1\langle \psi \partial_k N|_{p_*}\rangle + \langle \psi, \partial_\varepsilon \mathcal{F}|_{p_*}\rangle.\end{aligned}$$

The first term vanishes and we have the formula above by solving for $k_1$.

□

Unfortunately, the formula on the right is in terms of the heteroclinic $v_{\mathrm{het}}$ for which we do not have an analytical form. Still, we have provided a theoretical plan for computing the strain-displacement relation "explicitly". This is a novel contribution; we do not know of any other situations in the literature where a strain-displacement relation for a hexagonal pattern has been computed.

## 3.6 Proof of Theorem 3.1

Theorem 3.1 depends upon two hypotheses. Hypothesis 1 provides existence of a heteroclinic orbit in the real subspace of the amplitude equations (3.1). Rotating this solution via $\mathcal{R}_\theta$, we obtain a family of similar heteroclinics. This family also solves the full normal form equations (3.61) provided that $\varepsilon = 0$. Hypothesis 2 ensures that this family persists for small $\varepsilon > 0$. This persistence comes from the transversality of the intersection $\mathcal{W}^{cu}_{\mathcal{P}} \cap \mathcal{W}^s$, when $\varepsilon = 0$. Through Section 3.5, we reframed the problem as a functional equation and saw that this transversality is equivalent to invertibility of the equations linearization. This invertibility is implied by conditions *(i), (ii)* in Proposition 3.10. Thus, in order to prove Theorem 3.1 we must assume either:

- Hypothesis 1
- Hypothesis 2

or

- Hypothesis 1
- conditions *(i), (ii)* in Proposition 3.10

In our proof below, we use the latter.

*Proof of Theorem 3.1.* Let $\varepsilon, \nu > 0$ be small enough that they lie in the neighborhoods of 0 guaranteed by the Center Manifold Theorem and the Normal Form Lemmas of Sections 3.3 and 3.4. Now the small bounded solutions to the Swift-Hohenberg equation (1.4) are approximated by the dynamics of (3.61).

Fix $\delta > 0$ so that $\nu = \varepsilon\delta$. Assume Hypothesis 1 and conditions *(i),(ii)* from Proposition 3.10. For each $\phi \in [0, 2\pi)$, let $k(\phi;\varepsilon) = g_k(\phi;\varepsilon)$ be the wavenumber guaranteed by the Implicit Function Theorem (IFT) in the proof of Proposition 3.10. This will be smooth as a function of $\phi$. This follows from the fact that $\partial_\theta \mathcal{F} \notin \mathrm{Rg}(\mathcal{L})$, so we can apply the IFT with $\theta$ as a variable at $\theta = \phi_*$. We can repeat this at every $\phi_* \in [0, 2\pi)$, the result is a family of smooth functions $g_k^{\phi_*}$ whose domains cover $[0, 2\pi)$ and agree on their overlap.

Now let $v_{\mathrm{het}}(x; k(\phi), \phi; \delta, \varepsilon)$ be a heteroclinic solution to (3.63), also guaranteed by the IFT in the same proof. Note that $v_{\mathrm{het}} \in \mathcal{W}^{cu}_{\mathcal{P}}(\varepsilon) \cap \mathcal{W}^s(\varepsilon)$. In particular, it lies on the fiber which converges to the equilibrium $v_{\mathrm{hex}}(k(\phi), \phi; \delta, \varepsilon)$. Now undoing all the coordinate changes, transformations, and reductions will show us that $v_{\mathrm{hex}}$ corresponds to a hexagon pattern solution $u_{\mathrm{hex}}$ to the homogeneous Swift-Hohenberg equation (1.2)

with wave-vectors, at leading order in $\varepsilon$,

$$\begin{aligned}\mathbf{k}_0 &= (-1 - \varepsilon k(\phi;\varepsilon), 0)\\ \mathbf{k}_+ &= (\tfrac{1+\varepsilon k(\phi;\varepsilon)}{2}, \sqrt{3}/2)\\ \mathbf{k}_- &= (\tfrac{1+\varepsilon k(\phi;\varepsilon)}{2}, -\sqrt{3}/2).\end{aligned}$$

In particular, this solution has horizontal wavenumber $k_x(\phi;\varepsilon) = \frac{1}{2} + \frac{\varepsilon k(\phi;\varepsilon)}{2} + \mathcal{O}(\varepsilon^3)$. The vertical wavnumber $k_y = \sqrt{3}/2$ remains unchanged. The dependence on $\nu$ (or $\delta$) is implicitly built in to the formula for $k(\phi;\varepsilon)$ provided in Corollary 3.11. □

We discuss this result at the end of the next chapter, one we have computational evidence (and a best guess) for $k_1(\phi)$.

# Chapter 4

# Numerics and Simulations for Hexagons

## 4.1 Numerical Farfield-Core for Hexagons

This section provides numerical evidence to substantiate Hypotheses 1 and 2. We implement numerics for the farfield-core (FFC) decomposition described in Section 3.5.1. This theoretical framework allows us to apply "asymptotic boundary conditions" and computes a spatial heteroclinic on a large domain. This heteroclinic corresponds to a transition from hexagons to the homogeneous solution, via the spatial dynamics set up of Section 3.3.

We next outline the numerical problem. Then, the remainder of this section details our numerical evidence for the hypotheses and documents convergence of the scheme.

### 4.1.1 Numerical Scheme

We solve a numerical version of equation (3.66), the functional equation of the theoretical FFC framework. We remind the reader that this equation is obtained by truncating the normal form and applying additional ansatz – co-rotation $\mathcal{R}_{xk}$ and farfield-core decomposition $v = \chi v_{\text{hex}} - w$. We rewrite the equation here as

$$\mathcal{F}(w, k, \theta; \varepsilon) = \partial_x w - f(x, w, k, \theta; \varepsilon, \delta) = 0, \qquad w \in (H^2_\eta)^4, \qquad x \in \mathbb{R}. \tag{4.1}$$

Here $f$ is the right-hand side of equation (3.65), $\partial_x$ is the first spatial derivative, $k$ and $\theta$ are the wavenumber and phase of the asymptotic pattern, $\varepsilon$ is the size of the (small) jump inhomogeneity on the linear term, and $\delta$ is the parameter on the quadratic terms. We will treat $k$ as a variable and $\theta, \varepsilon, \delta$ as parameters in our numerics.

First we truncate the domain and discretize space. We fix positive $L_x \gg 1$ and pose the problem on the interval $[-L_x, L_x]$. This causes a major issue with enforcing exponential localization of our solution $w$, since our exponentially weighted norm $\|\cdot\|_\eta$ becomes equivalent to an unweighted version on the finite domain. We resolve this issue with a phase condition at the end of the section. Proceeding with our discretization, we let the grid size be $dx$ and obtain a total of $n = 2L_x/\mathrm{d}x + 1$ spatial grid points. Let $x_j$ be the $j$th grid point. Recalling that this is a functional equation with four components

$$w = \begin{bmatrix} w^0 \\ v^0 \\ w^+ \\ v^+ \end{bmatrix}, \qquad f = \begin{bmatrix} f^1 \\ f^2 \\ f^3 \\ f^4 \end{bmatrix},$$

we define

$$w_j := w(x_j) \in \mathbb{C}^4, \qquad f_j(k, \theta; \varepsilon, \delta) = f(x_j, w_j, k, \theta; \varepsilon, \delta) \in \mathbb{C}^4$$

We implement a second order finite difference approximation for the derivative

$$\partial_x u - f(u) \approx \frac{u(x_{j+1}) - u(x_j)}{dx} - \frac{f(u(x_{j+1})) + f(u(x_j))}{2}$$

as in [16, §8.4.1], for instance. To this end, define the $(n-1) \times n$ matrix

$$D = \begin{bmatrix} -1 & 1 & 0 & \dots & 0 \\ 0 & -1 & 1 & 0 & \dots \\ \vdots & & \ddots & \ddots & \vdots \\ 0 & 0 & 0 & -1 & 1 \end{bmatrix}.$$

Including boundary conditions,

$$w^0(-L_x) = w^0(L_x) = w^+(-L_x) = w^+(L_x) = 0,$$

by appending four rows to the bottom makes the problem square. Define

$$BC = \begin{bmatrix} 1 & 0 & \dots & 0 \\ 0 & \dots & 0 & 1 \end{bmatrix}.$$

We can now write the finite-difference version of (4.1) as a system of $n$ equations

$$\left[\begin{array}{cccc} D & 0 & 0 & 0 \\ 0 & D & 0 & 0 \\ 0 & 0 & D & 0 \\ 0 & 0 & 0 & D \\ \hline BC & 0 & 0 & 0 \\ 0 & 0 & BC & 0 \end{array}\right] [w_j] - \left[\begin{array}{c} (f^1_{j+1} + f^1_j)/2 \\ (f^2_{j+1} + f^2_j)/2 \\ (f^3_{j+1} + f^3_j)/2 \\ (f^4_{j+1} + f^4_j)/2 \\ \hline 0 \\ 0 \\ 0 \\ 0 \end{array}\right] = 0, \tag{4.2}$$

with parameters $k, \theta, \varepsilon$, and $\delta$ appearing in the $f^i_j$ terms.

The function $f$ has an additional parameter built in. We have not yet fixed the location of the cutoff function $\chi(x)$, from the farfield-core ansatz. Section 3.5.1 only required that this location be $\ll -1$. We let $-\ell$ be the center of this cutoff function by defining $\chi(x_j) := \frac{1-\tanh(x_j+\ell)}{2}$. We choose $\ell$ to be $\sim L_x/2$.

Recall that we wish to solve for $(w, k)$ in terms of parameters $\theta, \varepsilon, \delta$. Treating $k$ as a variable requires appending an equation. Note that fixing $\phi$ does not eliminate translation invariance on a finite domain, because we cannot effectively enforce exponential localization of $w$. We must therefore add a condition that eliminates linear growth of $w$ near $x \sim -L_x$. In our 4-dimensional phase space, this contribution comes from the direction of the rotation $\mathcal{R}_\theta$, since translation of $x$ moves us along the co-rotating frame

$\mathcal{R}_{kx}$. We choose the phase condition

$$\int_{-L_x}^{-L_x+3} w(x) \cdot \partial_\theta \mathcal{R}_\theta v_{\text{hex}}(k, \theta; \varepsilon)\, \mathrm{d}x = 0. \tag{4.3}$$

We note that many other choices for this phase condition may work equally well. In particular, we originally used a different choice which appeared to work except for a set of $\phi$ values with measure zero.

In the discretized problem, this phase condition amounts to appending a row $PC$. To build this row, we first make the $n \times 1$ vector

$$PC = \partial_\theta \mathcal{R}_\theta v_{\text{hex}}(k, \theta; \varepsilon) \begin{bmatrix} 1 & \dots & 1 & 0 & \dots 0 \end{bmatrix}$$

where there are $3/dx$ ones before the zeros. Then the new bottom row is four copies of $PC$, concatenated horizontally. Appending this row to (4.2) and concatenating an extra column of zeros, we have

$$F(w_j, k; \phi, \varepsilon, \delta) := \left[\begin{array}{cccc:c} D & 0 & 0 & 0 & 0 \\ 0 & D & 0 & 0 & 0 \\ 0 & 0 & D & 0 & 0 \\ 0 & 0 & 0 & D & 0 \\ \hdashline BC & 0 & 0 & 0 & 0 \\ 0 & 0 & BC & 0 & 0 \\ \hdashline PC & PC & PC & PC & 0 \end{array}\right] \begin{bmatrix} w_j^0 \\ v_j^0 \\ w_j^+ \\ v_j^+ \\ \hdashline 0 \end{bmatrix} - \left[\begin{array}{c} (f_{j+1}^1 + f_j^1)/2 \\ (f_{j+1}^2 + f_j^2)/2 \\ (f_{j+1}^3 + f_j^3)/2 \\ (f_{j+1}^4 + f_j^4)/2 \\ \hdashline 0 \\ 0 \\ 0 \\ 0 \\ \hdashline 0 \end{array}\right] = 0. \tag{4.4}$$

Now (4.4) represents a well-posed problem with three parameters $\phi, \varepsilon, \delta$, and three numerical constructs $L_x$ (domain size), $dx$ (grid size), $\ell$ (location of cut off). We solve this problem with an application of Newton's method[1]. For an initial guess, we use a

[1]Specifically, we employ MATLAB's powerful `fsolve` function. In practice, this introduces added complexity upon implementation, since `fsolve` finds real solutions only. In practice our system becomes $8n + 1 \times 8n + 1$, accounting for real and imaginary parts.

piecewise constant function

$$w_{\text{init}}(x_j) = \begin{cases} 0 & x_j < -\ell, x_j > 0 \\ v_{\text{hex}}(\phi;\varepsilon,\delta) & -\ell < x_j < 0 \end{cases} \qquad \text{and} \qquad k_{\text{init}} = \tfrac{\varepsilon}{8}\cos(\phi).$$

We find that Newton's method converges quickly for all $\sqrt{3}/4 < \delta \lessapprox 4.1$, for all $0 < \varepsilon \lessapprox 0.27$, and for all $\phi \in [0, 2\pi)$. For $\varepsilon, \phi$, we sometimes must use an initial guess of a solution for nearby values. We discuss the bounds on $\delta$ in the next section. The upper bound on $\varepsilon$ is due to the fact that the terms $\varepsilon T(\cdot, e^{\mathrm{i}x})$ in (3.65), from the normal form transformations, disrupt the hyperbolicity of $v \equiv 0$ as $\varepsilon \to 0.3$. In the next sections, we document solutions to this problem, for various values of $\phi, \varepsilon, \delta$, that support the claims of Hypotheses 1 and 2. We demonstrate exponential convergence of the solutions in the size of the domain $L_x$, quadratic convergence in the size of the grid $dx$, and independence of solutions with respect to the location $-\ell$ of the cutoff function $\chi$.

Unless otherwise stated, images and results were generated with $L_x = 50, \mathrm{d}x = 0.25, \ell = 20$. With these settings, computations occurred with $n = 401$ spatial grid points. Note that the location $-\ell$ of the cutoff function is approximately in the middle of the negative-half of the domain.

### 4.1.2 A Real Heteroclinic

This section provides numerical evidence to support the assertions in Hypothesis 1. By setting $\varepsilon = 0$, we reduce the problem to one described by the amplitude equations (3.2). Setting $\phi = 0$ restricts us to the real subspace $\{w \in \mathbb{R}^4\}$. Our numerical problem reduces to a real boundary-value problem, where the variable $k \equiv 0$.

Figure 4.1 shows the heteroclinic profiles $c_0, c_+$ and the core solution profiles $w_0, w_+$ for $\delta = 0.25, 1, 3, 4.1$. Notice that all profiles are completely real; the imaginary part (red) is zero on the whole domain. Notice that the heteroclinic profiles $c_+$ are nonmonotone – easily visible for smaller values of $\delta$. This suggests that proving existence with basic methods, such as invariant regions or sub/super solutions, would be difficult.

Finally, we point out that for $\delta = 0.45$ and 4.1 we begin to see qualitative changes in the profile beginning to show. For $\delta = 0.45$, we see the the bump before the transition become exaggerated in $c_+, w_+$ and we see a negative dip creep in before the first

transition in for $w_0$. This can be attributed to the impending loss of hyperbolicity for the hexagonal equilibrium $\mathbf{c}_{\text{hex}}$ in the amplitude equations, recall that this occurs at $\delta = \sqrt{3}/4 \approx 0.4330$. For $\delta = 4.1$, we see the transition begin to show an intermediate bump. We expect this is due to a second equilibrium $\mathbf{c}_{\text{dnhex}}$ moving into the stable manifold of $\mathbf{c}_0$. Indeed, for these extremal values of $\delta$, the Newton's method took longer to converge. In the remainder, we use intermediate values, typically $\delta = 1, 3$.

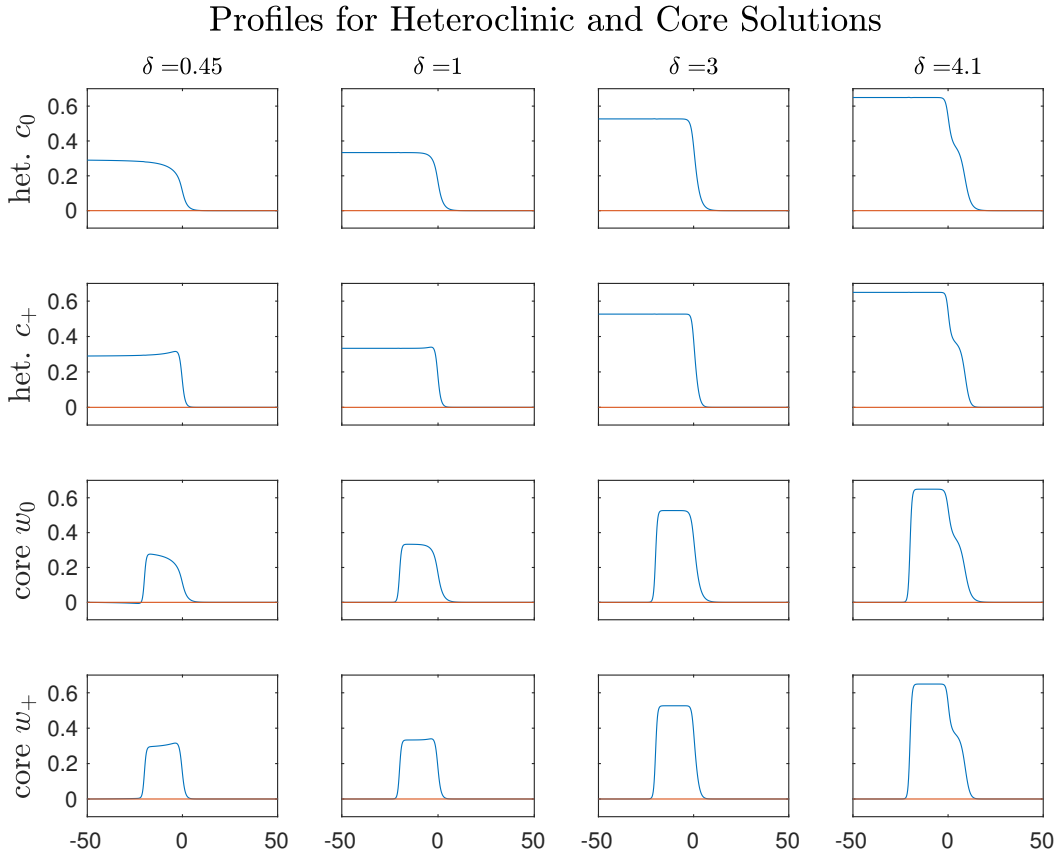


Figure 4.1: Profiles for real heteroclinics $c_0, c_+$ and core solutions $w_0, w_+$ to the numeric problem (4.4), with $\varepsilon = \phi = 0$ and $\delta = 0.45, 1, 3, 4.1$. Each plot shows the real part (blue) and imaginary part (red). Heteroclinic profiles are generated from the core solutions by undoing the farfield-core ansatz in post-processing. Each plot is shown in a window $[-50, 50] \times [-0.1, 0.7]$.

**Convergence**

We document convergence of solutions with respect to the size of the domain $L_x$, and grid size $dx$ in Figure 4.2. In addition we demonstrate independence of the location $-\ell$ of the cutoff function $\chi$ from the farfield-core ansatz. For each, we define error as the norm in $(\ell^2)^4$ of the difference $w - w_{\text{ref}}$, where we compute $w_{\text{ref}}$ with $L_x = 75, \mathrm{d}x = 0.1, \ell = 20$. In each case, taking this difference poses small issues, which we address below.

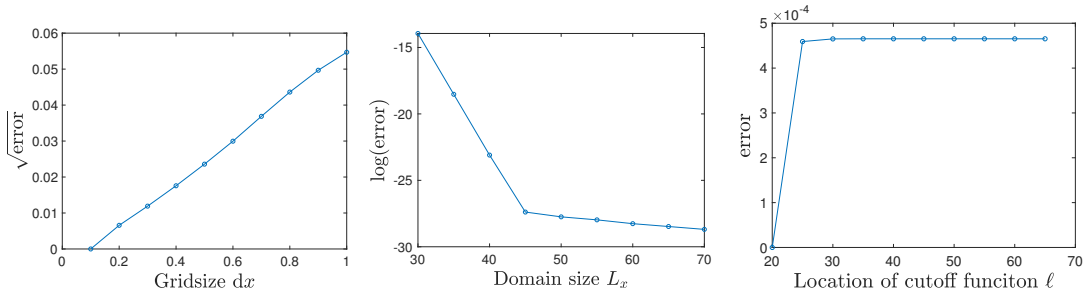


Figure 4.2: Convergence of the real heteroclinic profiles for $\varepsilon = 0, \phi = 0, \delta = 1$, and (a) $L_x = 75, \ell = 20$, varying grid size d$x$; (b) $\ell = 20, \mathrm{d}x = 0.1$, varying domain size $L_x$; and (c) $L_x = 75, \mathrm{d}x = 0.1$ varying cutoff function location $\ell$. Error is defined as the norm in $(\ell^2)^4$ of the difference $w - w_{\text{ref}}$, where $w_{\text{ref}}$ is computed with $L_x = 75, \mathrm{d}x = 0.1, \ell = 20$. Additional details in text.

Figure 4.2a demonstrates that the error $\sim \mathcal{O}(dx^2)$, as expected from our second-order finite difference scheme. In order to compare $w$ and $w_{\text{ref}}$ computed with different $dx$ values, we downsampled $w_{\text{ref}}$ by choosing only the values at grid points which appear in $w$. To ease this downsampling, we chose values of $dx$ that are integral multiples of the reference grid size $\mathrm{d}x = 0.1$.

Figure 4.2b demonstrates that the error $\sim e^{-L_x}$, as expected due to the fact that our solutions lie in stable/unstable manifolds. Here we truncate each $w$ to the smallest domain with $L_x = 30$ and compare the truncated version to a similarly truncated $w_{\text{ref}}$. We point out the the piecewise nature of the log(error) plot. The piecewise nature of the log-plot is likely due to the fact that, for $L_x \gtrapprox 45$, the error from the grid size dominates the error from the domain size.

Figure 4.2c demonstrates that the solutions are essentially independent of the location of the cutoff function. Clearly the core solutions $w$ and $w_{\text{ref}}$ with different cut-off

locations $\ell$ would not have comparable norms in $(\ell^2)^4$, since they are localized on different parts of the domain. Instead, we compare the corresponding heteroclinic profiles $v$ and $v_{\text{ref}}$ and observe that the error is $\sim 10^{-4}$.

### 4.1.3 Complex Heteroclinics

This section provides numerical evidence corroborating the conclusions of Proposition 3.4. That is, in the full complex phase space of (3.2), the unstable and stable manifolds intersect in a circle, obtained by rotating the intersection of Hypothesis 1. This leads to a family of heteroclinics, each obtained by rotating the real heteroclinic of the last section. To explore these numerically, we keep $\varepsilon = 0$, but allow $\phi$ to vary in $[0, 2\pi)$. As expected, each of the solutions in this section still have $k \approx 0$.

Figure 4.3 shows the heteroclinic profiles $c_0, c_+$ and the core solution profiles $w_0, w_+$ for $\delta = 1, 3$ and $\phi = \pi/3, 5\pi/4$. As expected, these are precisely rotated versions of the real heteroclinics in the last section. For this reason, we omit a redundant convergence check.

Notably, this is the first, and simplest, case where we can compute a strain-displacement relation. In this case it is completely vertical, up to numerical error. See Figure 4.6 and Section 4.1.5.

### 4.1.4 Persistence of Heteroclinics with $\varepsilon > 0$

This section provides numerical evidence supporting the claims of Hypothesis 2. With $\varepsilon > 0$, our numerical problem (4.4) is analogous to looking for heteroclinics in the truncated normal form equation including terms moved via the normal form commutator, see equation (3.61). For each $0 < \varepsilon < 0.27$, Newton's method converges to a core solution $w$ and wavenumber $k$.

Figure 4.4 shows the heteroclinic profiles $c_0, c_+$ and the core solution profiles $w_0, w_+$ for $\delta = 1$, $\phi = 0, \pi/3$, and $\varepsilon = 0.05, 0.1, 0.2$. Notice that the profiles are similar to the real profiles for small $\varepsilon$ but as $\varepsilon$ grows we see a genuine difference. A small bump emerges just before the transition in the imaginary part (red) as $\varepsilon$ grows. This illustrates that these are no longer simple rotations of the real heteroclinic, in contrast to the ones we observed in the last section. For instance, one may compare the rotated right-hand

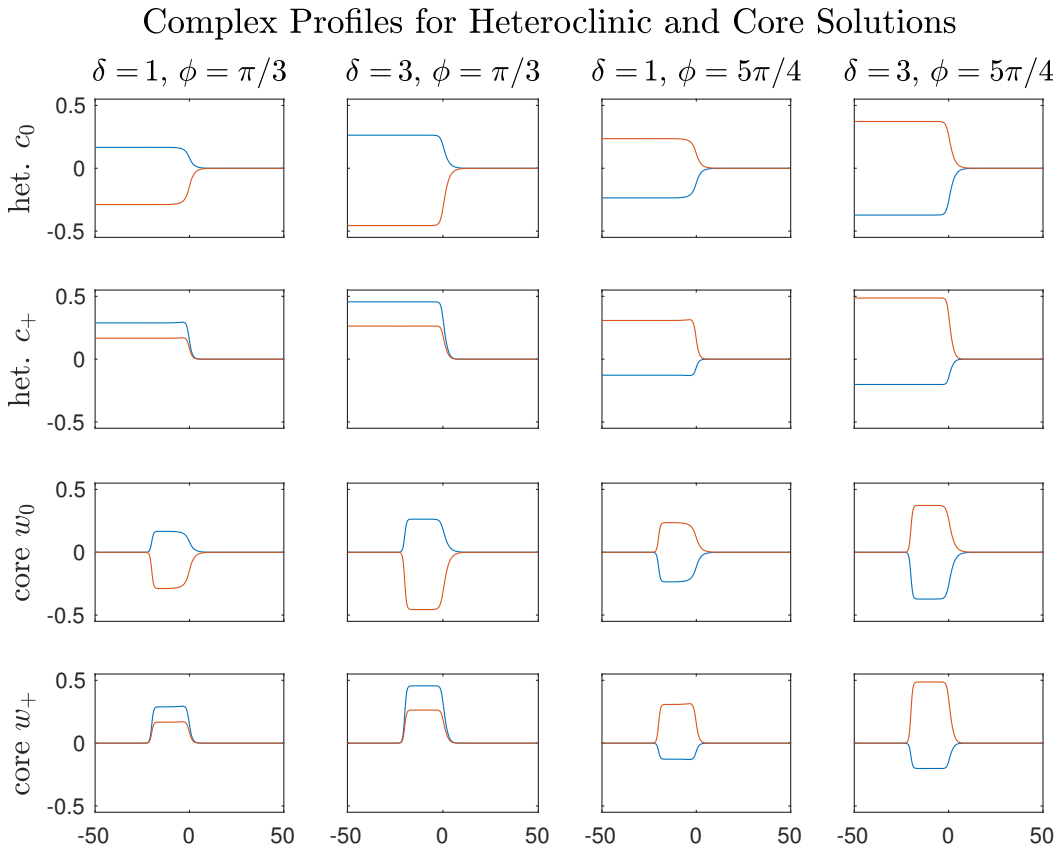


Figure 4.3: Profiles for complex heteroclinics $c_0, c_+$ and core solutions $w_0, w_+$ to the numeric problem (4.4), with $\varepsilon = 0$, $\phi = \pi/3, 5\pi/4$, and $\delta = 1, 3$. They appear identical to the real solutions with a complex rotation by $\mathcal{R}_\phi$. Each returned a value of $k < 1.5 \times 10^{-7}$.Each plot is shown in a window $[-50, 50] \times [-0.55, 0.55]$.

column (with $\varepsilon = 0.2, \phi = \pi/3$) to the left-hand column in Figure 4.3. Both these profiles are generated with $\phi = \pi/3$ and appear to have the same phase except near the transition, where we point out the small bump in the solution with $\varepsilon > 0$.

We are now able to compute non-trivial strain-displacement relations. See Figure 4.7 and Section 4.1.5.

### Convergence

Now that $\varepsilon > 0$, we are implementing the full vector field and should reexamine convergence. We conduct a study similar to that of Section 4.1.2. For our test case we choose

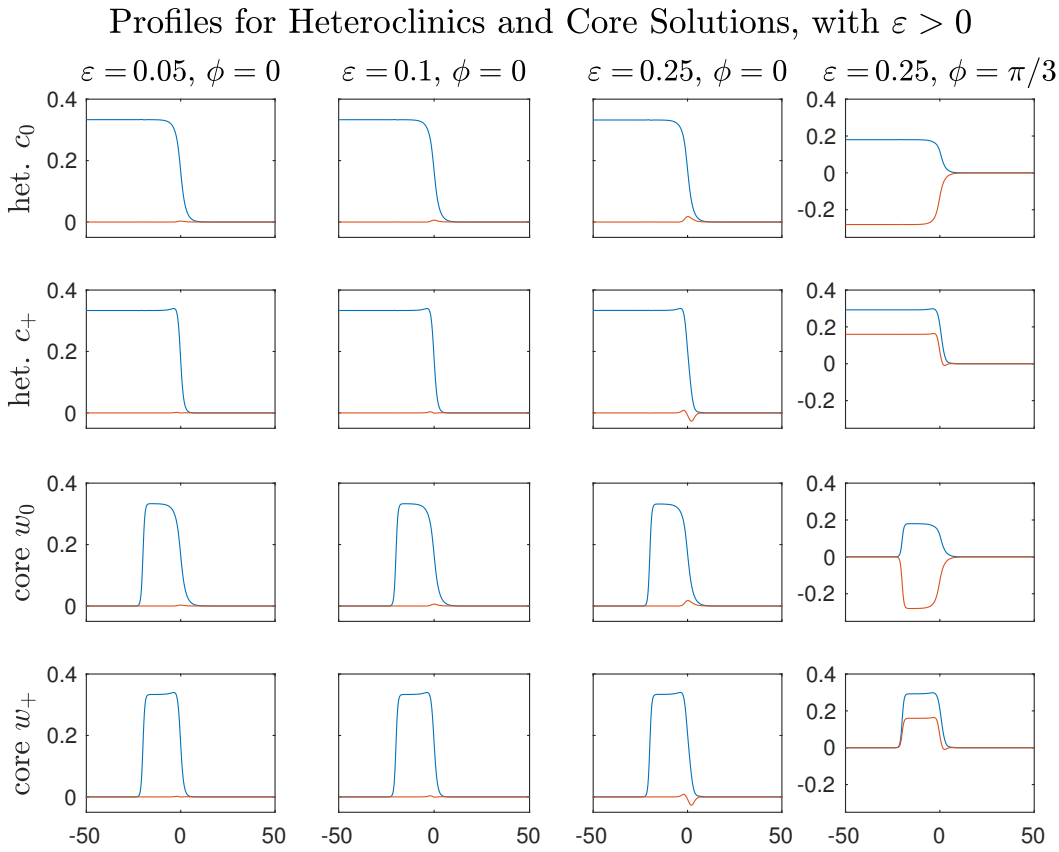


Figure 4.4: Profiles for heteroclinics $c_0, c_+$ and core solutions $w_0, w_+$ to the numeric problem (4.4), with $\delta = 1, \phi = 0, \pi/3$, and $\varepsilon = 0.05, 0.1, 0.25$.

$\varepsilon = 0.1$ and $\phi = \pi/3$ (the latter is particularly immaterial). We find that the error $\sim \mathcal{O}(dx^2)$, $\sim e^{-L_x}$, and that moving the location of the cutoff function has essentially no effect. See Figure 4.5 for details.

In addition, we also study the convergence of the wavenumbers, since these are no longer zero. We define the wavenumber error $k_{\text{err}} := k - k_{\text{ref}}$, where $k_{\text{ref}}$ is the wavenumber of the reference function $w_{\text{ref}}$ and $k$ is the wavenumber of solutions varying with the grid size, domain size, or cutoff location.

Having exhibited convergence of our algorithm, we now turn to our ultimate goal of computing the strain-displacement relations.

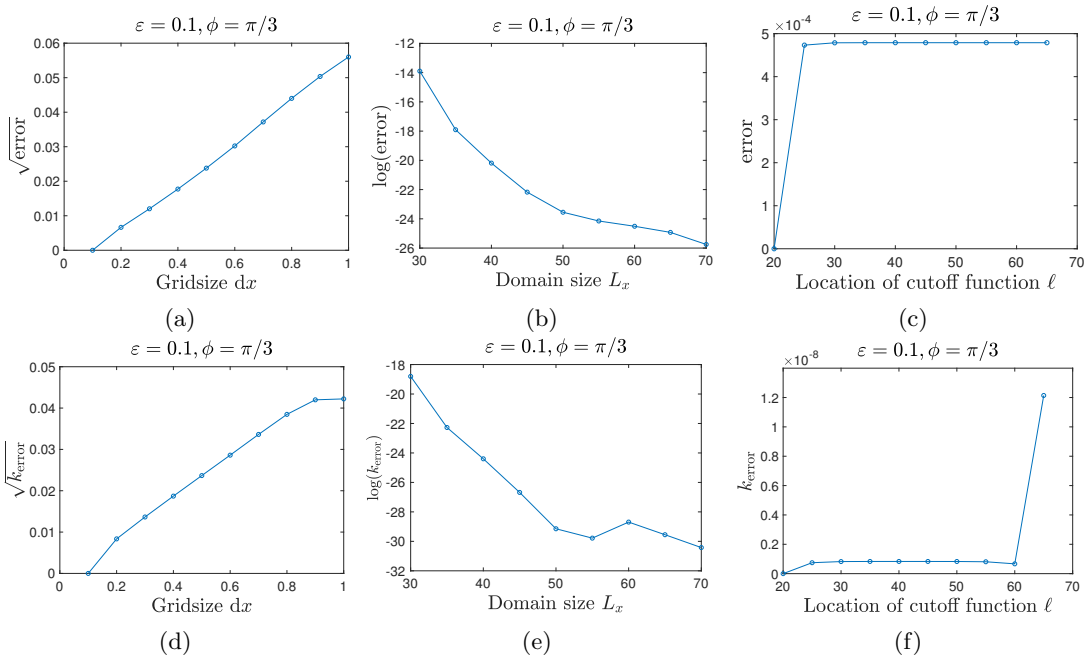


Figure 4.5: Convergence of the complex heteroclinic profiles and wavenumbers for $\varepsilon = 0.1, \phi = \pi/3, \delta = 1$, and (a) $L_x = 75, \ell = 20$, varying grid size $dx$; (b) $\ell = 20, \mathrm{d}x = 0.1$, varying domain size $L_x$; and (c) $L_x = 75, \mathrm{d}x = 0.1$ varying cutoff function location $\ell$. Error is defined as the norm in $(\ell^2)^4$ of the difference $w - w_{\text{ref}}$ and $k_{\text{error}}$ is defined as the absolute difference $|k - k_{\text{ref}}|$, where $w_{\text{ref}}, k_{\text{ref}}$ are computed with $L_x = 75, \mathrm{d}x = 0.1, \ell = 20$. Additional details in text.

### 4.1.5 Computing Strain-Displacement Relations

Recall that a strain-displacement relation is an equation relating the wavenumber and phase of a pattern. Generically, the SH equation in an infinite domain, and with spatially-constant parameter, has periodic patterns with wavenumbers independent of their phase at zero, say. By introducing our parameter jump inhomogeneity, we have disrupted the translation invariance and fixed such a relation. In terms of spatial dynamics, recall that the stable manifold of $\mathbf{c}_0$ intersects the unstable manifold of periodic orbits $\mathcal{P}(\varepsilon)$ in a circle $\mathcal{S}(\varepsilon)$. Each point on $\mathcal{S}(\varepsilon)$ connects $\mathbf{c}_0$ to a fiber of a particular periodic orbit, with particular wavenumber $k$ and phase $\phi$.

Numerically, we implement numerical continuation in the $k, \phi$-plane, using a secant step method. The results appear in Figure 4.7.

In the case of $\varepsilon = 0$, the completely vertical strain-displacement relation of Figure

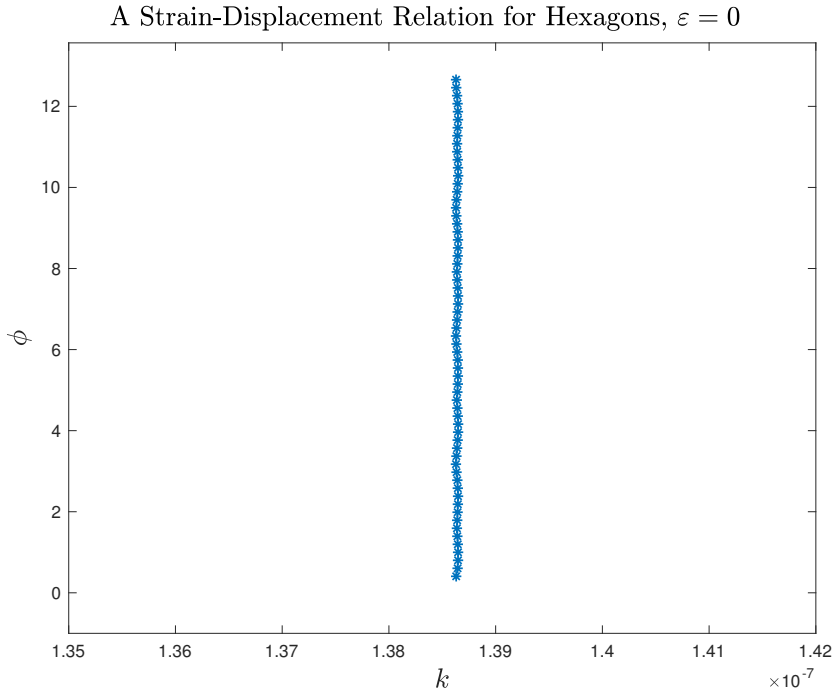


Figure 4.6: A vertical strain-displacement relation for complex solutions with $\varepsilon = 0, \delta = 1$, and $\phi \in [0, 2\pi)$. Note that the horizontal scale $\sim 10^{-7}$.

4.6 implies that $k = 0$ for all $\phi \in [0, 2\pi)$. This scenario corresponds to Proposition 3.4. In terms of the spatial dynamics, the whole circle $\mathcal{S} = \mathcal{S}(0)$ connects to fibers ending on periodic orbits with $k = 0$, i.e. equilibria $\mathbf{c}_{\text{hex}}(\phi)$.

When $\varepsilon > 0$, the strain-displacement relation wiggles slightly as observed in Figure 4.6. In terms of the spatial dynamics, the circle of intersection $\mathcal{S}(\varepsilon)$ deforms only slightly because it is transverse, rather than disconnecting or disappearing as a non-transverse intersection might. The effect is that $\mathcal{S}(\varepsilon)$ selects slightly different fibers and thus lands on periodic orbits with nonzero $k$, dependent on their phase $\phi$. In the FFC interpretation, this is equivalent to the invertibility of $\partial_{(w,k)}\mathcal{F}$ in Proposition 3.10. One then applies the Implicit Function Theorem and arrives at the Melnikov-type integral mentioned at the end of Section 3.5. It would be interesting to compare this explicit computation to the results of the numerical studies here. The main obstacle is the lack of an explicit heteroclinic solution, even in the real subspace. Instead, we make the best guess we can based on our numerics. By inspection we observe that appears $k \sim \cos(\phi)$.

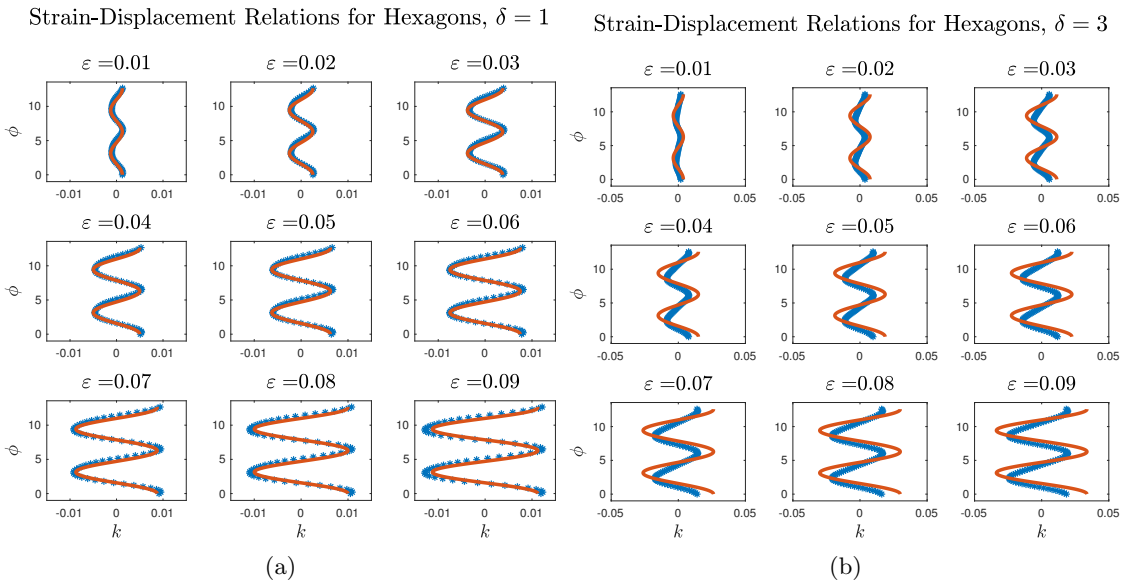


Figure 4.7: Strain-displacement relations computed for $\phi \in [0, 4\pi)$, various $\varepsilon \in [0, 0.1]$, and (a) $\delta = 1$, (b) $\delta = 2$. Solutions to the numerical farfield-core problem (blue $*$) and our best guess $k = \delta\varepsilon\cos(\phi)$ (orange).

Taking the maximum and minimum wavenumber from strain-displacement relations for $\varepsilon = 0.01, \ldots, 0.27$ and plotting in the $\varepsilon - k$ plane, we obtain Figure 4.8a. We clearly see a linear relationship for small $\varepsilon$, as in the case of stripes. We note that a line with slope 8 is an excellent fit and extrapolate a guess for the first order term in a strain-displacement expansion

$$k(\phi; \varepsilon) \sim \frac{\varepsilon}{8}\cos(\phi), \qquad \text{when } \delta = 1.$$

This guess may provide guidance in future analysis along the lines of that described above.

For $\delta = 3$, we compute the strain-displacement relations appearing in Figure 4.7b with minima and maxima documented in Figure 4.8b. Initial inspection does not yield a guess that fits satisfactorily. Notably, the large change in $\delta$ has effected a large change in the relation above. This should come as no surprise, since the Melnikov-type integral includes the linearization $\partial_{(w,k)}\mathcal{F}$ at a heteroclinic, which clearly depends on $\delta$ as demonstrated in Figure 4.1.

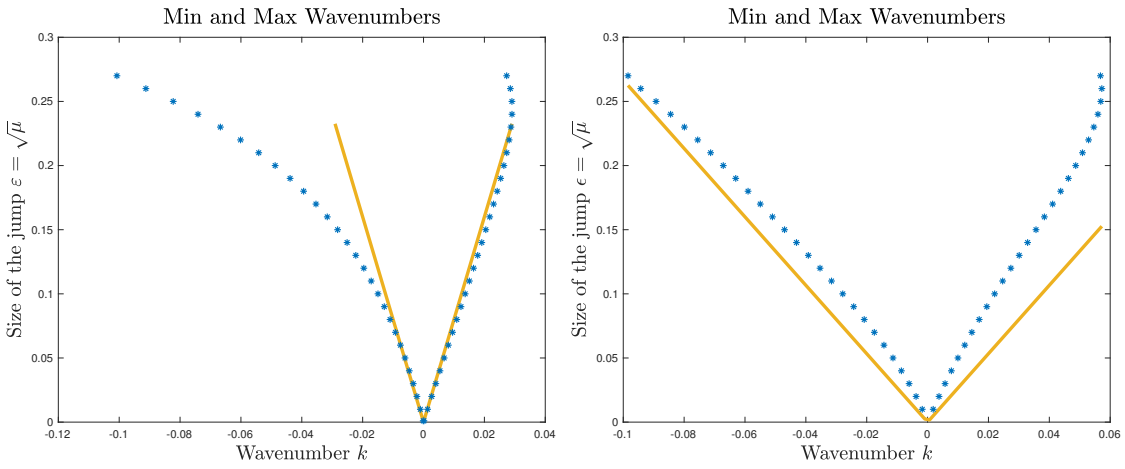


Figure 4.8: Minimum and maximum wavenumber, obtained from strain-displacement relations computed with (a) $\delta = 1$, (b) $\delta = 3$ using secant continuation and our best guess $k_{\min/\max} = \pm\delta\varepsilon/8$ (gold).

## 4.2 Direct Simulations

We observed the existence of stationary hexagonal fronts for long times in a direct numerical simulation of the Swift-Hohenberg equation with spatial inhomogeneity (1.4). We used a standard spectral method with $2^{10} \times 2^8$ Fourier modes, creating an effective $\mathrm{d}x \approx 0.3927$ and $\mathrm{d}y \approx 0.2267$. We used implicit Euler time stepping with $\mathrm{d}t = 0.5$. In independent trails not reported here, refinements of these numerical constructs yielded no qualitative change. All simulations are posed on a long, narrow strip with dimension $[-64\pi, 65\pi] \times [-\frac{16\pi}{\sqrt{3}}, \frac{16\pi}{\sqrt{3}}]$ with periodic boundary conditions. We use various $\varepsilon > 0$ and for the quadratic parameter we use $\nu = \varepsilon$ (i.e. $\delta = 1$). We use initial data of the form

$$u(x,y,0) = \begin{cases} \frac{2}{3}\varepsilon\Big[\cos(-(x+\phi_0)) + \cos\left(\frac{x-\phi_0}{2} + \frac{\sqrt{3}y}{2}\right) + \cos\left(\frac{x-\phi_0}{2} - \frac{\sqrt{3}y}{2}\right)\Big], & x < 0 \\ 0, & x > 0 \end{cases}$$

which, on the left, represents the leading order real expression for a hexagonal pattern with critical wavenumber $k_x = \frac{1}{2}$. We shift the pattern to the right by $\phi_0 = \pi$ so that it does not have a maximum at $x = 0$.

### 4.2.1 Unique Wavenumber Selection in Growing Domains

As discussed in Section 2.6.3, the system might exhibit any wavenumber $k_x$ in an interval $J_{k_x}$. We would like to measure the bounds of $J_{k_x}$, and in order to do so we employ the theory of [25]. There, authors examined several model equations similar to ours, but with a moving inhomogeneity $\mu(x-ct)$ (or on a linearly growing domain with boundary conditions). They found that

$$k_x(c) = k_{\min} + \mathcal{O}(\sqrt{c})$$

where $k_{\min}$ is the left endpoint of $J_{k_x}$. That is, it is the minimum horizontal wavenumber occurring in the same system with a fixed inhomogeneity.

Figure 4.9 shows the results of numerical simulations with a moving inhomogeneity $\mu(x-ct)$ with speed $c = 0.0001$. The behavior we observed is similar to the heuristic we gave in Section 1.2.3 to help understand the relationship between strain (compression of stripes) and displacement (phase). Here, the inhomogeneity moves slowly to the right. As it does so, the domain where we observe hexagons grows larger. The hexagons widen to fill the space, decreasing the wavenumber.[2] When the wavenumber attains (close to) the minimum, a new column of hexagons is added on the right to fill the space and the whole pattern relaxes to a more comfortable wavenumber near the critical $k_x = \frac{1}{2}$.

*Remark* 4.1. The skeptical reader may note that for faster speeds, there is enough space to add a full column of hexagons before the bulk of the pattern obtains the minimum wavenumber. Indeed, this is born out in the order $\mathcal{O}(\sqrt{c})$ terms in the formula above, see [25] for details. The key is that we have chosen a speed so small that the wavenumber in the bulk of the pattern can adjust down to the minimum before there is enough space for a full new column of hexagons to form. To ensure we chose a sufficiently small speed, we conducted numerical experiments with decreasing speed until we could no longer observe a decrease in wavenumber.

We measured wavenumbers throughout each simulation and plotted them over time, observing oscillations described well by the behavior outlined above. See the bottom

[2] Furthermore, it appears that the phase of the pattern at the inhomogeneity is somewhat fixed – because the solution must decay to 0 quickly thereafter. Meanwhile, the phase in the bulk of the hexagons changes as they all expand to fill the space to the right.

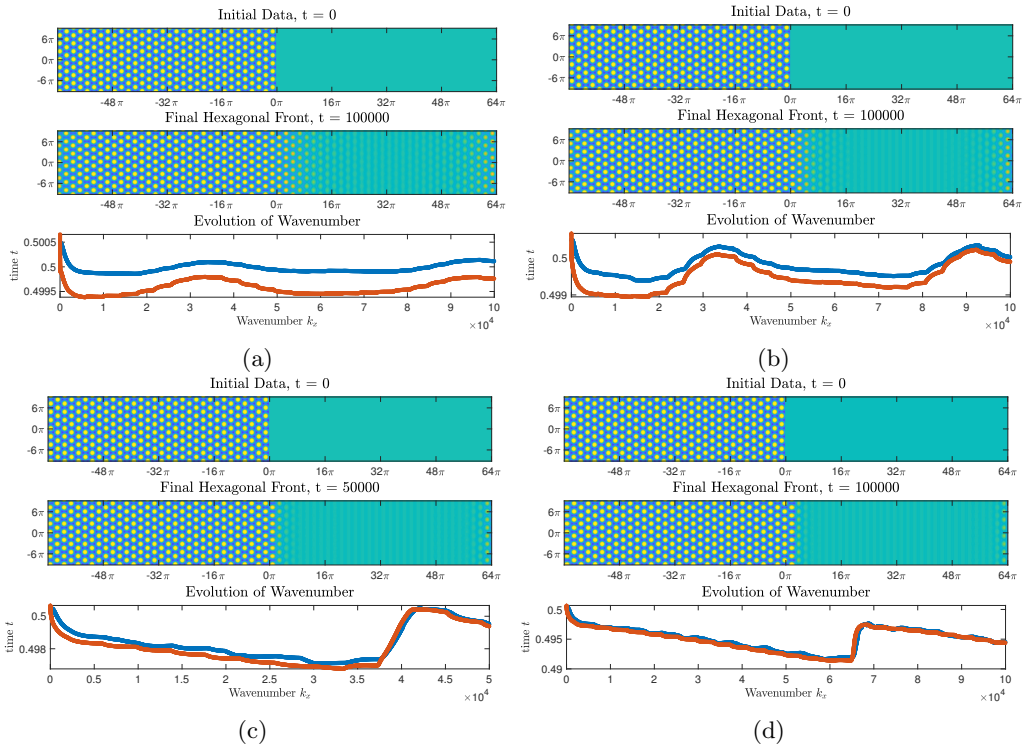


Figure 4.9: Direct numerical simulations of the Swift-Hohenberg equation with spatial inhomogeneity 1.4 with $\delta = 1$ and (a) $\varepsilon = 0.05$, (b) $\varepsilon = 0.1$, (c) $\varepsilon = 0.2$, and (c) $\varepsilon = 0.3$. Each subfigure shows initial condition (top), final result of long simulation (middle), and wavenumbers throughout the simulation (bottom). We plot the wavenumber in the middle of the patterns (blue) and the average wavenumber throughout the bulk (orange).

plot in each subfigure of Figure 4.9. Note that for small $\varepsilon$, e.g. (a) $\varepsilon = 0.05$, we see a very gradual change in wavenumbers as hexagons expand and are added slowly. Observing that the transition from hexagons to the zero state is quite gradual and it can be hard to identify the position of the inhomogeneity in the final frame. This is simply because the size of the inhomogeneity is not drastic. Correspondingly, it does not restrict the possible phases at $x = 0$ so harshly and allowing the wavenumbers to transition slowly. By contrast, larger values of $\varepsilon$, e.g (d) $\varepsilon = 0.3$, display a sharper transition and clearly show the time at which a column of hexagons was added by a steep increase in the wavenumber $k_x$.

### 4.2.2 Comparing Measurements and Farfield-Core

By taking the minimum wavenumber obtained by the middle of the hexagons in each of our simulations, we can compare to the data collected from numerical solutions of the far-field core problem and recorded in Figure 4.8. To do so, we must transform the FFC data by undoing all the transformations used to arrive at the amplitude equations. While the numerical FFC data provided us with wavenumber $k$ for solutions to the amplitude equations, we are now comparing that with a wavenumber $k_x = \frac{1}{2} + \frac{\varepsilon k}{2}$. See the proof in Section 3.6 for details. Figure 4.10 shows excellent agreement between the transformed far-field core data (blue $*$) and the measurements from direct numerical simulations (orange $\circ$), particularly for small $\mu = \varepsilon^2$. Note that we again plot our best guess $k_{x,\min} = \frac{1}{2} - \frac{\varepsilon^2}{16}$ (gold) and see strong agreement with our measurements from simulations, even for values of $\varepsilon^2$ past where the far-field core data has diverged.

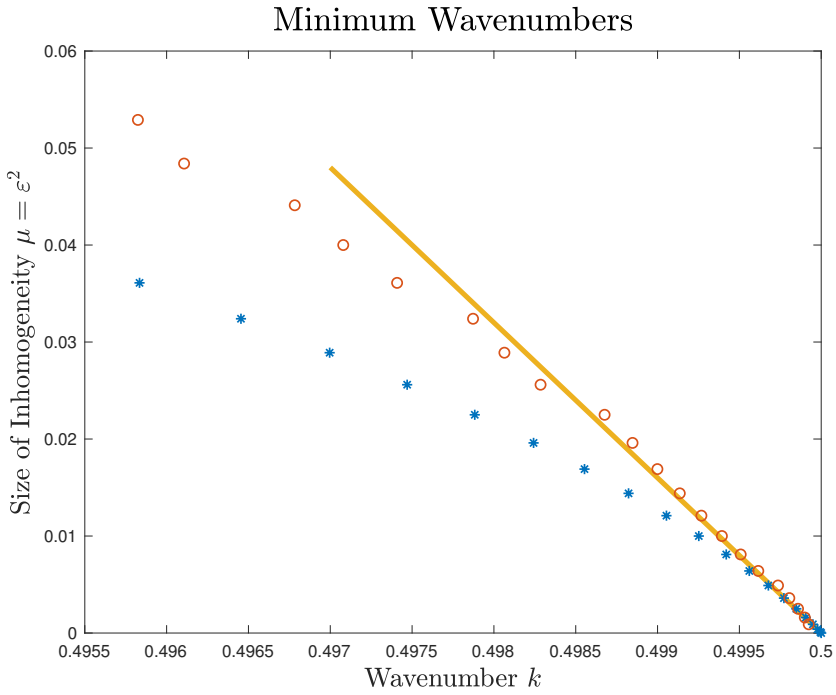


Figure 4.10: Minimum wavenumbers for $\delta = 1$ as computed obtained from numerical far-field core (blue $*$) and measurements in direct simulations (orange $\circ$) and our best guess $k_{x,\min} = \frac{1}{2} - \frac{\varepsilon^2}{16}$ (gold).

## 4.3 Conclusions and Discussion

### Parameter Ramps and Boundary Conditions

As in the case of stripes, there are obvious analogies to be drawn between our case and the Swift-Hohenberg posed on a semi-infinite domain with a boundary condition at $x = 0$. Ideas discussed at the end of Chapter 2, such as investigating a family of increasingly large jumps, are similarly interesting in the hexagon case. However, one would likely benefit from understanding them in the simpler case of stripes first.

Also, one could again imagine smoothing out the jump to the point where it becomes a slow ramp. Unlike in the case of stripes, there has been very little work in this direction. The only such investigation known to us is in the case of the amplitude equations only [35]. There Hoyle demonstrates existence of hexagons on a (fairly steep) ramp of the form $\tanh 10x$. She does not examine wavenumber selection, but remarks that previous results about rolls on parameter ramps suggest that it should occur at order $\mathcal{O}(\varepsilon^2)$ as we have shown here.

### Similarities to Striped Fronts

Supposing that we fix $\delta = 1$, we have a guess and numerical evidence that

$$\tfrac{1}{2} - \tfrac{\varepsilon^2}{16} \leq k_x \leq \tfrac{1}{2} + \tfrac{\varepsilon^2}{16}.$$

Compared with the case of striped fronts, where $1 - \frac{\varepsilon^2}{16} \leq k_x \leq 1 + \frac{\varepsilon^2}{16}$, the bounds on the interval of wavenumbers appear to be the same in each case. This suggests that we have a new heuristic – think of columns of hexagons as equivalent to stripes and imagine that the same strain-displacement phenomenon is at play in both situations.

This has the interesting effect that *only* the horizontal wavenumber has been selected. Indeed, the analysis presented hear suggests that the vertical wavenumber remains unrestricted from the homogeneous parameter case. This helps us understand how the "pulling" behavior in our simulations plays out. In our simulations, the vertical wavenumber remains constant at $k_y = \sqrt{3}/2$, as verified in independent measurements which have not been included. This is due to the vertical dimension of our choice of domain.

One could study the selection of $k_y$ due to a horizontal planar jump-type inhomogeneity, at say $y = 0$. This is equivalent to studying the second "rows of hexagons" orientation.

### Rotations of Hexagons

To investigate the second orientation, many of the computations here could be recycled. Such a computation would still be significant, because the different scaling of space results in new coefficients in the normal form transformations, which must be computed in order to bridge the inhomogeneity. The end result would be the same amplitude equations with different coefficients.

In a different direction, Goh et al have investigated situations where a moving trigger selects stripes with orientations depending on speed [28, 7]. We could guess that the same phenomenon might be present with hexagons, by relating columns of hexagons to stripes, but it would be exceedingly difficult to observe. While the hexagonal lattice is of course rotationally invariant, it is also rigid. Stripes can bend around a defect and snake there way to a preferred orientation. Meanwhile, in small rectangular domains, the orientation of hexagons developing from initial conditions is essentially fixed by the aspect ratio of the domain. Care must be taken to choose the correct dimensions to observe hexagons at all, particularly for small $\varepsilon$. These restrictions are lessened in large domains where the bulk makes small adjustments throughout to accommodate a mismatched aspect ratio. Of course, simulating in larger domains is more computationally costly and it can be difficult to isolate one effect, as our simulations in a strip do.

### Stability

We observed the breakdown of hexagonal patterns on the left half of the domain in numerics. First, for large values of $\varepsilon > 1/2$ with $\nu = \varepsilon$ we saw diagonal stripes develop after a moving inhomogeneity has pulled hexagons to a minimally bearable wavenumber. These transitions occurred only after long times. Second, for small values of $\varepsilon = \nu < 0.03$, it appeared that the front itself was unstable. Hexagons with smaller amplitude first developed on the right of the inhomogeneity, then these invaded the larger hexagons on the left. Finally, the whole domain devolved into a variety of patterns in localized patches including down hexagons, triangles, and very weak stripes.

The stability of hexagons with respect to perturbations in phase have been studied via amplitude equations in [44, 36, 19]. Interestingly, there is a bounded region of stability in the $k, \varepsilon$-plane, in contrast to the unbounded stability region of stripes in the same setting or in the one-dimensional setting with $\nu = 0$. There are two instabilities, a "rectangular Eckhaus" and a "rhombic", which each cause hexagons with wavenumbers outside the stability region to deform and break down. It would be interesting to see how the minimum wavenumbers selected by moving the inhomogeneity compare to these stability boundaries. Unfortunately, it does not appear that these stability boundaries have been computed for the Swift-Hohenberg equation. Our work here, specifically our computations of the normal form transformations, provide an excellent framework for interpreting the stability in the amplitude equations in terms of Swift-Hohenberg, but that project in outside the scope of this thesis.

# References


[1] G. Ahlers. *Experiments with Rayleigh-Bénard convection.* Springer, 2006.

[2] Guenter Ahlers. Experiments with pattern-forming systems. *Physica D: Nonlinear Phenomena*, 51(1-3):421–443, Aug 1991.

[3] I. Andrade-Silva, M. G. Clerc, and V. Odent. Zig-zag wall lattice in a nematic liquid crystal with an in-plane switching configuration. *Physical Review E*, 90(2), Aug 2014.

[4] Tarik Aougab, Margaret Beck, Paul Carter, Surabhi Desai, Björn Sandstede, Melissa Stadt, and Aric Wheeler. Isolas versus snaking of localized rolls. *Journal of Dynamics and Differential Equations*, Oct 2017.

[5] V I Arnold. On matrices depending on parameters. *Russian Mathematical Surveys*, 26(2):29–43, Apr 1971.

[6] Yu. Astrov, E. Ammelt, S. Teperick, and H.-G. Purwins. Hexagon and stripe turing structures in a gas discharge system. *Physics Letters A*, 211(3):184–190, Feb 1996.

[7] Montie Avery, Ryan Goh, O. Goodloe, A. Milewski, and Arnd Scheel. Growing stripes, with and without wrinkles. *SIAM J Appl Dyn Sys*, to appear.

[8] Debbie L. Benson, Jonathan A. Sherratt, and Philip K. Maini. Diffusion driven instability in an inhomogeneous domain. *Bulletin of Mathematical Biology*, 55(2):365–384, Mar 1993.

[9] E. Buzano and M. Golubitsky. Bifurcation on the hexagonal lattice and the planar benard problem. *Philosophical Transactions of the Royal Society A: Mathematical, Physical and Engineering Sciences*, 308(1505):617–667, Mar 1983.

[10] V. Castets, E. Dulos, J. Boissonade, and P. DeKepper. Experimental evidence of a sustained standing Turing-type nonequilibrium chemical pattern. *Phys. Rev. Lett.*, 64(24):2953–2956, Jun. 1990.

[11] Carmen Chicone. *Ordinary Differential Equations with Applications*. 34. Springer-Verlag New York, 2 edition, 2006.

[12] Shui-Nee Chow and Jack K. Hale. Methods of bifurcation theory. *Grundlehren der mathematischen Wissenschaften*, 1982.

[13] P. Collet and J-P. Eckmann. *Instabilities and fronts in extended systems*. Princeton University Press, 1990.

[14] M. Cross, P. Daniels, P. Hohenberg, and E. Siggia. Phase-winding solutions in a finite container above the convective threshold. *Journal of Fluid Mechanics*, 127:155–183, 1983.

[15] M. C. Cross and P. C. Hohenberg. Pattern formation outside of equilibrium. *Rev. Mod. Phys.*, 65(3):851–1112, Jul. 1993.

[16] Peter Deuflhard and Folkmar Bornemann. Scientific computing with ordinary differential equations. *Texts in Applied Mathematics*, 2002.

[17] A. Doelman, B. Sandstede, A. Scheel, and G. Schneider. Propagation of hexagonal patterns near onset. *European Journal of Applied Mathematics*, 14:85–110, 2003.

[18] A. Doelman, P. van Heijster, and F. Xie. A geometric approach to stationary defect solutions in one space dimension. *SIAM J. Applied Dynamical Systems*, 15(2):655–712, 2016.

[19] B Echebarria and C Pérez-García. Phase instabilities in hexagonal patterns. *Europhysics Letters (EPL)*, 43(1):35–40, Jul 1998.

[20] M. Potier Ferry. *Collapse: The Buckling of Structures in Theory and Practice*. Cambridge University Press, 1983.

[21] E. Fontich and C. Simó. Invariant manifolds for near identity differentiable maps and splitting of separatrices. *Ergodic Theory and Dynamical Systems*, 10(02), Jun 1990.

[22] E. Fontich and C. Simó. The splitting of separatrices for analytic diffeomorphisms. *Ergodic Theory and Dynamical Systems*, 10(02), Jun 1990.

[23] A. Geraci and S. Longhi. Swift-Hohenberg equation for optical parametric oscillators. *Physical Review A*, 54(5):4581–4, 1996.

[24] Stephan Getzin, Hezi Yizhaq, Bronwyn Bell, Todd E. Erickson, Anthony C. Postle, Itzhak Katra, Omer Tzuk, Yuval R. Zelnik, Kerstin Wiegand, Thorsten Wiegand, and et al. Discovery of fairy circles in australia supports self-organization theory. *Proceedings of the National Academy of Sciences*, 113(13):3551–3556, Mar 2016.

[25] R. Goh, R. Beekie, D. Matthias, J. Nunley, and A. Scheel. Universal wave-number selection laws in apical growth. *Physical Review E*, 94(2), 2016.

[26] R. Goh and A. Scheel. Triggered fronts in the complex Ginzburg-Landau equation. *Journal of Nonlinear Science*, 24:117–144, 2014.

[27] R. Goh and A. Scheel. Pattern formation in the wake of triggered pushed fronts. *Nonlinearity*, 29(8):2196 –2237, 2016.

[28] Ryan Goh and Arnd Scheel. Pattern-forming fronts in a swift-hohenberg equation with directional quenching - parallel and oblique stripes. *Journal of the London Mathematical Society*, 98(1):104–128, Mar 2018.

[29] Google Earth. `https://earth.app.goo.gl/EwTeHB`, April 2019.

[30] M. Haragus and G. Iooss. *Local Bifurcations, Center Manifolds, and Normal Forms in Infinite-Dimensional Dynamical Systems*. Springer, 2011.

[31] M. Haragus and A. Scheel. A bifurcation approach to non-planar traveling waves in reaction-diffusion systems. *GAMM-Mitt.*, 30:75–95, 2007.

[32] Mariana Haragus and Arnd Scheel. Interfaces between rolls in the Swift-Hohenberg equation. *Int. J. Dyn. Syst. Differ. Equ.*, 1(2):89–97, 2007.

[33] Mariana Haragus and Arnd Scheel. Grain boundaries in the Swift-Hohenberg equation. *European J. Appl. Math.*, 23(6):737–759, 2012.

[34] T. Hiscock and S. Megason. Orientation of Turing-like patterns by morphogen gradients and tissue anisotrophies. *Cell Systems*, 1:408–416, 2015.

[35] R. B. Hoyle. Steady squares and hexagons on a subcritical ramp. *Physical Review E*, 51(1):310–315, Jan 1995.

[36] R.B. Hoyle. Nonlinear phase diffusion equations for the long-wave instabilities of hexagons. *Applied Mathematics Letters*, 8(3):81–85, May 1995.

[37] Rebecca Hoyle. Pattern formation. 2006.

[38] G. Iooss and A. Mielke. Time-periodic ginzburg-landau equations for one dimensional patterns with large wave length. *ZAMP Zeitschrift fr angewandte Mathematik und Physik*, 43(1):125–138, Jan 1992.

[39] G. Iooss and M.C. Peroueme. Perturbed homoclinic solutions in reversible 1:1 resonance vector fields. *Journal of Differential Equations*, 102(1):62–88, Mar 1993.

[40] Gabriela Jaramillo and Arnd Scheel. Deformation of striped patterns by inhomogeneities. *Mathematical Methods in the Applied Sciences*, 38(1):51–65, Dec 2013.

[41] C. Knight and G. Derks. A stability criterion for the non-linear wave equation with spatial inhomogeniety. *J. Differential Equations*, 259(9):4745–4762, 2015.

[42] A. Kock and H. Meinhardt. Biological pattern formation: from basic mechanisms to complex structures. *Reviews of Modern Physics*, 66(4):1481–1507, 1994.

[43] Lorenz Kramer, Eshel Ben-Jacob, Helmut Brand, and M. C. Cross. Wavelength selection in systems far from equilibrium. *Physical Review Letters*, 49(26):1891–1894, Dec 1982.

[44] J Lauzeral, S Metens, and D Walgraef. On the phase dynamics of hexagonal patterns. *Europhysics Letters (EPL)*, 24(9):707–712, Dec 1993.

[45] J. Lega, J. Moloney, and A. Newell. Swift-Hohenberg equation for lasers. *Phys. Rev. Lett.*, 73(22):2978–2981, 1994.

[46] J. Lega, J. Moloney, and A. Newell. Universal description of laser dynamics near threshold. *Physica D*, 83:478–498, 1995.

[47] D. Lloyd and A. Scheel. Continuation and bifurcation of grain boundaries in the Swift-Hohenberg equation. *SIAM J Appl Dyn Sys*, 16(1):252–293, 2017.

[48] David J. B. Lloyd, Björn Sandstede, Daniele Avitabile, and Alan R. Champneys. Localized hexagon patterns of the planar swift–hohenberg equation. *SIAM Journal on Applied Dynamical Systems*, 7(3):1049–1100, Jan 2008.

[49] Elizabeth Makrides and Björn Sandstede. Existence and stability of spatially localized patterns. *Journal of Differential Equations*, 266(2-3):1073–1120, Jan 2019.

[50] R. Marangell, C. K. R. T. Jones, and H. Susanto. Localized standing waves in inhomogeneous Schrödinger equations. *Nonlinearity*, 23(9):2059–2080, 2010.

[51] I. Melbourne. Derivation of the time-dependent ginzburg-landau equation on the line. *Journal of Nonlinear Science*, 8(1):1–15, Feb 1998.

[52] Alexander Mielke. Instability and stability of rolls in the Swift-Hohenberg equation. *Comm. Math. Phys.*, 189:829–853, 1997.

[53] David G. Míguez, Milos Dolnik, Irving Epstein, and Alberto P. Muñuzuri. Interaction of chemical patterns in coupled layers. *Phys. Rev. E*, 84:046210, Oct 2011.

[54] David G. Míguez, Milos Dolnik, Alberto P. Muñuzuri, and Lorenz Kramer. Effect of axial growth on turing pattern formation. *Physical Review Letters*, 96(4), Feb 2006.

[55] Rafael Monteiro. Horizontal patterns from finite speed directional quenching. *arXiv:1707.09010*, 2017.

[56] Rafael Monteiro and Arnd Scheel. Contact angle selection for interfaces in growing domains. *arXiv:1705.00079*, 2017.

[57] Rafael Monteiro and Arnd Scheel. Phase separation patterns from directional quenching. *Journal of Nonlinear Science*, 2017.

[58] D. Morrissey and A. Scheel. Characterizing the effect of boundary conditions on striped phases. *SIAM J. Applied Dynamical Systems*, 14(3), 2015.

[59] NASA. https://visibleearth.nasa.gov/view.php?id=59758, June 2002.

[60] NASA. https://www.visibleearth.nasa.gov/view.php?id=6243, January 2006.

[61] A. C. Newell and J. A. Whitehead. Finite bandwidth, finite amplitude convection. *J. Fluid Mech.*, 38(2):279–303, Sep. 1969.

[62] Kenneth J Palmer. Exponential dichotomies and transversal homoclinic points. *Journal of Differential Equations*, 55(2):225–256, Nov 1984.

[63] Kenneth J. Palmer. Exponential dichotomies and fredholm operators. *Proceedings of the American Mathematical Society*, 104(1):149–149, Jan 1988.

[64] L. Peletier and W. Troy. Pattern formation described by the Swift-Hohenberg equation. *Sūrikaisekikenkyūsho Kōkyūroku*, (1178):1–15, 2000.

[65] L. Perko. *Differential Equations and Dynamical Systems.* Number 7 in Texts in Applied Mathematics. Springer, 1996.

[66] Y. Pomeau and S. Zaleski. Wavelength selection in one-dimensional cellular structures. *Journal de Physique*, 42(4):515–528, 1981.

[67] Y. Pomeau and S. Zaleski. Pattern selection in a slowly varying environment. *Journal de Physique Lettres*, 44(4):135–141, 1983.

[68] H.G. Purwins. https://www.uni-muenster.de/Physik.AP/Purwins/DC/index-en.html, 2011.

[69] Björn Sandstede and Arnd Scheel. On the structure of spectra of modulated travelling waves. *Mathematische Nachrichten*, 232(1):39–93, Dec 2001.

[70] A. Scheel and J. Weinburd. Wavenumber selection via spatial parameter jump. *Phil Trans Roy Soc A*, https://doi.org/10.1098/rsta.2017.0191(2117), 2018.

[71] Arnd Scheel and Qiliang Wu. Small-amplitude grain boundaries of arbitrary angle in the Swift-Hohenberg equation. *ZAMM Z. Angew. Math. Mech.*, 94(3):203–232, 2014.

[72] Guido Schneider. Error estimates for the ginzburg-landau approximation. *ZAMP Zeitschrift fr angewandte Mathematik und Physik*, 45(3):433–457, May 1994.

[73] J. Swift and P. Hohenberg. Hydrodynamic fluctuations at the convective instability. *Physical Review A*, 15(1):319–328, 1977.

[74] A. van Harten. On the validity of the ginzburg-landau equation. *Journal of Nonlinear Science*, 1(4):397–422, Dec 1991.

[75] R.Dennis Vigil, Q. Ouyang, and Harry L. Swinney. Turing patterns in a simple gel reactor. *Physica A: Statistical Mechanics and its Applications*, 188(1-3):17–25, Sep 1992.

# Appendix A

# Normal Form Computations

This appendix includes computations used to obtain the normal form transformations in Chapter 2. To this end, we restate and prove Lemma 2.6 using a form more closely following [30].

**Lemma A.1.** *For any positive integer $N \geq 2$, there exist neighborhoods $\mathcal{V}, \mathcal{M}$ of $0$ in $\tilde{\mathbb{C}}^2$ and $\mathbb{R}$ respectively so that for any $\mu \in \mathcal{M}$ there exists a polynomial $\Phi(\cdot\,;\mu)\colon \tilde{\mathbb{C}}^2 \to \mathbb{R}^4$ of degree $N$ with the following properties:*

*(i) The coefficients of the monomials of degree $q$ in $\Phi(\cdot\,;\mu)$ are functions of $\mu$ of class $\mathcal{C}^{N-q}$,*

$$\Phi(0,0;0) = 0, \qquad \partial_{(A,B,\overline{A},\overline{B})}\Phi(0,0;0) = 0, \quad \textit{and} \quad \mathbf{S}\Phi(A,B;\mu) = \Phi(\overline{A},-\overline{B};\mu).$$

*(ii) For $(A,B) \in \mathcal{V}$, the change of variables*

$$U = A\begin{bmatrix}1\\ i\\ 0\\ 0\end{bmatrix} + B\begin{bmatrix}0\\ 1\\ 2i\\ -2\end{bmatrix} + \overline{A}\begin{bmatrix}1\\ -i\\ 0\\ 0\end{bmatrix} + \overline{B}\begin{bmatrix}0\\ 1\\ -2i\\ -2\end{bmatrix} + \Phi(A,B;\mu) \tag{A.1}$$

*gives a transformation* $\mathbb{R}^4 \leftrightarrow \tilde{\mathbb{C}}^2$ *which transforms equation* (2.11) *into*

$$\begin{bmatrix} A_x \\ B_x \end{bmatrix} = \begin{bmatrix} i & 1 \\ 0 & i \end{bmatrix} \begin{bmatrix} A \\ B \end{bmatrix} + \begin{bmatrix} iP(A,B;\mu) & 0 \\ Q(A,B;\mu) & iP(A,B;\mu) \end{bmatrix} \begin{bmatrix} A \\ B \end{bmatrix} + G(A,B;\mu) \qquad \text{(A.2)}$$

*where the remainder* $G(A,B;\mu) = o((|A|+|B|)^N)$ *and* $P, Q$ *are real valued polynomials of degree* $N-1$ *given by*

$$P(|A|^2, (A\overline{B} - \overline{A}B); \mu) = -\tfrac{1}{8}\mu + \tfrac{9}{16}|A|^2 + \mathcal{O}\left((|\mu| + (|A|+|B|)^2)^2\right)$$
$$Q(|A|^2, (A\overline{B} - \overline{A}B); \mu) = -\tfrac{1}{4}\mu + \tfrac{3}{4}|A|^2 + \tfrac{3i}{16}(A\overline{B} - \overline{A}B) + \mathcal{O}\left((|\mu| + (|A|+|B|)^2)^2\right).$$

*Proof.* The lemma is a restatement of Lemma 3.17 in [30] in the particular case of a double eigenvalue equal to $i$. We show that our scenario satisfies the hypotheses of Lemma 3.17, then use a later computation from [30] to find the coefficients in the normal form.

By our discussion in the main text, $\mathbf{S}$ is a reversibility symmetry for the vector field in (2.11) and so our equation satisfies Hypothesis 3.1 in [30]. The spectrum of $L$ is $\{\pm i\}$, so we have also satisfied Hypothesis 3.14 with $\kappa = 1$.

Finally, we quickly discuss the basis for $\mathbb{C}^2$. Let

$$v_0 = \begin{bmatrix} 1 \\ i \\ 0 \\ 0 \end{bmatrix} \qquad \text{and} \qquad v_1 = \begin{bmatrix} 0 \\ 1 \\ 2i \\ -2 \end{bmatrix}$$

be the eigenvector and generalized eigenvector pair for $L$ corresponding to eigenvalue $i$. Indeed, the reader may check that $Lv_0 = iv_0$ and $(L-i)^2 v_1 = 0$, while $(L-i)v_1 = v_0$. The conjugated pair $\overline{v}_0, \overline{v}_1$ corresponds to the eigenvalue $-i$. In addition, note that $\mathbf{S}v_0 = \overline{v}_0$ and $\mathbf{S}v_1 = -\overline{v}_1$. This shows that the pair $v_0, v_1 \in \mathbb{C}^4$ satisfies the conditions in Lemma 3.15, and so $\{v_0, v_1, \overline{v}_0, \overline{v}_1\}$ is the basis of $\tilde{\mathbb{R}}^4$ mentioned in Lemma 3.17.

We have now satisfied the hypotheses of Lemma 3.17, so we know that some appropriate $\Phi$ transforms (2.11) into the normal form (2.14). In the example on page 223, the authors compute the first three coefficients in each of the polynomials $P, Q$ to be

$\alpha = -\frac{1}{8},\ \beta = \frac{9}{16},\ \gamma = 0$, and $a = -\frac{1}{4},\ b = \frac{3}{4},\ c = \frac{3i}{16}$, respectively. The method for computing these coefficients involves an algorithm which comes from the proof of the theorem. It is outlined in the next proof below. □

## A.1 Constructive Proof of Lemma 2.7

This section includes the computations necessary for a constructive proof of Lemma 2.7. That is, we explain how we computed the $\mu$-dependent linear normal form transformation $\Phi_{1,1}(A, B; \mu)$ for the 1-dimensional Swift-Hohenberg equation.

**Lemma A.2.** *Let $\mathcal{M}$ be the neighborhood guaranteed by Lemma A.1. For any $\mu \in \mathcal{M}$, a polynomial satisfying the conditions of Lemma A.1 with $N = 4$ is*

$$\Phi(A, B; \mu) = \sum_{|q|=2,3} \Phi_{(q)} A^{q_1} B^{q_2} \overline{A}^{q_3} \overline{B}^{q_4} \mu^{q_5} \tag{A.3}$$

*where $(q) = q_1 q_2 q_3 q_4 q_5$ is a multi index with size $|q| = q_1 + q_2 + q_3 + q_4 + q_5$. The vector coefficients $\Phi_{(q)}$ with $|q| = 2$ that are nonzero are*

$$\Phi_{10001} = \begin{bmatrix} 0 \\ \frac{-i}{8} \\ 0 \\ \frac{-i}{2} \end{bmatrix}, \quad \Phi_{01001} = \begin{bmatrix} 0 \\ 0 \\ \frac{-i}{4} \\ \frac{1}{2} \end{bmatrix}, \quad \Phi_{00101} = \overline{\Phi_{10001}}, \quad \textit{and} \quad \Phi_{00011} = \overline{\Phi_{01001}}$$

*and the nonzero vector coefficients with $|q| = 3$ are given in Table A.1, where*

$$v_0 = \begin{bmatrix} 1 \\ i \\ 0 \\ 0 \end{bmatrix}, \qquad v_1 = \begin{bmatrix} 0 \\ 1 \\ 2i \\ -2 \end{bmatrix}.$$

There are two methods of proof. First, we could simply show that this polynomial satisfies the two conditions. Second, we could show the explicit construction of this polynomial which follows the proof of the general normal form theorem, Lemma A.1. To demonstrate the algorithmic nature of the proofs in normal form theory, we outline

the second with the simplification of removing the dependence on parameter $\mu$.

*Proof.* Let $\mathcal{N}(A,B) = \begin{bmatrix} iP(A,B) & 0 \\ Q(A,B) & iP(A,B) \end{bmatrix} \begin{bmatrix} A \\ B \end{bmatrix} + \text{c.c.}$ be the nonlinear terms in normal form, see equation (2.14). Note that here the complex conjugate terms are all in the 3rd and 4th components. We differentiate equation (2.13), and then then plug in for $\frac{dU}{dx}$ using equation (2.11) and for $(A_x, B_x, \overline{A}_x, \overline{B}_x)^\top$ using equation (2.14). After significantly rearranging terms, we have

$$\begin{aligned} D\Phi \begin{bmatrix} i & 1 \\ 0 & i \end{bmatrix} \begin{bmatrix} A \\ B \end{bmatrix} - L\Phi(A,B) \\ = R\left(\Theta_1 \begin{bmatrix} A \\ B \end{bmatrix} + \Phi(A,B)\right) - (\Theta_1 + D\Phi)\mathcal{N}(A,B) + (\Theta_1 + D\Phi)G(A,B) \end{aligned} \tag{A.4}$$

where $\Theta_1 = \begin{bmatrix} 1 & 0 & 1 & 0 \\ i & 1 & -i & 1 \\ 0 & 2i & 0 & -2i \\ 0 & -2 & 0 & -2 \end{bmatrix}$ and we use $\begin{bmatrix} A \\ B \end{bmatrix}$ as shorthand for $\begin{bmatrix} A \\ B \\ \overline{A} \\ \overline{B} \end{bmatrix}$ to save writing all the complex conjugate terms. The-left hand side of equation (A.4) is called the "homological operator" and it acts on the space of polynomials $f\colon \tilde{\mathbb{C}}^2 \to \mathbb{R}^4$ by

$$\mathscr{A}_L(f)(A,B) = Df \begin{bmatrix} i & 1 \\ 0 & i \end{bmatrix} \begin{bmatrix} A \\ B \end{bmatrix} - Lf(A,B).$$

A key property of $\mathscr{A}_L$ is that the space of homogeneous polynomials of degree $q$ is invariant under $\mathscr{A}_L$. Now we may define an inner product on the homogeneous polynomials of degree $q$ so that $(\mathscr{A}_L)^* = \mathscr{A}_{L^*}$. The details of this inner product may be found in [30].

Next, we expand using Taylor series and compare terms. At order $q$, we have a solvable equation exactly when the right-hand side of equation (A.4) is in image $\mathscr{A}_L = (\ker \mathscr{A}_{L^*})^\perp$. These solvability conditions allow us to solve for coefficients in the transformation $\Phi$ and in the normal form $\mathcal{N}$. The rest is simply executing the linear algebra, with computations below

When the dependence on the parameter is reintroduced, the main idea remains the same. We must only be more careful in what we mean by "order" so that it may account for powers of the parameter as well.

Executing the procedure above in our case leads to solvability conditions that are expressed by equations given in [30, Appendix D.2]. At order $\mu A, \mu B$ we have

$$\begin{aligned} av_1 + \mathrm{i}\alpha v_0 &= (L - i)\Phi_{10001} + R(v_0, \mu) \\ \mathrm{i}\alpha + \Phi_{10001} &= (L - i)\Phi_{01001} + R(v_1, \mu) \end{aligned}$$

Solving the first yields $\Phi_{10001} = (0, \frac{-\mathrm{i}}{8}, 0, \frac{-\mathrm{i}}{2})^\top + M$ for $M \in \ker(L - \mathrm{i})$. After choosing $M = 0$, the second yields $\Phi_{01001} = (0, 0, \frac{\mathrm{i}}{4}, \frac{1}{2})^\top$. Other equations at order $|q| = 2$ give vector coefficients $\Phi_{(q)} = 0$. At order $|q| = 3$, we obtain a total of ten equations, up to conjugate symmetries. In [30, Appendix D.2], these are labeled (D.35-D.44). The first four may be solved straightforwardly by inverting $(L - 3\mathrm{i})$, giving the vector coefficients in the first column of Table A.1. The remaining six equation can be solved up to an element of $\ker(L - \mathrm{i}) = \operatorname{span}\{v_0\}$.

Solving these six equations in order, we arrive at

$$\Phi_{20100} = \begin{bmatrix} 0 \\ 9\mathrm{i}/16 \\ -3/8 \\ 9\mathrm{i}/8 \end{bmatrix} + av_0, \quad \Phi_{20010} = \begin{bmatrix} 0 \\ 0 \\ 3\mathrm{i}/4 \\ -3/2 \end{bmatrix} + av_1 + bv_0, \quad \Phi_{11100} = \begin{bmatrix} 0 \\ 0 \\ 3\mathrm{i}/2 \\ -3 \end{bmatrix} + 2av_1 + cv_0$$

for any $a, b, c \in \mathbb{C}$. Choosing $a = \frac{-9}{16}$ makes the next two equations solvable and we have

$$\Phi_{02100} = \begin{bmatrix} 0 \\ 0 \\ -9/8 \\ -15\mathrm{i}/8 \end{bmatrix} + dv_0, \qquad \Phi_{11010} = \begin{bmatrix} 0 \\ 0 \\ -9/4 \\ -15\mathrm{i}/4 \end{bmatrix} + 2bv_1 + cv_1 + ev_0$$

for any $d, e \in \mathbb{C}$. Choosing $b = 0, c = \frac{-9\mathrm{i}}{4}$ makes the last equation solvable and we have

$$\Phi_{02010} = \begin{bmatrix} 0 \\ 0 \\ -9\mathrm{i}/4 \\ 27/8 \end{bmatrix} + dv_1 + fv_0$$

for any $f \in \mathbb{C}$. We are now free to choose $d = e = f = 0$, and have the entries in the second and third columns of Table A.1. □

| Order | Vector Coefficient | Order | Vector Coefficient | Order | Vector Coefficient |
|---|---|---|---|---|---|
| $A^3$ | $\Phi_{30000} = \begin{bmatrix} -1/64 \\ -3i/64 \\ 1/8 \\ 3i/8 \end{bmatrix}$ | $A^2\overline{A}$ | $\Phi_{20100} = \begin{bmatrix} 0 \\ 9i/16 \\ -3/8 \\ 9i/8 \end{bmatrix} - \frac{9}{16}v_0$ | $B^2\overline{A}$ | $\Phi_{02100} = \begin{bmatrix} 0 \\ 0 \\ -9/8 \\ -15i/8 \end{bmatrix}$ |
| $A^2B$ | $\Phi_{21000} = \begin{bmatrix} -9i/128 \\ 21/128 \\ 9i/32 \\ -15/32 \end{bmatrix}$ | $A^2\overline{B}$ | $\Phi_{20010} = \begin{bmatrix} 0 \\ 0 \\ 3i/4 \\ -3/2 \end{bmatrix} - \frac{9}{16}v_1$ | $AB\overline{B}$ | $\Phi_{11010} = \begin{bmatrix} 0 \\ 0 \\ -9/4 \\ -15i/4 \end{bmatrix} - \frac{9i}{4}v_1$ |
| $AB^2$ | $\Phi_{12000} = \begin{bmatrix} 69/512 \\ 135i/512 \\ -21/64 \\ -27i/64 \end{bmatrix}$ | $AB\overline{A}$ | $\Phi_{11100} = \begin{bmatrix} 0 \\ 0 \\ 3i/2 \\ -3 \end{bmatrix} - 2\frac{9}{16}v_1 - \frac{9i}{4}v_0$ | $B^2\overline{B}$ | $\Phi_{02010} = \begin{bmatrix} 0 \\ 0 \\ -9i/4 \\ 27/8 \end{bmatrix}$ |
| $B^3$ | $\Phi_{03000} = \begin{bmatrix} 27i/256 \\ -93/512 \\ -45i/256 \\ 51/256 \end{bmatrix}$ | | and ten conjugates given by | | $\overline{\Phi_{q_1q_2q_3q_4q_5}} = \Phi_{q_3q_4q_1q_2q_5}$ |

Table A.1: The coefficients in the order three normal form transformation.

## Reordering the Normal Form Transformations

While the theory and the example of [30] let us explicitly determine the normal form transformation with a little linear algebra, for our purposes it is more useful to have the transformation in a different form. Our goal is to have a sequence of transformations whose composition yields the transformation found in the last section.

We begin by applying Lemma A.1 at orders $|q| = 1, 2, 3$ sequentially. When $N = 1$, the transformation given by (2.13) is linear and puts the matrix $L$ in equation (2.11) into Jordan normal form and leaves higher order terms unchanged, i.e. the polynomials

$P, Q$ in equation (2.14) are both the zero polynomial. This transformation is given by

$$\Phi_{\text{Lin}}(A,B) = A\begin{bmatrix}1\\ i\\ 0\\ 0\end{bmatrix} + B\begin{bmatrix}0\\ 1\\ 2i\\ -2\end{bmatrix} + \overline{A}\begin{bmatrix}1\\ -i\\ 0\\ 0\end{bmatrix} + \overline{B}\begin{bmatrix}0\\ 1\\ -2i\\ -2\end{bmatrix} = \begin{bmatrix}1 & 0 & 1 & 0\\ i & 1 & -i & 1\\ 0 & 2i & 0 & -2i\\ 0 & -2 & 0 & -2\end{bmatrix}\begin{bmatrix}A\\ B\\ \overline{A}\\ \overline{B}\end{bmatrix},$$

When $N = 2$, the transformation from Lemma A.1 has the same effect on the matrix $L$ but also affects the terms of orders $\mu A, \mu B$ and complex conjugates. The polynomials $P, Q$ have degree 1, and so are simply the constant $\mu$ terms. This transformation is given by

$$\begin{aligned}\Phi_{\text{Lin}}(A,B) + \Phi_\mu(A,B;\mu) = &\begin{bmatrix}| & | & | & |\\ v_0 & v_1 & \overline{v_0} & \overline{v_1}\\ | & | & | & |\end{bmatrix}\begin{bmatrix}A\\ B\\ \overline{A}\\ \overline{B}\end{bmatrix}\\ &+ \mu\begin{bmatrix}| & | & | & |\\ \Phi_{10001} & \Phi_{01001} & \overline{\Phi_{10001}} & \overline{\Phi_{01001}}\\ | & | & | & |\end{bmatrix}\begin{bmatrix}A\\ B\\ \overline{A}\\ \overline{B}\end{bmatrix}\\ = &\begin{bmatrix}1 & 0 & 1 & 0\\ i & 1 & -i & 1\\ 0 & 2i & 0 & -2i\\ 0 & -2 & 0 & -2\end{bmatrix}\begin{bmatrix}A\\ B\\ \overline{A}\\ \overline{B}\end{bmatrix} + \mu\begin{bmatrix}0 & 0 & 0 & 0\\ \frac{-i}{8} & 0 & \frac{i}{8} & 0\\ 0 & \frac{-i}{4} & 0 & \frac{i}{4}\\ \frac{-i}{2} & \frac{1}{2} & \frac{i}{2} & \frac{1}{2}\end{bmatrix}\begin{bmatrix}A\\ B\\ \overline{A}\\ \overline{B}\end{bmatrix}.\end{aligned}$$

The vector coefficients $\Phi_{(q)}$ were found in Lemma A.2.

Finally, when $N = 3$, the transformation includes the lower order parts from $N = 1, 2$ and now includes a part $\Phi_{\text{Cub}}$ acting on the terms of order 3. A complete description of $\Phi_{\text{Cub}}$ is given by Table A.1. We denote the full, order 3 normal form by

$$\Psi(A,B;\mu) = \Phi_{\text{Lin}}(A,B) + \Phi_\mu(A,B;\mu) + \Phi_{\text{Cub}}(A,B).$$

We seek to write this $\Psi$ as a composition of three transformations

$$\begin{aligned} &\Theta_1 \colon \tilde{\mathbb{C}}^2 \to \mathbb{R}^4 \\ &\Theta_2 \colon \tilde{\mathbb{C}}^2 \to \tilde{\mathbb{C}}^2 \qquad \text{so that} \quad \Psi(A, B; \mu) = \Theta_1 \circ \Theta_2 \circ \Theta_3(A, B), \\ &\Theta_3 \colon \tilde{\mathbb{C}}^2 \to \tilde{\mathbb{C}}^2 \end{aligned}$$

as in Figure A.1a. Note that $\Theta_2 = \Theta_2(\mu)$ depends on $\mu$, but we omit this in notation for now.

The existence and well-definedness of the $\Theta_i$s is proved by simply finding their explicit expressions. First, we find matrices for $\Theta_1, \Theta_2$, which are linear, and then define $\Theta_3(A, B) = \Theta_2^{-1}\Theta_1^{-1}(\Psi(A, B; \mu))$.

From above, we know that

$$\Phi_{\text{Lin}}(A, B) = \begin{bmatrix} 1 & 0 & 1 & 0 \\ i & 1 & -i & 1 \\ 0 & 2i & 0 & -2i \\ 0 & -2 & 0 & -2 \end{bmatrix} \begin{bmatrix} A \\ B \\ \overline{A} \\ \overline{B} \end{bmatrix} = \Theta_1 \begin{bmatrix} A \\ B \\ \overline{A} \\ \overline{B} \end{bmatrix},$$

So we have an expression for $\Theta_1$.

Next,

$$\Theta_2 \begin{bmatrix} A \\ B \\ \overline{A} \\ \overline{B} \end{bmatrix} = \Theta_1^{-1} \left( \Phi_{\text{Lin}}(A,B) + \Phi_\mu(A,B;\mu) \right)$$

$$= \Theta_1^{-1} \left( \Theta + \mu \begin{bmatrix} 0 & 0 & 0 & 0 \\ \frac{-i}{8} & 0 & \frac{i}{8} & 0 \\ 0 & \frac{-i}{4} & 0 & \frac{i}{4} \\ \frac{-i}{2} & \frac{1}{2} & \frac{i}{2} & \frac{1}{2} \end{bmatrix} \right) \begin{bmatrix} A \\ B \\ \overline{A} \\ \overline{B} \end{bmatrix}$$

$$= \left( \begin{bmatrix} 1 & 0 & 0 & 0 \\ 0 & 1 & 0 & 0 \\ 0 & 0 & 1 & 0 \\ 0 & 0 & 0 & 1 \end{bmatrix} + \mu \begin{bmatrix} \frac{-3}{16} & \frac{-i}{8} & \frac{3}{16} & \frac{-i}{8} \\ \frac{i}{8} & \frac{-3}{16} & \frac{-i}{8} & \frac{-1}{16} \\ \frac{3}{16} & \frac{i}{8} & \frac{-3}{16} & \frac{-i}{8} \\ \frac{i}{8} & \frac{-1}{16} & \frac{-i}{8} & \frac{-3}{16} \end{bmatrix} \right) \begin{bmatrix} A \\ B \\ \overline{A} \\ \overline{B} \end{bmatrix}.$$

Thus we also have a matrix for $\Theta_2 = \text{Id.} + \mu M$ where $M$ is the second matrix above.

We can compute $\det \Theta_2 = 1 - \frac{3}{4}\mu + \frac{7}{64}\mu^2 - \frac{1}{256}\mu^3$, so $\Theta_2$ is invertible for all $\mu > 0$. We expand the inverse as a Neumann series and see that

$$\begin{aligned} \Theta_2^{-1} &= (\text{Id.} + \mu M)^{-1} \\ &= \sum_{n=0}^{\infty} (-\mu M)^n \\ &= \text{Id.} - \mu M + \mathcal{O}(\mu^2). \end{aligned}$$

Now $\mu M = \Phi_{1,1}(\varepsilon^2)$.

Furthermore, the two transformations $\Theta_3, \Theta_2$ commute, since the cubic transformation only affects cubic terms in the vector field. The result is that the two diagrams in Figure A.1 are equivalent.

**Lemma A.3.** *The normal form transformation described in Lemma A.1 with $N = 3$ is alternatively given by*

$$\Psi(A,B) = \Theta_1 \circ \Theta_3 \circ \Theta_2(A,B)$$

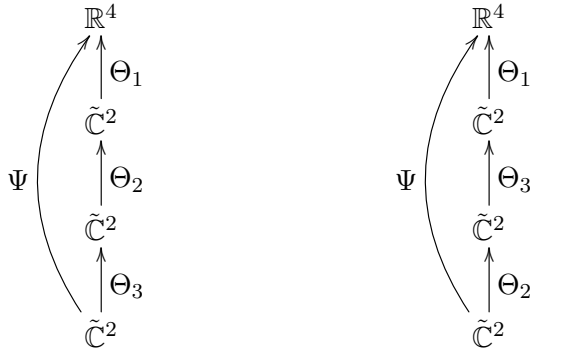


(a) The natural order.

(b) A reordering with $\Theta_2$ first.

Figure A.1: The normal form transformation $\Psi$ as a composition.

*where* $\Theta, \Theta_2$ *are defined by the matrices in the computations above and*

$$\Theta_3(A, B) = \Theta_2^{-1}\Theta_1^{-1}\left(\Psi(A, B; \mu)\right).$$

**Corollary A.4.** *Let* $\Psi$ *be the normal form transformation described in Lemma A.1 for arbitrary* $N$*. We can alternatively describe the transformation by*

$$\Psi(A, B) = \Theta_1 \circ \Theta_2 \circ \Theta_3 \circ \cdots \circ \Theta_N(A, B)$$

*where we define* $\Theta_1$ *as above and* $\Theta_N = \Theta_{N-1}^{-1} \circ \cdots \circ \Theta_1^{-1}\left(\Psi(A, B)\right)$*. Furthermore,* $\Theta_i \circ \Theta_j = \Theta_j \circ \Theta_i$ *for all* $i, j \neq 1$*.*

*Proof.* We have provided only the spirit of proof for this extension. □

Note that in fact, $\Theta_2 = \Theta_2(\mu)$ for $\mu$ close to 0. We compute one more composition which will be helpful in Section 2.5.1.

$$\begin{aligned}\Theta_2(\mu)^{-1}\Theta_2(-\mu) &= \left(\text{Id.} - \mu M + \mathcal{O}(\mu^2)\right)\left(\text{Id.} + (-\mu)M\right) \\ &= (\text{Id.} - \mu M)^2 + \mathcal{O}(\mu^2) \\ &= \text{Id.} - 2\mu M + \mathcal{O}(\mu^2)\end{aligned}$$

The key is that, at leading order in $\mu$, the transformation $\Theta_2(\mu)^{-1}\Theta_2(-\mu)$ is the identity.